



Synthesis and characterization of novel organic semiconducting materials for organic field effect transistors (OFETs) and photovoltaics (OPVs)

Submitted by

Sasikumar Arumugam

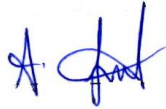
A thesis submitted in fulfilment of the requirements for the degree of Doctor of Philosophy in Department of Pure and Applied Chemistry, University of Strathclyde

2015

This thesis is the result of the author's original research. It has been composed by the author and has not been previously submitted for examination which has led to the award of a degree.

The copyright of this thesis belongs to the author under the terms of the United Kingdom Copyright Acts as qualified by University of Strathclyde Regulation 3.50. Due acknowledgement must always be made of the use of any material contained in, or derived from, this thesis.

Signed:

A handwritten signature in blue ink, consisting of a stylized 'A' followed by a cursive name.

Date: 25-03-2015

Acknowledgements

I thank Prof. Peter Skabara for the chance to work in his research group, the freedom and flexibility I've been given in my work, and the support and opportunities which have been available throughout the duration of my studies in his group.

I also owe a great deal of thanks to the postdoctoral researchers in the group, Dr. Anto Regis Inigo, Dr. Alexander Kanibolotsky, and Dr. Neil Findlay for their help and advice they have always been happy to provide. Especially, it was Dr. Alexander Kanibolotsky who spent a tremendous amount of time for proofreading of my thesis and made it read like English.

I would like to extend further thanks to Prof. Thomas Anthopoulos, Imperial College, London, for performing Top gate/Bottom contact (TG/BC) OFET studies of DPP-TTF polymer, included in chapter 3.

I would like to thank Dr. Saadeldin Elmasly for doing absorption, emission and cyclic voltammetry (CV) measurements. I thank Dr. Fiona Coomer for her help in doing XRD analysis for 5T-Ge material included in chapter 4. I would also like to thank researchers from UK national crystallographic service for analysing single XRD of perfluorobenzene sample included in chapter 6. I'm extremely grateful to my colleagues, Dr. Diego Cortizo Lacelle and Dr. Clara Orofino for providing the materials p(DPP-TTF) and DPP-Linear C respectively for OFET and OPV characterisation. I also extend my thanks to Dr. Iain Wright for providing 5T-TTF and 5T-Ge oligomers for OFET and OPV characterisation.

The group has always been a fun place to work and so I would like to personally acknowledge the other members of the group I have worked alongside for helping to

make my PhD studies an enjoyable as well as productive experience: Diego Cortizo Lacalle, Sandeep Kaur, Clara Orofino, Zuzana Vobecka, Zahera Mohsan, Neil Thompson, Joseph Cameron, Roisin Brown, Gary Conboy, Andrew McCrone and Enrico Angioni.

I wish to express my gratitude to my parents, for their prayers for me to complete my study successfully, encouraging me to follow my own path and for being always there to help and support me in every aspect of my life. I would like to express my warm feeling and offer special thanks to my wife, Amsadevi, who sacrificed so much for me and my thanks also to my father-in-law and mother-in-law. Thanks to my brother, sister and my friends for their prayers for me.

Abbreviations

| | |
|-----------------|--------------------------------------|
| CV | cyclic voltammetry |
| vis | visible |
| λ | wavelength |
| ν | frequency |
| Fc | ferrocene |
| Fc ⁺ | ferrocenium |
| Ge | germanium |
| HOMO | highest occupied molecular orbitals |
| LUMO | lowest unoccupied molecular orbitals |
| cm | centimetre |
| mV | millivolt |
| nm | nanometre |
| OFET | organic field effect transistor |
| V _{ds} | drain-source voltage |
| I _{ds} | drain-source current |
| V _{gs} | gate-source voltage |
| V | volt |
| V _{th} | threshold voltage |
| μ | charge carrier mobility |
| F | Faraday's constant |

| | |
|------------|------------------------------------|
| S/D | source and drain electrodes |
| SAM | self assembled monolayer |
| ITO | indium tin oxide |
| BHJ | bulk-heterojunction |
| V_{\max} | voltage at maximum power point |
| I_{\max} | current at maximum power point |
| FF | fill factor |
| V_{oc} | open circuit voltage |
| mA | milliampere |
| eV | electron volts |
| PCE | power conversion efficiency |
| I_{sc} | short circuit current |
| J_{sc} | short circuit current density |
| CF | chloroform |
| CB | chlorobenzene |
| o-DCB | ortho-dichlorobenzene |
| THF | tetrahydrofuran |
| SMOC | single material organic solar cell |
| BG/BC | bottom gate/bottom contact |
| TG/BC | top gate/bottom contact |
| RT | room temperature |

| | |
|---------------------|---|
| Ca | calcium |
| Al | aluminium |
| D/A | donor/acceptor |
| CCDC | Cambridge Crystallographic Data Centre |
| PC ₆₁ BM | phenyl-C ₆₀ -butyric acid methyl ester |
| PC ₇₁ BM | phenyl-C ₇₀ -butyric acid methyl ester |
| PFBT | pentafluorobenzenethiol |
| ODTS | octadecyltrichlorosilane |
| HMDS | hexamethyldisilazane |

Contents

| | |
|---|-----|
| Acknowledgements | 3 |
| Abbreviations | 5 |
| Table of figures | 11 |
| Table of Chart..... | 16 |
| Table of tables | 17 |
| Chapter 1 | 18 |
| 1.1 Organic semiconductors | 19 |
| 1.2 Band theory | 20 |
| 1.3 Doping of materials | 21 |
| 1.4 Oxidation and reduction | 22 |
| 1.5 Absorption and emission | 26 |
| 1.6 π -Bonding as an essential feature of organic semiconductor | 29 |
| 1.7 Operating principles and assembly of organic field effect transistors | 34 |
| 1.8 Organic Photovoltaics (OPV)..... | 43 |
| 1.9 Aim of the projects | 50 |
| Chapter 2 | 55 |
| 2.1 Abstract | 56 |
| 2.2 Introduction | 58 |
| 2.3 OFET fabrication of Oligothiophenes | 62 |
| 2.4 5T-TTF OFET results..... | 68 |
| 2.5 OPV fabrication using oligothiophenes materials..... | 76 |
| 2.6 5T-TTF OPV results..... | 79 |
| 2.7 Conclusions | 82 |
| Chapter 3 | 84 |
| 3.1 Abstract | 85 |
| 3.2 Introduction | 86 |
| 3.2 OFET studies for DPP-based polymers..... | 88 |
| 3.3 OPV studies for DPP-based polymers..... | 92 |
| 3.4 OFET results for DPP-TTF polymer..... | 98 |
| 3.5 OPV results for blend layer and single layer..... | 104 |

| | |
|---|-----|
| 3.6 Conclusions | 108 |
| Chapter 4 | 109 |
| 4.1 Abstract | 110 |
| 4.2 Concept of spiro linkage..... | 111 |
| 4.3 OFET results for devices fabricated by spincoating from chloroform solutions | 117 |
| 4.4 OFET results for devices fabricated by spincoating from chlorobenzene solutions..... | 118 |
| 4.5 Dependence of OFET performance on annealing temperature (chlorobenzene) | 120 |
| 4.6 Conclusions | 125 |
| Chapter 5 | 126 |
| 5.1 Abstract | 127 |
| 5.2 Introduction | 128 |
| 5.3 OFET results for DPP Linear-c compound | 133 |
| 5.4 Effect of ODTS and HMDS treatment of SiO ₂ substrates on device performance of OFETs with DPP Linear-c as an active layer: | 136 |
| 5.5 Conclusions | 139 |
| Chapter 6 | 140 |
| 6.1 Abstract | 141 |
| 6.2 Introduction | 142 |
| 6.3 Results and discussion..... | 146 |
| 6.4 UV-Vis and CV spectra of the organic semiconductors 6.2b and 6.2e | 148 |
| 6.5 Atomic Force Microscopy and crystal data..... | 151 |
| 6.6 Conclusions | 154 |
| Chapter 7 | 156 |
| Chapter 8 | 161 |
| 8.1 OFETs fabrication and characterization..... | 162 |
| 8.1.1 5T-TTF oligomer | 162 |
| 8.1.2 DPP-TTF polymer | 163 |
| 8.1.3 5T-Ge cruciform | 165 |
| 8.1.4 DPP Linear-c macromolecule | 165 |

| | |
|--|-----|
| 8.2 Solar cell fabrication and characterization | 166 |
| 8.3 Synthesis..... | 167 |
| 8.3.1 Synthesis of 2,2'-(perfluoro-1,4-phenylene)dithiophene (6.2a) and 2,5-bis(2,3,5,6-tetrafluoro-4-(thiophen-2-yl)phenyl)thiophene (6.2b) | 168 |
| 8.3.2 Synthesis of (perfluoro-1,4-phenylene)bis(thiophene-5,2-diyl))bis(trimethylstannane) (6.2d) | 171 |
| 8.3.3 Synthesis of 5,5'-(perfluoro-1,4-phenylene)bis(2-(perfluorophenyl)thiophene) (6.2e) | 171 |
| 8.4 Atomic force microscopy (AFM)..... | 174 |
| 8.5 X-ray diffraction (XRD)..... | 175 |
| Chapter 9 | 176 |
| 9.1 References | 177 |

Table of figures

| | |
|--|----|
| Figure 1.1: Schematic representation of Electronic Band Structure | 20 |
| Figure 1.2: Doping of materials either by electron gain or electron loss | 21 |
| Figure 1.3: Doping creates pseudo energy level favours low band gap..... | 22 |
| Figure 1.4: Oxidation process (transfer electron from solution)..... | 23 |
| Figure 1.5: Reduction process (transfer electron from Electrode)..... | 23 |
| Figure 1.6: Typical plot of cyclic voltammogram (oxidation wave) ¹² | 24 |
| Figure 1.7: Visible spectrum | 26 |
| Figure 1.8: Excitation of Electrons from low energy level to high energy level by absorbing photon. | 27 |
| Figure 1.9: Absorption and emission spectrum of conjugated polymer (poly[2- methoxy, 5-(2-ethylhexoxy)-1,4-phenylene vinylene]), MEH-PPV..... | 28 |
| Figure 1.10: π -Cloud structure of Ethene..... | 29 |
| Figure 1.11: π - Lobe representation of 1,3 butadiene | 30 |
| Figure 1.12: Molecular orbital structure of 1,3 butadiene | 31 |
| Figure 1.13: Molecular structure of polyacetylene | 32 |
| Figure 1.14: π -Ring representation of benzene | 33 |
| Figure 1.15: π -Orbital structure of Thiophene | 34 |
| Figure 1.16: Working principle of OFETs..... | 36 |
| Figure 1.17: Illustration of typical bottom gate structures with a) Bottom drain and source b) top drain and source electrodes. | 38 |
| Figure 1.18: Illustration of typical top gate structures with a) Bottom drain and source b) top drain and source electrodes. | 39 |
| Figure 1.19: OFET device operation..... | 40 |
| Figure 1.20: Typical output characteristics with various gate-source voltages of (V_{GS}) | 42 |
| Figure 1.21: Typical transfer characteristics with fixed voltage of drain-source (V_{DS}) | 43 |
| Figure 1.22: Schematic layout of a BHJ solar cell. A part of the active layer is enlarged to illustrate the types of active materials. | 44 |
| Figure 1.23: Steps and mechanism of light to electric power conversion. Light which is not converted into electricity is converted into heat and eventually contributes to losses by excitation decay and recombination processes. ⁴⁹ | 45 |
| Figure 1.24: PC ₆₁ BM (left) and the α -type chiral isomer of PC ₇₁ BM (right) | 48 |
| Figure 1.25: I-V characteristic of an organic solar cell under dark, and under illuminated condition (left) and equivalent circuit diagram of solar cell with shunt (R_P) and series resistance (R_S) (right)..... | 49 |

| | |
|---|-----|
| Figure 2.1 : Output characteristics (2.1a, left) and transfer characteristics (2.1b, right) of OFET fabricated by spin-coating 5T-TTF from chloroform on Si/SiO ₂ substrates with untreated gold electrode | 69 |
| Figure 2.2: AFM image of 5T-TTF film cast from chloroform solution on Si/SiO ₂ substrate..... | 70 |
| Figure 2.3: Output characteristics (2.3a, left) and transfer characteristics (2.3b, right) of OFET fabricated by spin coating 5T-TTF from its chloroform solution on Si/SiO ₂ substrates with PFBT treated gold electrode..... | 71 |
| Figure 2.4: AFM image of 5T-TTF thin film spin cast from chloroform solution on Si/SiO ₂ substrate with PFBT treated Au electrode. | 71 |
| Figure 2.5: Output characteristics (2.5a, left) and transfer characteristics (2.5b, right) of OFET fabricated by spin-coating 5T-TTF from chlorobenzene on Si/SiO ₂ substrates with PFBT treated gold electrode..... | 73 |
| Figure 2.6: AFM image of 5T-TTF film cast from chlorobenzene solution on Si/SiO ₂ substrate..... | 73 |
| Figure 2.7: Output characteristics (2.7a, left) and transfer characteristics (2.7b, right) of OFET fabricated by spin-coating 5T-TTF from chloroform on ODTs treated Si/SiO ₂ substrates with PFBT treated gold electrode..... | 74 |
| Figure 2.8: AFM image of 5T-TTF film spin-coated from chloroform solution on ODTs treated Si/SiO ₂ substrate. | 74 |
| Figure 2.9 : Current density-voltage characteristics under dark and illumination (2.9a, left) for OPV fabricated by spin-coating from chloroform and AFM image in tapping mode of 5T-TTF: PC ₇₁ BM (1:4) active layer deposited from chloroform (2.9b, right) | 80 |
| Figure 2.10 Current density-voltage characteristics under dark and illumination (2.10a, left) for OPV fabricated by spin-coating from o-dichlorobenzene and AFM images in tapping mode of 5T-TTF: PC ₇₁ BM (1:4) active layer deposited from o-dichlorobenzene (2.10b, right) | 81 |
| Figure 3.1: The general structure of a DPP-based D–A molecule (DBT) | 87 |
| Figure 3.2: Chemical structure of diketopyrrolopyrrole-tetrathiafulvalene polymer, p(DPP-TTF) | 97 |
| Figure 3.3: Output characteristics of OFETs fabricated by spin-coating of p(DPP-TTF) from chlorobenzene (3.3a, left) and chloroform (3.3b, right) solutions. Measurements at gate voltage intervals of -10V in a top gate configuration..... | 99 |
| Figure 3.4: Transfer characteristics of OFETs fabricated by spin coating of p(DPP-TTF) from chlorobenzene (left) and chloroform (right), measured in a top gate configuration at V _{ds} of -70V (upper panels) and at V _{ds} of -20V (for CB, left bottom panel) and -15V (for CF, right bottom panel)..... | 99 |
| Figure 3.5: Tapping mode AFM height images of p(DPP-TTF) using chlorobenzene (3.5a, left) and chloroform (3.5b, right) as solvents on PFBT and ODTs treated SiO ₂ surfaces after annealing at 200°C for half an hour..... | 102 |

| | |
|--|-----|
| Figure 3.6: Output characteristics (3.6a, left) and transfer characteristics (3.6b, right) of p(DPP-TTF) in chloroform on ODTs treated Si/SiO ₂ substrates..... | 102 |
| Figure 3.7: I/V curves (left) of OPV fabricated by spin coating of p(DPP-TTF):PC ₇₁ BM (1:4) blend from chloroform solution after annealing at 120°C. AFM image (right) of p(DPP-TTF):PC ₇₁ BM films spin-coated on ITO/PEDOT:PSS substrates and annealed at 120°C for 20 minutes | 105 |
| Figure 3.8: I/V curves (left) of OPV fabricated by spin coating of p(DPP-TTF):PC ₇₁ BM (1:4) blend from o-dichlorobenzene solution after annealing at 120°C. AFM image (right) of p(DPP-TTF):PC ₇₁ BM films spin-coated on ITO/PEDOT:PSS substrates and annealed at 120°C for 20 minutes | 105 |
| Figure 3.9: AFM images of p(DPP-TTF):PC ₇₁ BM films spin-coated on ITO/PEDOT:PSS substrates and annealed at 120°C for 20 minutes. Height images for 1:5 (A) and 1:6 (B) blend ratios from o-dichlorobenzene..... | 106 |
| Figure 3.10: I/V characteristics (left) for p(DPP-TTF) as a single component OPV and AFM height image (right) of pure polymer DPP-TTF film spin-coated on ITO/PEDOT: PSS substrates and annealed at 120°C for 20 minutes. | 107 |
| Figure 4.1: Generic spirocentre structure..... | 111 |
| Figure 4.2: Output characteristics (4.2a, left) and transfer characteristics (4.2b, right) of device fabricated by spin-coating 5T-Ge from chloroform on Si/SiO ₂ substrates with PFBT treated gold electrode | 117 |
| Figure 4.3: AFM image of 5T-Ge film spin cast from chloroform solution on Si/SiO ₂ substrate..... | 118 |
| Figure 4.4: Output characteristics (4.4a, left) and transfer characteristics (4.4b right) of OFET fabricated by spincoating 5T-Ge from chlorobenzene solution on PFBT treated gold electrode containing Si/SiO ₂ substrates | 119 |
| Figure 4.5: AFM image (4.5a, left) of 5T-Ge film spin-cast from chlorobenzene solution on Si/SiO ₂ substrate and annealed straight at 120°C; (4.5b, right) OFET device XRD pattern of crystalline 5T-Ge film (black line) compared with that calculated from single crystal X-ray data (blue line) and separate reflexes (red bars with hkl indices marked above by red font) the 2θ value of which coincide with the maxima positions of experimental pattern (shown in black font)..... | 120 |
| Figure 4.6: Output characteristics (4.6a, left) and transfer characteristics (4.6b, right) of OFET fabricated by spin-coating 5T-Ge from chlorobenzene solution on Si/SiO ₂ substrates with PFBT treated gold electrodes without any annealing. | 122 |
| Figure 4.7: Output characteristics (4.7a, left) and transfer characteristics (4.7b, right) of OFET fabricated by spin-coating 5T-Ge from chlorobenzene solution on Si/SiO ₂ substrates with PFBT treated gold electrodes after being step-annealing from to 120°C in 20 minutes steps..... | 122 |
| Figure 4.8: Tapping mode AFM images of Ge-cruciform annealed at 120°C for 20 minutes after subsequent annealing at 50, 75, 100°C for 20 minutes | 123 |

| | |
|---|-----|
| Figure 5.1: Output characteristics (5.1a, left) and transfer characteristics (5.1b, right) of the device fabricated by spincoating of DPP Linear-c from chloroform solution on PFBT treated gold electrode annealed at 140°C for half an hour | 134 |
| Figure 5.2: Tapping mode AFM images of DPP Linear-c thin film spin cast from chloroform solution on SiO ₂ substrate after annealing at 140°C for half an hour.... | 134 |
| Figure 5.3: Output characteristics (5.3a, left) and transfer characteristics (5.3b, right) of devices fabricated by spin-coating of DPP Linear-c from chlorobenzene solution on Si/SiO ₂ substrates with PFBT treated gold electrode..... | 135 |
| Figure 5.4: Tapping mode AFM images of DPP Linear-c thin film spin-cast from chlorobenzene solution on SiO ₂ substrate and annealed at 140°C for half an hour. | 136 |
| Figure 5.5: Output characteristics (5.5a, left) and transfer characteristics (5.5b, right) of OFET fabricated by spin-coating of DPP Linear-c from chloroform solution on PFBT and ODTS treated Si/SiO ₂ substrates and annealed at 140°C | 137 |
| Figure 5.6: Output characteristics (5.6a, left) and transfer characteristics (5.6b, right) of OFET fabricated by spin-coating of DPP Linear-c from chloroform solution on PFBT and HMDS treated Si/SiO ₂ substrates and annealed at 140°C | 137 |
| Figure 5.7: Tapping mode AFM image of DPP Linear-c film spin-cast from chloroform solution on ODTS modified SiO ₂ substrate (5.7a, left) and on HMDS modified SiO ₂ substrate (5.7b, right), after being annealed at 140 °C for half an hour. | 138 |
| Figure 6.1: Absorption and emission spectra of 2, 5-bis (2, 3, 5, and 6-tetrafluoro-4-(thiophen-2-yl) phenyl) thiophene (6.2b) measured in CH ₂ Cl ₂ | 148 |
| Figure 6.2: Monomer oxidation (left) and reduction (right) of ca. 9.9 x10 ⁻⁵ M CH ₂ Cl ₂ solution of 2,5-bis(2,3,5,6-tetrafluoro-4-(thiophen-2-yl)phenyl) thiophene (6.2b), on a glassy carbon working electrode, with an Ag wire reference electrode, Pt counter electrode, , 0.1 M TBAPF ₆ as supporting electrolyte, at a scan rate of 100mVs ⁻¹ . The data is referenced to the Fc/Fc+ redox couple..... | 149 |
| Figure 6.3: Absorption and emission spectra of 5, 5'-(perfluoro-1, 4-phenylene) bis (2-(perfluorophenyl) thiophene (6.2e) measured in CH ₂ Cl ₂ respectively | 150 |
| Figure 6.4: Oxidation (left) and reduction (right) of the compound 6.2e (ca. 10 ⁻⁴ M in CH ₂ Cl ₂) on a glassy carbon working electrode, with Ag wire reference electrode, Pt counter electrode, 0.1 M TBAPF ₆ as supporting electrolyte at a scan rate of 100mVs ⁻¹ . The data is referenced to the Fc/Fc+ redox couple..... | 150 |
| Figure 6.5: Atomic Force Microscopic images of compound 6.2b (A) and 6.2e (B) and blend of two compounds 6.2b and 6.2e (C) | 152 |
| Figure 6.6: Crystal structure and interplanar distance of compound (6.2b) (2,5-bis(2,3,5,6-tetrafluoro-4-(thiophen-2-yl)phenyl) thiophene) | 153 |
| Figure 6.7: π - π Stacking herringbone structure of compound (6.2b) 2,5-bis(2,3,5,6-tetrafluoro-4-(thiophen-2-yl)phenyl) thiophene | 154 |
| Figure 8.1: ¹ H NMR spectrum of 2,5-bis(2,3,5,6-tetrafluoro-4-(thiophen-2-yl)phenyl)thiophene (6.2b)..... | 172 |

| | |
|--|-----|
| Figure 8.2: ¹ H NMR spectrum of ((perfluoro-1,4-phenylene)bis(thiophene-5,2- diyl))bis(trimethylstannane) (6.2d) | 173 |
| Figure 8.3: ¹ H NMR spectrum of 5,5'-(perfluoro-1,4-phenylene)bis(2- (perfluorophenyl)thiophene) (6.2e)..... | 174 |
| Figure 8.4: Schematic representation of atomic force microscopy..... | 175 |

Table of Chart

| | |
|--|-----|
| Chart 2.1 : Redox Transformation of Tetrathiafulvalene, TTF..... | 58 |
| Chart 2.2 : Tetrathiafulvalene (TTF) derivatives | 60 |
| Chart 2.3: Unsubstituted and substituted oligothiophenes | 63 |
| Chart 2.4: Alkyl substituted oligothiophenes at terminal position..... | 65 |
| Chart 2.5: Linear conjugated oligothiophenes as π -dimeric model | 66 |
| Chart 2.6: Fused TTF poly (thiophene)s and oligothiophenes previously developed in the Skabara group. | 67 |
| Chart 3.1: structures of DPP-based copolymers with a fused thienothiophene and non-fused thiophene donor moieties. | 89 |
| Chart 4.1: Compounds containing spirocyclic bis (dithiolate) as the central atom of 'Ge' and 'Si' centres | 113 |
| Chart 4.2: New spirobi([1,3,2]dithiagermole molecule. | 115 |
| Chart 5.1: An illustration of the fluorene structure showing numbering of sites available for substitution, and alkyl groups to its 9-position | 128 |
| Chart 5.2: Quaterfluorene conjugated systems alongside the corresponding DPP cores. b) Star DPP b) DPP Linear-c c) DPP Linear-nc | 130 |
| Chart 5.3: Schematic representation of a) 1D and b) 2D interactions between molecules in DPP aggregates. | 131 |
| Chart 6.1: List of oligomers 6.1a-6.1e | 143 |
| Chart 6.2: Synthesis of the compounds 2, 5-bis (2, 3, 5, 6-tetrafluoro-4-(thiophen-2-yl) phenyl) thiophene (6.2b) and 5, 5'-(perfluoro-1, 4-phenylene) bis (2-(perfluorophenyl) thiophene (6.2e) | 146 |

Table of tables

| | |
|---|-----|
| Table 2.1: FET characteristics of vacuum and solution processed thin-film devices based on TTF derivatives..... | 62 |
| Table 2.2: Organic Field Effect Transistor mobility of oligothiophenes | 64 |
| Table 2.3: Device configurations produced with various SAM reagents and solvents..... | 69 |
| Table 2.4: Photovoltaic parameters of TTF based organic semiconductors prepared by solution and vacuum evaporation techniques | 78 |
| Table 2.5: A collection of the data obtained for solar cell devices: Power Conversion Efficiency (η), open circuit voltage (V_{oc}), short circuit current density (J_{sc}), and fill factor (FF) | 81 |
| Table 3.1: High mobility DPP-based compounds for OFETs..... | 92 |
| Table 3.2: OPV results based on DPP-based copolymers..... | 94 |
| Table 3.3: OFET performance for devices of various configurations fabricated using different solvents..... | 98 |
| Table 3.4: Comparison of device characteristics for OPV fabricated with using different solvents and annealed at 120°C. Here, J_{sc} is the short circuit current density, V_{oc} is the open-circuit voltage, FF is the fill factor, and η is the overall power conversion efficiency. | 106 |
| Table 4.1: Device configurations varied using different solvents..... | 117 |
| Table 5.1: The electrical performance of DPP Linear-c OFET devices using various dielectrics | 133 |
| Table 6.1: HOMO and LUMO levels, mobility (μ), and band gap values for compounds 6.1a-e..... | 144 |
| Table 6.2: Representation of Oxidation, reduction, HOMO-LUMO, and Band gap values for compounds 6.2b and 6.2e..... | 150 |
| Table 8.1: Experiments with various ratios of reagents and various reaction conditions ... | 170 |

Chapter 1

Introduction and Background

1.1 Organic semiconductors

Semiconductors, having been initially developed on the basis of crystalline inorganic materials, revolutionized electronics leading to the advance of faster electronic devices (high speed communication).¹ They found widespread applications in computer science, display technology, energy conversion devices. Because of overlapping electronic orbitals in their crystalline arrangement, the atomic states create a band structure with well-defined energy-momentum dispersion which describes the behaviour of electrons and holes in the conduction and in the valence bands respectively. Novel classes of organic semiconductors (OSC's) are an alternative to their inorganic analogues because of their flexibility, low cost, easy processability that permits the attainment of thin films of the material over large areas and the tunability of their properties through chemical modification or variation of their morphology. OSC's have extensively been used for electronic and photonic devices such as organic light-emitting diodes (OLEDs)², organic semiconductor lasers (OSLs)³, organic field effect transistors (OFETs)⁴, organic photovoltaics (OPVs)⁵, sensors⁶, and electrochromic devices.⁷

Different classes of organic semiconductors are conjugated polymers and small conjugated molecules. The following examples fit into the first group: poly (3-hexylthiophene), poly (p-phenylene vinylene), polyacetylene and its derivatives. Examples of conjugated small molecules are pentacene, anthracene and rubrene. Solids are classified as insulators, conductors and semiconductors by the availability of charge carriers (electrons and holes) for conducting electric current. Therefore, it

is essential to start with band theory, which gives an explanation about electrical properties and accounts for the presence of charge carriers (holes and electrons).

1.2 Band theory

In organic semiconductors, the overlap between π -electronic orbitals of adjacent molecules results in the splitting of HOMO (LUMO) and creates valence (conduction) band. The valence and conduction bands determine the hole and electron mobilities respectively. For simple cosine-shaped bands, the higher the HOMO (LUMO) bandwidth, the higher the expected hole (electron) mobility.⁸

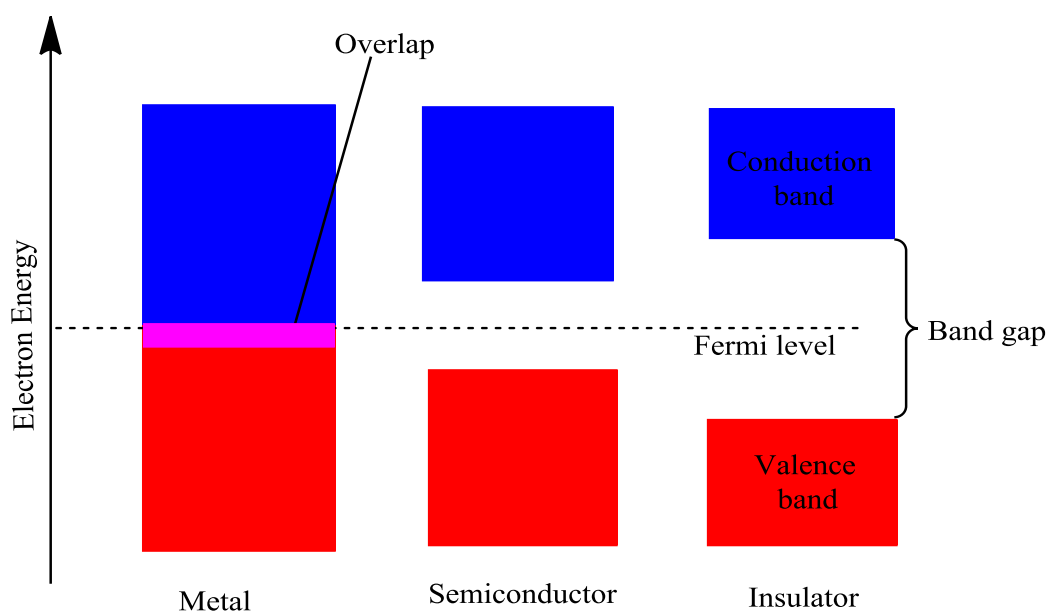


Figure 1.1: Schematic representation of Electronic Band Structure

The energy difference between these two energy bands is called the band gap; (E_g) or energy gap. The electrons in a semiconductor are characterized by the Fermi level (E_f), and for undoped semiconductor at $T \approx 0$ it is located in the middle of band gap. If the

electron effective mass (m_c) equals to the hole effective mass (m_v), E_f level does not change with increasing temperature. In metals the Fermi level coincides with the highest occupied energy state (figure 1.1). The magnitude of the band gap, E_g determines whether a material is a conductor, semiconductor, or an insulator. In metals, there is no energy gap ($E_g = 0\text{eV}$) between the occupied and unoccupied energy levels meaning that, electrons can move freely all over the metals volume due to the fact that any small perturbation leads to an instant change in their energy. In semiconductors the band gap, $E_g (>0 - 2.5\text{eV})$ is small and allows for electrons to be promoted to the conduction band by thermal excitation which contributes to an electrical conductivity. Insulating materials exhibit a very large $E_g (> 3\text{eV})$. So upon thermal excitation alone, no electrons can reach the conduction band and hence these materials do not conduct electricity.⁹

1.3 Doping of materials

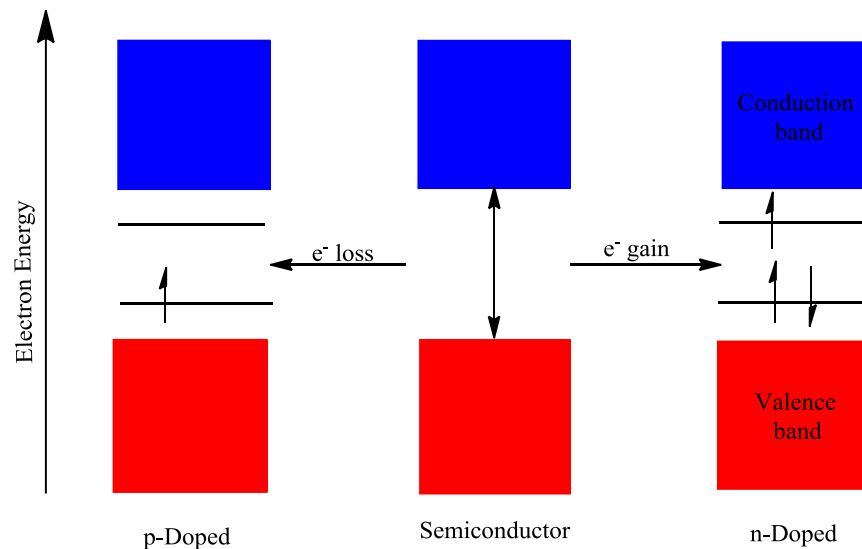


Figure 1.2: Doping of materials either by electron gain or electron loss

With the addition of dopants, (figure 1.2) the conductivity of the semiconductors can be increased either by positive or negative doping, which can be introduced physically, chemically or electrochemically. p-Doping results in positive charges in the valence band and involves the ejection of an electron leaving a vacant positive hole. A neighbouring electron can move into that hole, leaving another positive hole and this endows the semiconductor with conductivity.¹⁰ According to the band theory (figure 1.3) p-doping results in new localized vacant energy levels (E_a) located just above the valence band, electrons upon thermal excitation are promoted to those levels leaving positive vacant ‘holes’ in the valence band and the material becomes a conductor with positively charged holes as free charge carriers. Upon n-doping, new occupied energy levels just below the conduction band are created. Now, a promotion of the electrons from those levels to the conductance band by thermal excitation creates electron charge carriers.

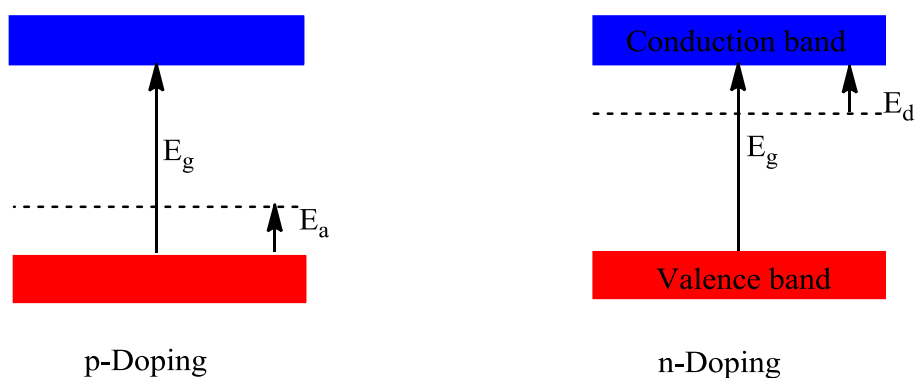


Figure 1.3: Energy levels E_a and E_d , which are created by p- and n- doping of semiconductors respectively.

1.4 Oxidation and reduction

For a semiconductor on an electrode surface, electrochemical doping can be achieved by the simple process of oxidation and reduction reactions. By applying the external

electric field through the working electrode, which is immersed into the analyte solution, an electrochemical cell can be operated. An oxidation involves the loss of an electron. The ability of compounds to be oxidized depends on their ionization potential. Upon oxidation the energy level of electrons on electrodes (Fermi level) should be lower than the HOMO level of the compound to allow the transfer of electrons to the electrode, which acts as an electron-acceptor.

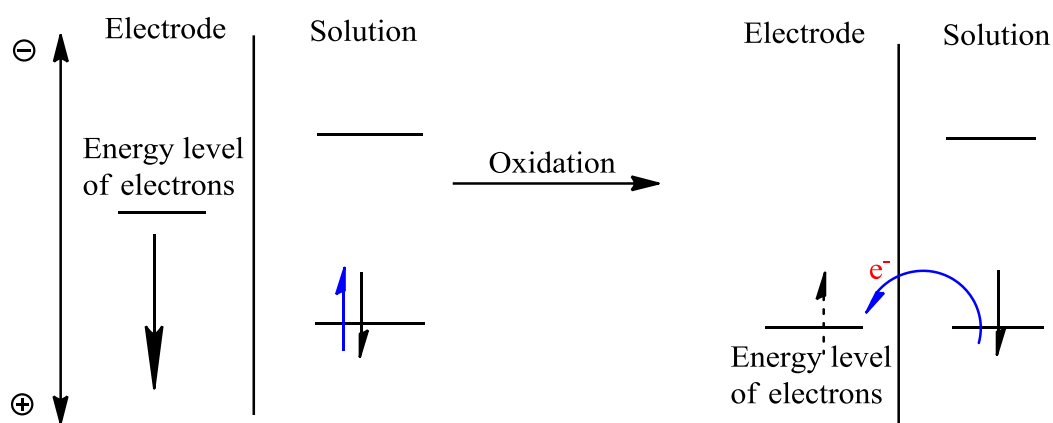


Figure 1.4: Oxidation process (transfer electron from solution)

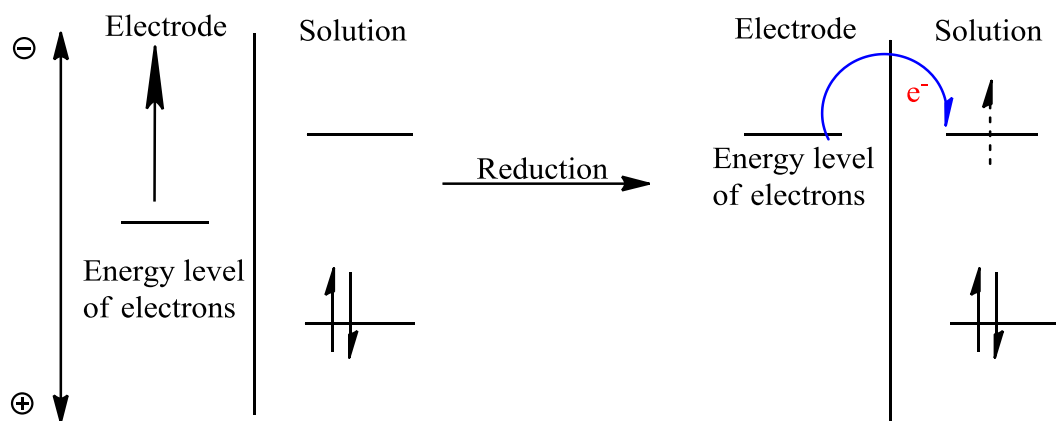


Figure 1.5: Reduction process (transfer electron from electrode)

It can be achieved by applying a positive potential to the electrode (figure 1.4). During oxidation an anodic current is created. Similarly, a reduction involves the gain of an

electron. The ability to n-dope compounds depends upon their electron affinity; the LUMO level of the material should be lower than the energy level of electrons at the electrode to allow transfer of electrons to the material, which acts as an electron-acceptor. It can be achieved by applying a negative potential, a cathodic current being created¹¹ (figure 1.5).

Cyclic voltammetry is a tool, which provides practical information about the redox (oxidation and reduction) properties of the target materials. It is a versatile electro analytical measurement technique serving a wide range of scientific fields. It is a very important tool for organic electronics research because it helps to estimate the energy levels of the organic compounds. The ionization potential is related to the HOMO energy level of the material and the electron affinity to its LUMO level.

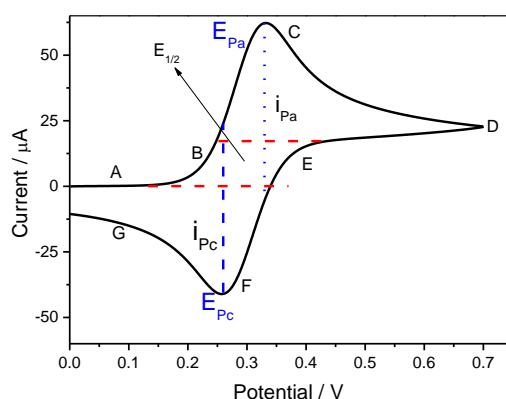


Figure 1.6: Typical plot of cyclic voltammogram (oxidation wave)¹²

We interpret the unique shape of the oxidation wave cyclic voltammogram shown in figure 1.6. The forward scan of the potential is in the positive direction (A). The potential sweeps linearly from 0V (A) to its maximum value (D) (forward scan) and backwards – reverse scan from (D) to (G). When the potential reaches a

sufficiently positive potential at (B) the anodic current starts to grow due to the oxidation, according to equation 1.



The anodic current increases rapidly (B-C) until the analyte X is depleted near the electrode surface providing the maximum of the concentration gradient and consequently the peak current at (C). After depletion of X at the electrode surface the oxidation of the analyte coming from the more remote part of diffusion layer leads to decrease in gradient and consequently in the current. The direction of the scan is switched backwards at (D) for the reverse scan. When the potential reaches a sufficient value for reduction at (E), the accumulated X^+ around the electrode can now be reduced back to the neutral analyte by the electrode process (Equation 2).



The cathodic current increases rapidly in the negative direction during (E to F), until the oxidised form of analyte X^+ is depleted at the electrode surface causing the current to reach maximum at F and decay from F to G as the concentration of X at the surface of the electrode is back to the initial one. The first cycle is completed when the potential returns back to the initial potential, E_i . If we sweep the potential in the negative direction for direct scan the cyclic voltammetry response is called the reduction wave because the process starts with the reduction reaction of X to X^- and gives a cathodic current (Equation 3) followed by oxidation of X^- to X producing an anodic current (Equation 4).



For a reversible redox process in which electron transfer step is fast enough to limit the rate by diffusion, the anodic and cathodic peak currents are equal, and the ratio i_{pa}/i_{pc} is 1. The half-wave potential, $E_{1/2}$, is an average of the anodic and cathodic peak potentials. The difference between potential of anodic and cathodic peaks ($E_p = E_{pc} - E_{pa}$) is close to $59/n$ mV at 25°C and independent of the scan rate, where 'n' is the number of electrons involved in the redox process.^{12, 13} The onsets of the first oxidation and reduction peaks of the materials can be converted to the HOMO and LUMO energy levels of monomer or polymer by subtracting them from the HOMO of ferrocene, which has a known value of -4.8eV.^{14, 15} Finally, the difference between HOMO and LUMO energy levels provides HOMO-LUMO gap value.¹⁶

1.5 Absorption and emission

In organic semiconductors the bonding and anti-bonding orbitals create two pseudo continua of energy levels separated by an energy gap. This allows the material to have a band like electronic structure which determines not only electronic but optical properties as well.

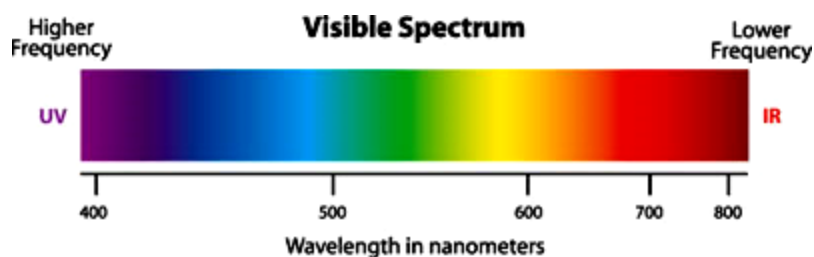


Figure 1.7: Visible spectrum

Optical spectroscopy is thus an invaluable tool to probe the properties of these materials. The absorption of light in a molecule is governed by the interaction of the

electromagnetic radiation field with the material. Due to the presence of certain functional groups called chromophores in a particular compound, the latter possesses colours, see figure 1.7. When a sample containing atoms or molecules is subjected to light, sufficient energy can be absorbed and this causes the electronic structure to become excited to a higher energy level. Initially, an atom or a molecule in the ground state fills its electrons into the lowest energy orbitals and once sufficient excitation energy is received these electrons can be promoted to higher energy levels or anti-bonding orbitals, as shown in the figure 1.8. In other words, a photon may be absorbed from the field, and an electron is excited to a higher energy state, if the energy of the photon corresponds to the energy gap between the ground and excited state of the material.

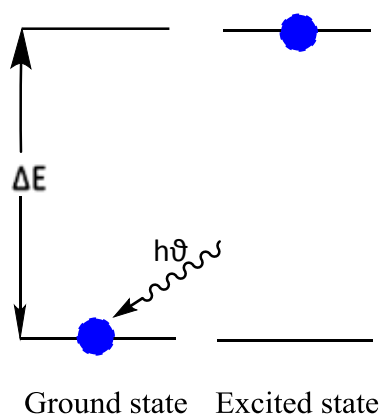


Figure 1.8: Excitation of Electrons from low energy level to high energy level by absorbing photon.

The energy of the photon ($h\nu$) absorbed during excitation transition is given by the equation 5:

$$E = h\nu \quad (5)$$

Where: h is Planck's constant and equals to 6.626×10^{-34} Js, ν is the frequency of the photon, in Hz. The frequency can be expressed in terms of wavelength and c , the velocity of light in vacuum. ($c = 3.0 \times 10^8$ ms⁻¹)

$$\nu = c/\lambda \quad (6)$$

Wavelength, λ , indicates the distance between two consecutive peaks (such as crests or troughs from the travelling waves). The equations 5 and 6 can be combined, providing equation 7.

$$E = hc/\lambda \quad (7)$$

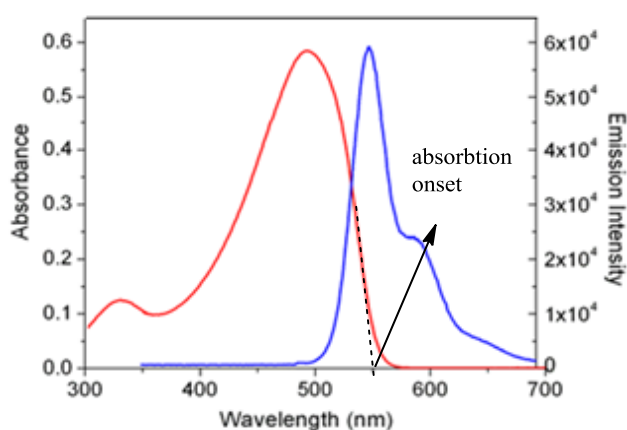


Figure 1.9: Absorption and emission spectrum of conjugated polymer (poly[2-methoxy, 5-(2-ethylhexoxy)-1,4-phenylene vinylene]), MEH-PPV.

The band gap energy (E_g) in electron volts (eV) is calculated from the wavelength λ_{onset} in nm of a photon by this equation (7):

$$E_g = hc / \lambda_{onset} = ((4.14 \times 10^{-15} \text{ eV s})(3 \times 10^{17} \text{ nm s}^{-1})) / \lambda_{onset} (\text{nm}),$$

which can be reduced to give $E_g = 1240/\lambda_{onset}$. Figure 1.9 shows optical absorption and emission spectra of the well-known conjugated polymer (poly[2-methoxy-5-(2-ethylhexoxy)-1,4-phenylene vinylene]), MEH-PPV.¹⁷ The broad absorption band is usually explained by the disordered nature of the polymer chain in the ground state,

meaning that polymer chains are twisted and folded leading to breaks in the conjugation and contains many shorter conjugated segments.

1.6 π -Bonding as an essential feature of organic semiconductor

To explain the structure-properties relationship for organic semiconductors, the nature of chemical bonds will be summarized. In conjugated molecules, carbon atoms are covalently bonded by alternating single and double bonds. The π -electron density is considered to be evenly distributed across the molecule and will not confine on multiple bonds. π -Bonds are formed from overlapping adjacent atomic p-orbitals above and below the plane of the molecule. Since they are out of the plane, these orbitals can interact with each other freely, and become delocalized.¹⁸ Ethene has two carbon atoms connected by a double bond and each of these two atoms is connected with two hydrogen atoms by single bonds. There are four electrons in the outer shell of a carbon atom and it has an electronic configuration of $1s^2 2s^2 2p^2$. Upon hybridization one of 2s-electron is promoted to a vacant 2p-orbital, creating virtual $1s^2 2s^1 2p^3$ state, with all three p-electron being on different 2p-orbitals according to Hund's rule. The two p electron orbitals of carbon mix with the 2s-orbital to form three degenerated (threefold axial local symmetry) sp^2 -hybridized orbitals, leaving the last valence electron in a p orbital. These three hybrid orbitals lie in one plane at 120° angles to each other and have a lower energy than the p-orbital.

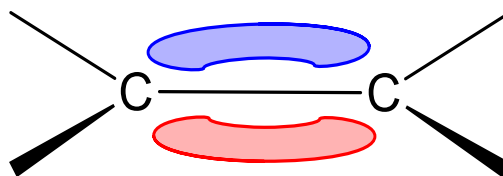


Figure 1.10: π -Cloud structure of Ethene

This difference in energy is the driving force for hybridization. When two carbon atoms are close to each other, the two sp^2 -orbitals overlap to form a single σ -bond and the remaining p orbitals on each carbon atom overlap with each other above and below the plane of the molecule, which leads to a π -bond formation as shown in figure 1.10. If two double bonds similar to that described above are located close to each other in one molecule and separated by one single bond, they interact with each other. This interaction is called conjugation. The concept of conjugation is better to trace on an example of 1,3-butadiene. All four carbons in this molecule are sp^2 -hybridized. The planar arrangement and the alignment of the p-orbitals allow overlap between two double bonds. The electrons are delocalized over the full length of the molecule. This delocalization of electrons creates partial double bond character between C2 and C3 (figure 1.11). A MO diagram shown in the figure 1.12 explains chemical bonding in the molecule in terms of MO (LCAO) theory. 1,3-Butadiene has 4 π -electrons, and each MO can accommodate two of them.

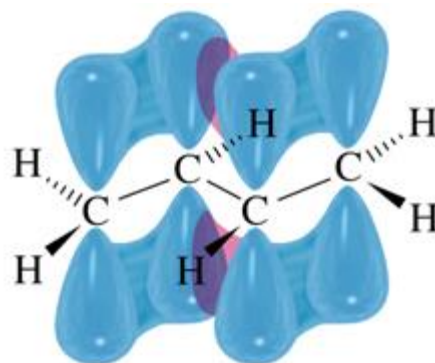


Figure 1.11: π - Lobe representation of 1,3-butadiene

Generally molecules in ground state have occupied bonding MO's and vacant antibonding MO's. A π bonding orbital is formed by overlap of p-lobes with the same

wave function sign known as constructive overlap. An π anti-bonding orbital is formed by overlap of p-lobes with opposite wave function sign known as destructive overlap. Electrons have a lower energy in the bonding MO than in the original p orbitals, and a higher energy in the anti-bonding orbitals. The MO energies are symmetrically distributed above and below the initial energies of the p orbitals.

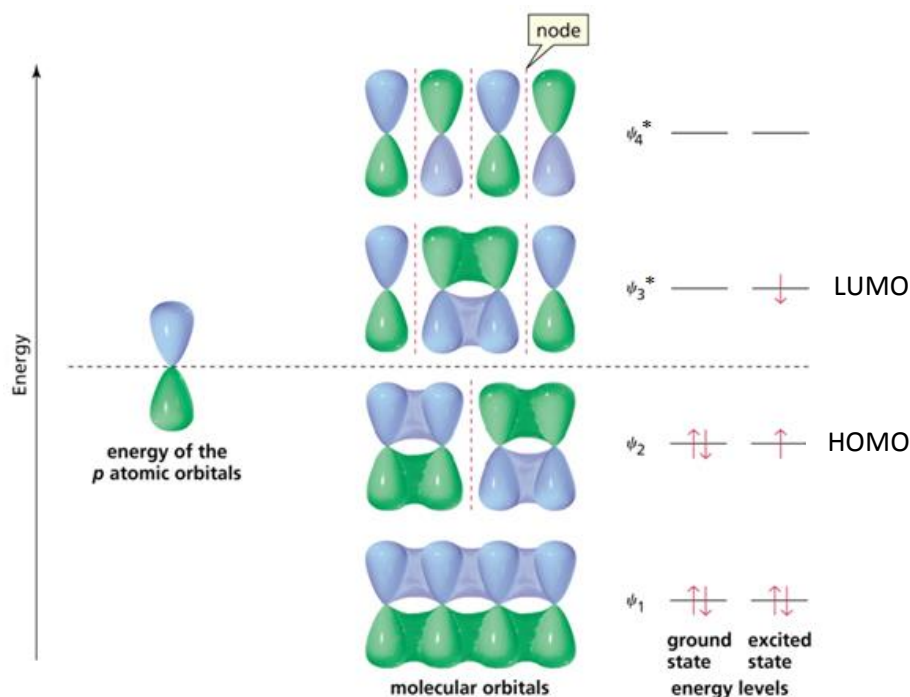


Figure 1.12: Molecular orbital structure of 1,3-butadiene (ground and excited state)

The lowest energy MO (ψ_1) will have the greatest number of favourable interactions in p lobes (interacting constructively). There are 3 bonding interactions and this MO is delocalized all over four nuclei. The next MO (ψ_2) has a node in the center of the molecule with bonding between C1-C2, and C3-C4, and there is an antibonding interaction between C2-C3. This MO has two bonding and one antibonding interaction, but overall it is considered as bonding, with the energy being higher than

that of ψ_1 , but lower than the energy of a p-orbital. This orbital is considered to be the highest occupied molecular orbital (HOMO) for butadiene neutral ground state. The third MO (ψ_3^*) has two nodes. Here, there are two antibonding and one bonding interactions, so this is an antibonding MO, and is denoted with an asterisk (*). This orbital is the lowest unoccupied molecular orbital (LUMO). The fourth MO (ψ_4^*) has 3 nodes, and is completely antibonding with highest energy. The orbitals ψ_1 and ψ_2 might be considered as a split local HOMO level of original isolated double bonds due to their conjugation, whereas the ψ_3^* and ψ_4^* orbitals are the product of a similar LUMO level splitting. Extending of alternating single-double bond unit into an infinite one dimensional chain creates the structure of the well-known organic semiconductor-polyacetylene (figure 1.13). In this polymer the conjugation of sp^2 -hybridized carbon atoms reaches its limit. Polyacetylene is the most illustrative example of conducting polymers. While doped it can attain conductivity that is close to that of silver. For the discovery of conducting organic polymers in 1977, the polymer chemist, Shirakawa,¹⁹ the organometallic chemist, MacDiarmid, and the physicist, Heeger²⁰ were awarded the Nobel Prize in Chemistry in 2000.

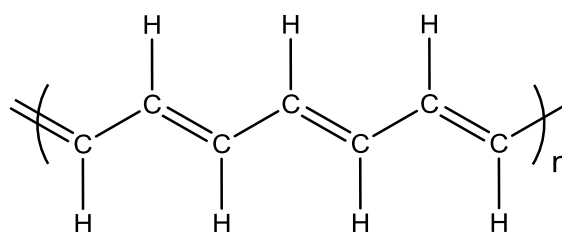


Figure 1.13: Molecular structure of polyacetylene

In a cyclic structure the conjugation of sp^2 carbon atoms manifest itself through the aromaticity. All six carbon atoms in benzene have four valence electrons, three of

which are involved to form the sigma bonds to each other and with the s orbitals of the six hydrogen atoms forming C-C and C-H sigma bonds. Also carbon atoms in benzene possess unhybridised p-orbitals which are aligned perpendicularly to the σ -bonds. The lateral overlap of these p-orbitals between neighbouring carbon atoms produces a π molecular orbital. This is called a conjugated π -system where the weakly bound π -electrons are said to be delocalized.

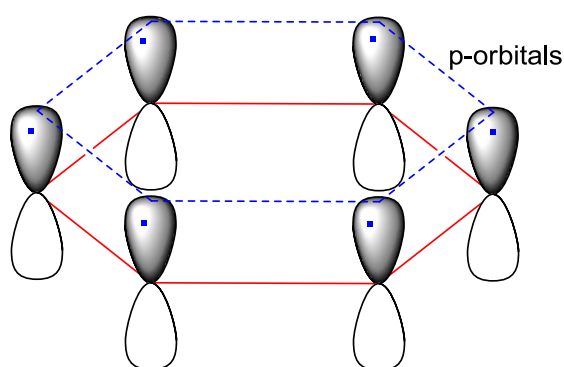


Figure 1.14: π -Ring representation of benzene

Based on Huckel's calculation, a planar cyclic molecule with alternating double and single bonds has aromatic stability if it has $4n+2$ π -electrons. For $n=1$: $4n + 2 = 6$, therefore, benzene is aromatic and the electrons are delocalized (figure 1.14). As the result of this delocalization, the π wave function is represented by a linear combination of p-orbitals from all six atoms. The weakly bound π -electrons can move along the carbon chain and overlap in the solids, contributing towards semiconducting properties.²¹

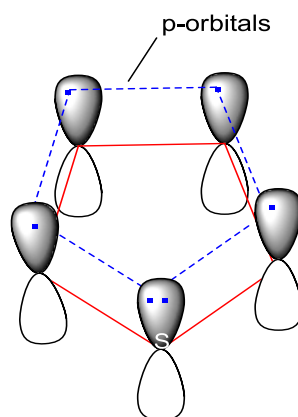


Figure 1.15: π -Orbital structure of Thiophene

In thiophene, the endocyclic atoms (4 carbons+1 sulfur) have sp^2 hybridized outer shells and these orbitals overlap with each other and with the s atomic orbitals of the four hydrogen forming C-C, C-S, and C-H σ -bonds. All these sigma bonds and sulfur's lone pair of electrons (not shown in figure 1.15) located in sp^2 -orbital lie in the plane of the ring. The p-orbitals of carbons contain one electron each and p-orbital of the sulfur contains two electrons (the second sulfur lone pair). These orbitals are perpendicular to the plane of sigma bonds as depicted in the figure 1.15. Their lateral overlap produces a molecular orbital containing six electrons which satisfies the Huckel's aromaticity rule ($4n+2$).

1.7 Operating principles and assembly of organic field effect transistors

Transistors are the fundamental building blocks, which are mainly used to amplify signal or as on/off switches. The field effect is the process in which conductivity of a semiconductor varies depending upon an electric field applied orthogonally to its surface. Organic field effect transistors normally comprise three different terminals, the source, drain, and gate. It contains a semiconductor layer and an insulating layer

between the semiconductor and the gate, as well. By applying the voltage between the source and gate, a charge can be induced in the semiconductor layer. The charge carriers are injected from the source electrode and collected across the conducting channel at the drain by applying a voltage between the two metals.²² In general, semiconductors are made from inorganic materials, such as silicon and germanium, but the technological and manufacturing limitations of these materials paved the way for research in the field of organic semiconductors, such as conjugated oligomeric or polymeric systems. The insulator can be made of a variety of dielectric materials, though silicon oxide (SiO_2) is a common choice.²³ To describe the operating principle of the organic field effect transistors, simple energy level diagrams of source-drain metal electrodes Fermi level and HOMO-LUMO levels of a semiconductor, are shown in figure 1.16. If there is no gate-source voltage applied, the organic semiconductor which is intrinsically undoped doesn't have any charge carriers. Due to high resistance of the undoped organic semiconductors the currents will be very low.^{24, 25}

When a negative gate voltage is applied as shown in the picture and the Fermi level of source/drain metal is close to the HOMO level of the organic semiconductor, positive charges by injection from the source are induced at the organic semiconductor area adjacent to the gate dielectric (p-type conducting channel is formed), and by applying a voltage, V_{ds} between drain and source one can detect a current through the channel I_{ds} . Such organic semiconductors with ability to conduct only positive charge carriers are said to be p-type semiconductors. Typical values of HOMO levels of p-type materials fall between -4.9 and -5.5eV , which results in good electrical contact with high work function metals, for e.g. gold -4.9eV .²⁶

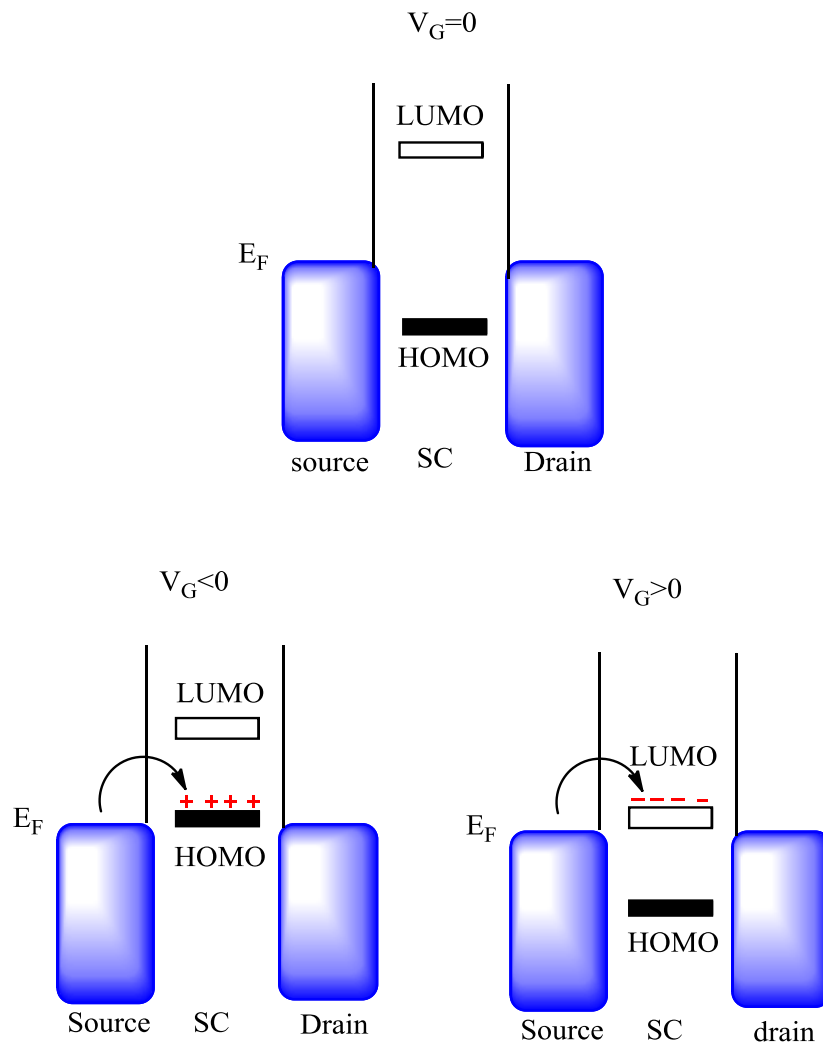


Figure 1.16: Working principle of OFETs.

When a positive voltage is applied to the gate, with the Fermi level of source/drain metal being close to the LUMO level of the organic semiconductor, negative charges are induced by injection from the source at the semiconductor-dielectric interface (n-type conducting channel is formed) and can be extracted by the drain by applying a voltage V_{ds} . Such organic semiconductors have the ability to conduct only negative charge carriers and are said to be n-type semiconductors. These n-type semiconductors have a low lying LUMO energy level (between -3 and -4eV) and exhibit high electron

affinity, that allows them to receive electrons from the metal electrodes upon applying a voltage.²⁷ OFETs belong to the class of thin-film transistors, where the semiconducting materials are deposited as a thin film on a substrate. Owing to this fact, OFETs are also referred to as Organic Thin-Film Transistors (OTFTs). In particular, the three important characteristics, used to evaluate the performance of organic semiconductors in field-effect transistor devices, are the threshold voltage V_{th} , the charge-carrier mobility (μ [cm^2/Vs]) and on/off current ratio (I_{on}/I_{off}). The threshold voltage V_{th} characterizes the voltage V_{gs} at which the field effect sets, meaning that it primarily relates to the number of the charge-carrier traps in the semiconductor channel. The charge mobility (μ) is the measure of the ability of electrons or holes to flow through the OFET semiconductor under an applied potential V_{ds} and defined as the velocity of charge carrier (V_c) at unit electric field:

$$\mu = \frac{V_c \cdot l}{V_{ds}} \quad (8)$$

Mobility of at least $1\text{cm}^2/\text{Vs}$ will be required for high-speed organic digital circuits, but in chemical sensors the lower mobilities ($0.01\text{--}0.1\text{cm}^2/\text{Vs}$) can also be acceptable. The on/off current ratio (I_{on}/I_{off}) is defined as the ratio of the current flow, between the source and drain electrodes in the on state and in the off state of the device.²⁸ Large I_{on}/I_{off} ratio is required²⁹ for application of OFETs in organic circuits and this can be achieved by enhancing the on current (e.g., through improvement of the charge injection from electrodes) and/or by reducing the off current, through the application of post-processing treatments such as annealing and optimization of the organic semiconductor purity. The charge-carrier mobility (μ) in turn eventually determines the magnitude of the voltage applied and also the power consumption of the transistor.

OFETs are generally prepared in four configurations as shown in figures 1.17(a-b) and 1.18(a-b). Two of these are the bottom gate with bottom and the top-contacts, the other two are top gate with bottom and the top-contacts.

Figure 1.17(a) shows the structure of bottom gate with bottom drain-source device. First of all, the substrates will be made from doped silicon with silicon dioxide layer. Doped silicon is used for the gate electrode whereas silicon dioxide grown on the top of the silicon acts as the insulating layer followed by the metal source and drain electrodes deposited on the silicon dioxide layer. Then, the OSC material is deposited directly on top of the electrodes, filling the gap between them. If a negative voltage V_{gs} is applied to the gate electrode, an electric field is induced perpendicular to the layers. As the consequence, positive charge carriers occur at the interface between semiconductor and gate insulator. At the same time a voltage, V_{ds} is applied at the drain electrode, holes can be transported from the source electrode to the drain electrode. This conducting state is called the “on” state; $V_{gs} \leq V_{th}$ defines the “off” state.^{26, 28, 30}

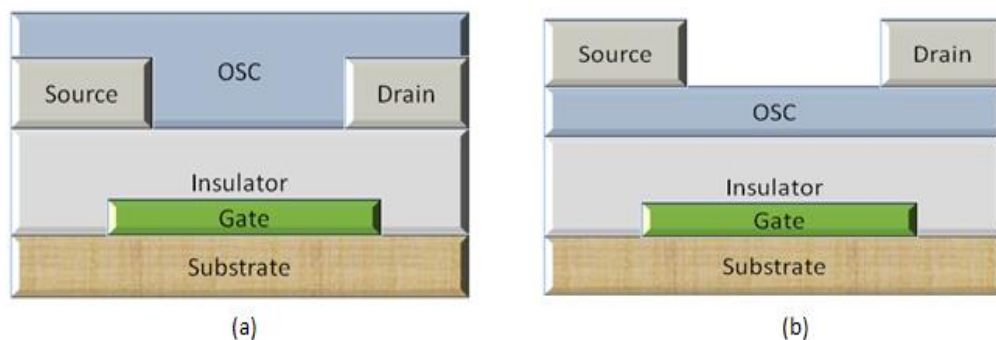


Figure 1.17: Illustration of typical bottom gate structures with a) Bottom drain and source b) top drain and source electrodes.

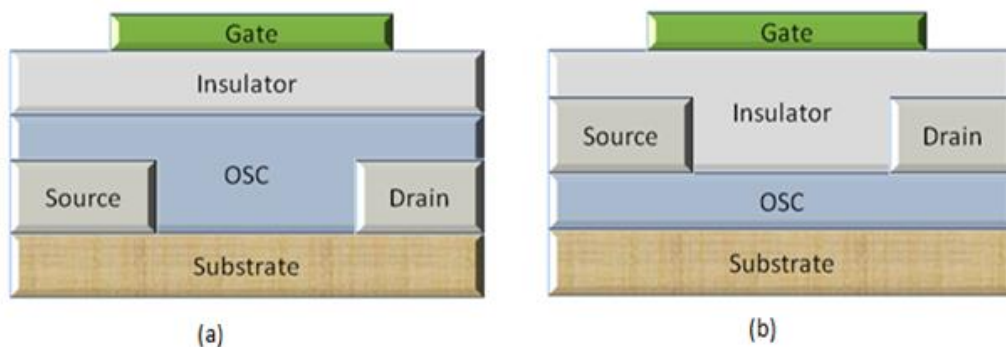


Figure 1.18: Illustration of typical top gate structures with a) Bottom drain and source b) top drain and source electrodes.

This device structure is suitable for both large-area applications and nanometer scale transistor design.²⁹ This architecture may be preferred, because the semiconductor layer does not have to be exposed to the potentially damaging chemicals needed to process subsequent layers. Fabrication of the top drain-source field effect transistor shown in figure 1.17(b) poses a challenge because many conventional fabrication processes damage the surface of van der waals bonded organic crystals or materials by disrupting molecular order, creating interfacial trapping sites and obstacles to charge injection. Figure 1.18(a-b) depicts the top gate configurations.

Even though the gate electrode is deposited on top of all other layers, the positions of source and drain electrodes are not similar. Advantages of these configurations are encapsulating the semiconducting layer between the substrate and the insulator layer. This provides more protection for organic semiconductor from an environment. In the case of figure 1.18(a) the electrodes are fabricated directly on the substrate which provides the larger contact area between the electrodes and the organic semiconductor.

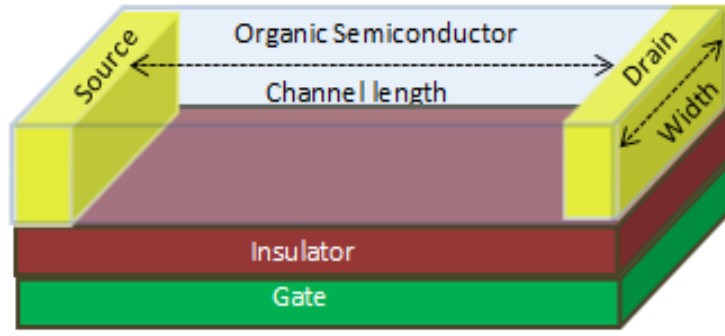


Figure 1.19: OFET device operation

Whereas the figure 1.18(b) shows device with the electrodes fabricated on the top of the organic semiconductor, which is difficult to fabricate due to a possibility of damaging semiconductor layer during the metal evaporation, so the top-contact design is not used frequently. Each device setup has their own requirements on the compatibility between the different materials used in the fabrication based on materials, solvents, developers, etc. Figure 1.19 shows the top view of an OFET and the geometrical device parameters which are channel length (represented as L) and channel width (represented as W).³⁰ Typical OFET device I-V characteristics can be classified as output characteristics, (figure 1.20) when measuring I_{ds} by varying V_{ds} with constant V_{gs} and transfer characteristics, (figure 1.21) varying V_{gs} with constant V_{ds} where C_i is the capacitance per unit area of dielectrics.

$$I_{ds,lin} = \frac{W}{L} \mu_{lin} C_i \left((V_{gs} - V_{th}) - \frac{V_{ds}}{2} \right) V_{ds} \quad V_{ds} < V_{gs} - V_{th} \quad (9)$$

The transfer characteristic curves of the transistor (i.e. a plot of the source–drain current I_{ds} against the gate voltages V_{gs}) are used to determine the charge-carrier mobility. Two regions of the characteristic curves can be differentiated. At $V_{ds} < V_{gs} - V_{th}$, the source–drain current rises linearly with increasing gate voltage

according to equation (9) (linear region), whereas at $V_{ds} \geq V_{gs} - V_{th}$, there is quadratic dependence I_{ds} from V_{gs} according to equation (10), which represents the saturation region.^{31, 32} The current on the output characteristics rises with increasing V_{ds} (linear region, equation (9)) until it reaches pinch-off point, shown in the figure 1.20 by yellow dashed line ($V_{ds}=V_{gs}-V_{th}$), after which the current levels off, i.e. saturates, with any further increase of V_{ds} (saturation region, equation (10)). The threshold voltage represents the value of the gate-source voltage beyond which a conductive channel forms at the interface (the transistor is turned on).

$$I_{ds,sat} = \frac{W}{2L} \mu_{sat} C_i (V_{gs} - V_{th})^2 \quad V_{ds} \geq (V_{gs} - V_{th}) \quad (10)$$

The charge-carrier mobility μ_{sat} in the saturation region can be calculated from the slope of the current–voltage curve in a plot of I_{ds} against $(V_{gs}-V_{th})^2$ (see Equation 10). In the transfer curves, as the magnitude of V_{gs} increases for a given V_{ds} , the source–drain current at first increases quadratically with V_{gs} (beyond a threshold voltage) and then quasi-linearly with V_{gs} , when $V_{gs}-V_{th}$ becomes larger than V_{ds} .

$$\mu_{lin} = \frac{\partial I_{ds,lin}}{\partial V_{gs}} \times \frac{L}{WC_i V_{ds}} \quad (11)$$

In this case, at $V_{gs}-V_{th} > V_{ds}$, the linear-regime field-effect mobility (μ_{lin}) can be evaluated using a standard equation 11.²⁶ In saturation region, μ_{sat} is calculated from the plot of the square root of I_{ds} , versus V_{gs} according to equation 12, assuming μ_{sat} to be independent of V_{gs} . The conventional quadratic model of FET takes into account decreasing the number of charge carriers with increasing drain source voltage at constant V_{gs} due to the drop of potential within the channel. Typically, due to higher

speed of charge carrier travel at higher electric field the magnitude of the drain-source current increases with increasing drain-source voltage until the pinch-off is reached. At this point, increasing I_{ds} due to higher charge carriers speed at higher V_{ds} is compensated by decreasing the number of charge carrier, so the current remains constant.

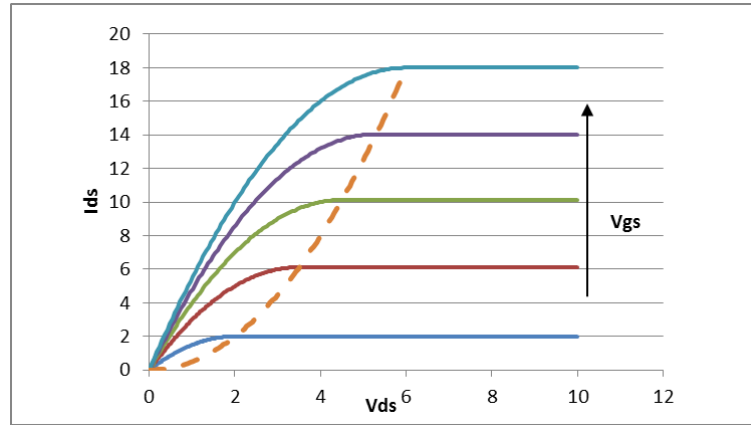


Figure 1.20: Typical output characteristics with fixed voltage of gate-source (V_{gs})

$$\sqrt{\mu_{sat}} = \frac{\partial \sqrt{I_{ds}}}{\partial V_{gs}} \times \sqrt{\frac{2L}{WC_i}} \quad (12)$$

The magnitude of the saturation current depends on the applied gate-source voltage. Even though p-type OFETs are more common than n-type OFETs, some n-type OFETs have also been researched. In the case of n-type OFETs, the current-voltage behaviour is similar, but the values will be in the first quadrant, instead of the third due to the negative charge of the carriers, i.e., electrons.

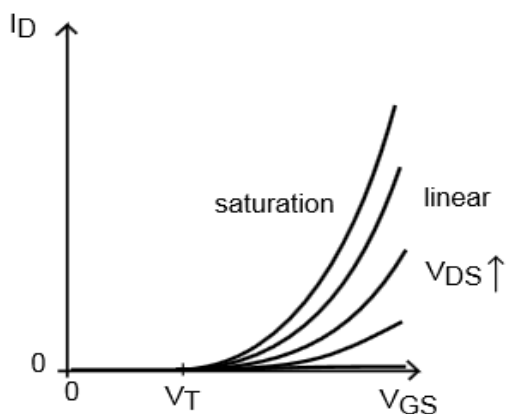


Figure 1.21: Typical transfer characteristics with fixed voltage of drain-source (V_{ds})

1.8 Organic Photovoltaics (OPV)

Photovoltaic science and technology is related to the processes of converting solar energy directly into electricity. Solar energy is expected to be one of the clean alternative energy sources to fossil fuels in the near future.^{33, 34} Organic photovoltaic systems, using organic semiconductors as the active materials (charge-transport materials), are potentially a cost-effective and lightweight solar energy conversion platform as compared to their inorganic counterparts.³⁵⁻³⁹ A typical organic solar cell consists of a thin film of organic semiconductors sandwiched between two electrodes. Commonly used architectures of OPV devices are shown in figure 1.22. There are two major architectures for single-cell-based OPVs: bilayer solar cells (in which donor and acceptor materials are sequentially stacked on top of each other as active layer) and bulk hetero-junction solar cells (BHJs, in which a blend of a donor and an acceptor material is the active layer). Bilayer solar cells are more closely analogous to conventional silicon-based solar cells.

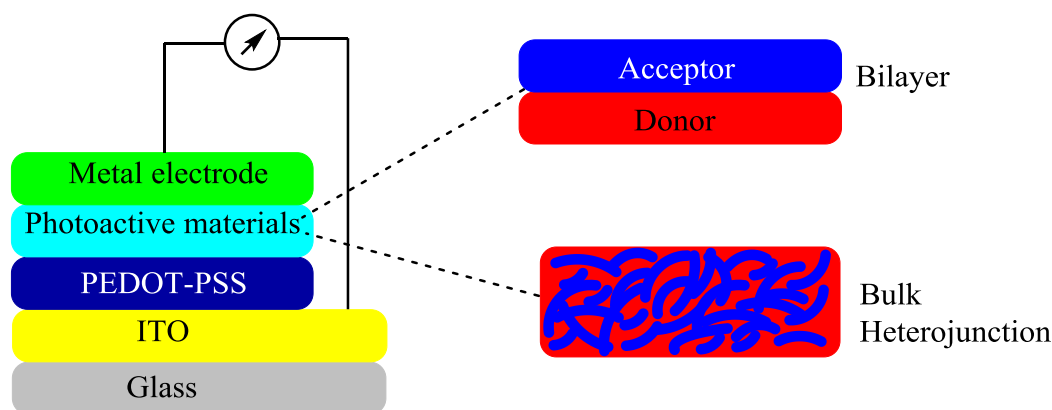


Figure 1.22: Schematic layout of a bilayer and BHJ solar cell. A part of the active layer is enlarged to illustrate the types of active materials. The schematic depicts a bilayer device architecture with the donor and acceptor material as separate layers and BHJ active layer where the donor and acceptor blend forms phase segregated domains within the active layer.

These devices benefit from the separated charge carrier transporting layers that ensure transport pathway to the correct electrode and give the separated charge carriers limited chance to recombine with their counterparts. One of the drawbacks of this device is that the limited exciton diffusion length (the lifetime of excitons is only on the order of a nanosecond) in organic semiconductors limits the energy harvesting ability of respective devices for highly efficient solar cells.⁴⁰⁻⁴² In contrast, one of the merits of BHJ solar cells is the large D/A interface area, and if the phase separation occurs on a nano scale, most of the generated excitons reach the D/A interface for charge dissociation before decay.^{37, 39, 43} However, such blends can exhibit significant morphological disorder due to random phase separation of the components. In most cases, the molecular domains of separate phase are too large (cause exciton loss) or too small (leading to facile charge recombination) in size, which lowers the overall OPV device performance.⁴⁰

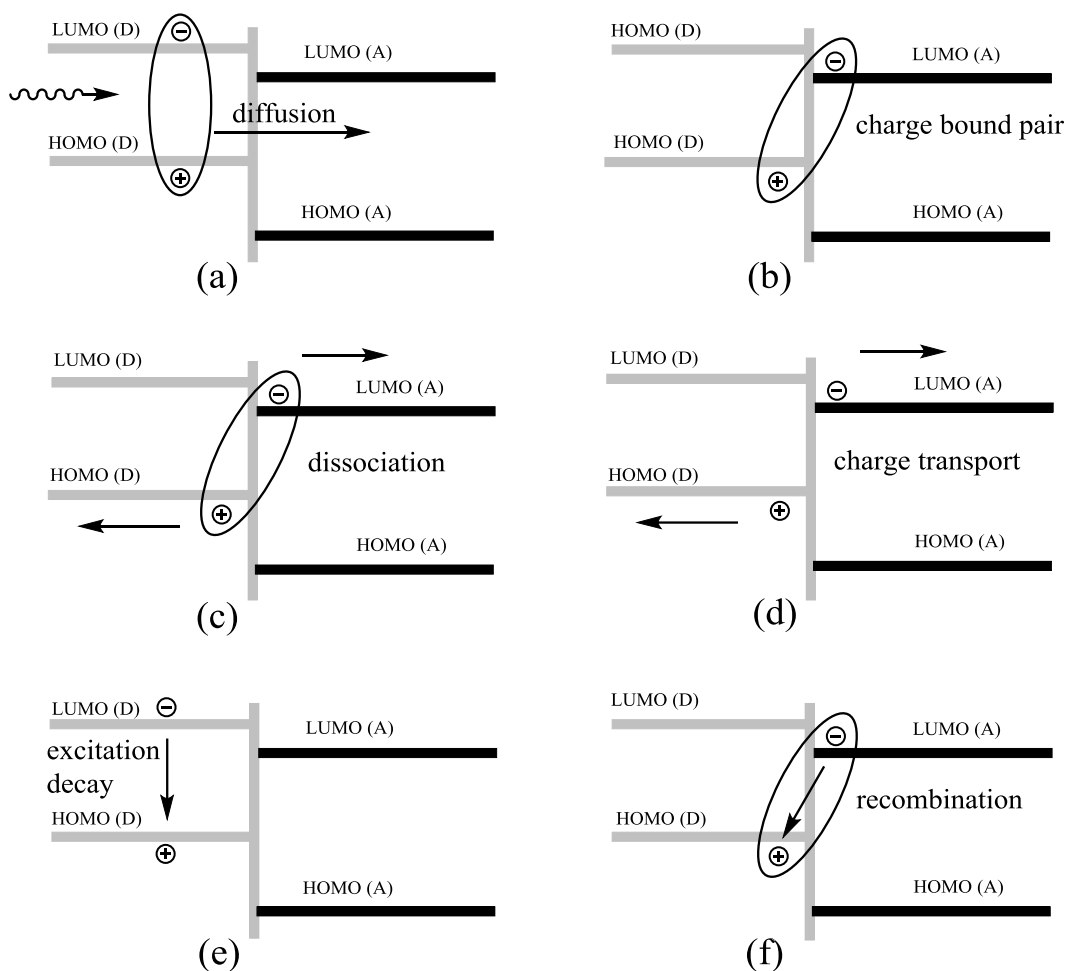


Figure 1.23: Steps and mechanism of light to electric power conversion. Light which is not converted into electricity is converted into heat and eventually contributes to losses by excitation decay and recombination processes.⁴⁴

Currently, more research efforts on OPVs are directed towards the BHJ-type solar cells, since they potentially could provide cost effective devices through wet-processing methods. It has been proposed by Frechet³⁹ that the ideal bulk-heterojunction (BHJ) solar cell should have a donor - acceptor blend with a mean domain size of the order of the exciton diffusion length (typically 10 nm). Hence, the photo-generated excitons could diffuse efficiently to the D/A interface before decay, for efficient charge separation.^{37, 39, 45} However, a number of variables, including

choice of donor and acceptor, the donor-acceptor weight ratio, the solvent and post-treatment, can dramatically affect the morphology, making device optimization challenging. In addition, based on these two main device structures, new solar cell device architectures, such as tandem solar cells^{46, 47} and inverted organic solar cells^{48, 49} have also been investigated, which benefit the overall organic solar cell research either on more efficient energy conversion or facile device fabrication process. As shown in figure 1.23, the process of converting solar energy into electricity using OPVs can be schematically described by the following several steps. To reach higher efficiency most of the photo generated excitons should diffuse and reach the dissociation region where the excitons are separated into free negative and positive polarons (electrons and holes). Excitons are neutral species, so they diffuse via random hops without any influence of the electric field.³⁶ The dissociation region is usually located at the interface between two materials with different electronic properties such as electron affinity or ionization potential.

Exciton generation can happen in any part of the semiconductor so that the layer thickness should equal the diffusion length, the distance over which the exciton moves before recombination. For organic solar cells using the donor/acceptor heterojunction for exciton dissociation, it is believed that a minimum energy difference of 0.3eV between the LUMO levels of donor and acceptor materials is required to overcome an “exciton-binding” energy for an efficient dissociation at the D/A interface.^{38, 40} There is an intermediate state between excitons and the fully separated charges. This so called charge pair is a coulombic bound pair of a negative and positive charge in different molecules as shown in figure 1.23(b). Finally, free charge transport within the donor (acceptor) phase of an active layer to the respective electrodes leads to charge-carrier

collection. Charge separation is known to occur at organic semiconductor interfaces, between materials with sufficiently different ionisation potentials (IP) and electron affinities (EA). In the latter, one material can then act as electron acceptor (A) while the other keeps the positive charge and is referred to as electron donor (D). If the difference between the LUMO levels of the donor and acceptor is not sufficient, the exciton may just hop onto the material with the lower band gap without splitting up its charges. Eventually it will recombine without contributing charges to the photocurrent. Possible loss mechanisms are exciton decay, geminate recombination of bound electron-hole pairs, and bimolecular recombination of free charge carriers [figure 1.23 (e and f)].

PCBM is now the most widely used acceptor material in organic photovoltaic applications (figure 1.24). A weak point of PC₆₁BM as a photovoltaic material is its low absorption in the visible region, due to the high degree of symmetry which makes the lowest energy transition formally dipole forbidden. To improve the absorption properties of the acceptor phase, Hummelen *et al.* synthesized the corresponding C₇₀ derivative, PC₇₁BM.⁵⁰ The absorbance of PC₇₁BM is much stronger than that of PC₆₁BM. For that reason PC₇₁BM has been widely used in organic solar cells based on small band gap polymers in order to enhance light absorption. Many organic solar cells comprising PC₇₁BM as acceptor show higher PCEs than that of the corresponding devices with PC₆₁BM as acceptor.⁵⁰⁻⁵² Besides light absorption, the electrochemical properties of the fullerene derivatives are important for the application as acceptor material in organic solar cells. The open circuit voltage is determined by the difference in energy between the LUMO level of the fullerene acceptor and the HOMO level of the polymer donor.⁵³⁻⁵⁵ For PC₆₁BM and PC₇₁BM energy levels are similar, therefore

the increase in efficiency is caused mainly by the extra light absorption by donor/acceptor (D/A) moieties.

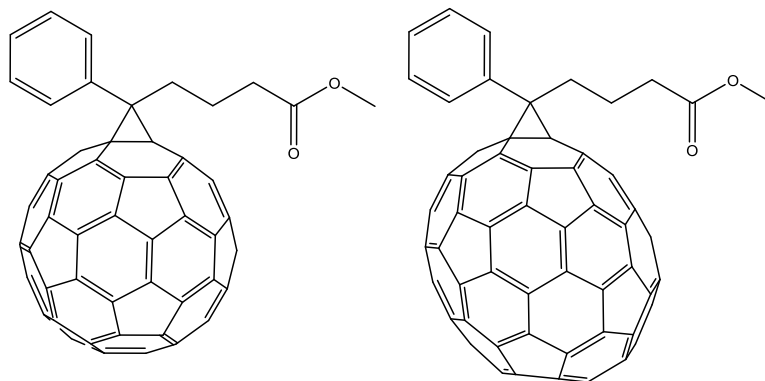


Figure 1.24: PC₆₁BM (left) and the α -type chiral isomer of PC₇₁BM (right)

Drawing the current–voltage characteristics of a cell in the dark and under illumination (Fig. 1.24) permits an evaluation of most of its photovoltaic performances as well as its electric behaviour.⁵⁶ In the dark, a typical diode-type I-V response with limited current flows in the reverse bias direction ($V < 0$) can be recorded. As the cell is illuminated, the I-V curve is ideally shifted down at all potentials because of the additional photocurrent, and power is generated in the devices. Note that the photovoltaic effect occurs only in forward bias ($V > 0$), where the cell generates power when the product of the current and the voltage is negative. V_{oc} is the voltage across the solar cell when the cell current is zero. J_{sc} is the cell current density when there is no applied bias to the cell. I_{max} and V_{max} are the values of the current density and voltage which provide the maximum power P_{max} delivered by the PV cell. Fill factor (FF) is the parameter of illuminated cell I-V curve defined as the ratio of the

maximum output power to the product of short circuit current and open circuit voltage (Equation 13).

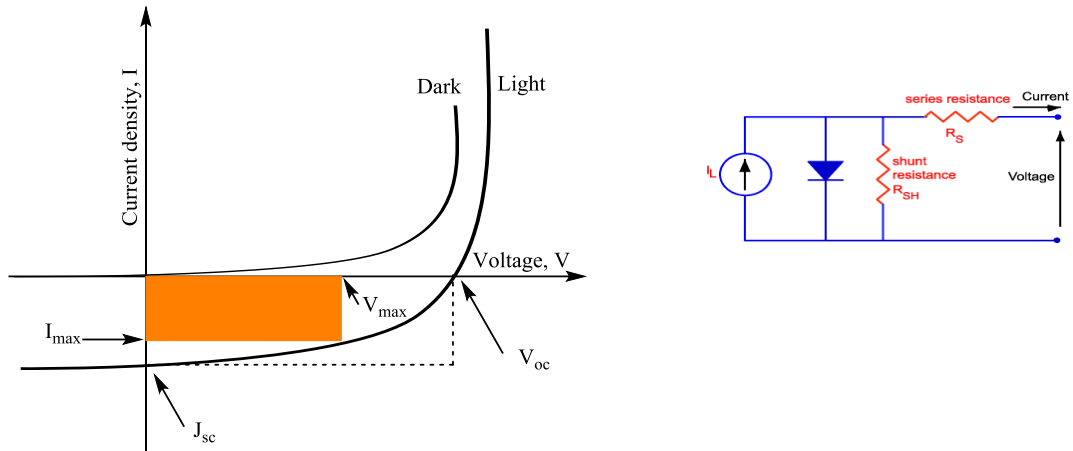


Figure 1.25: I-V characteristic of an organic solar cell under dark, and under illuminated condition (left) and equivalent circuit diagram of solar cell with shunt (R_P) and series resistance (R_S) (right).

$$FF = \frac{I_{max} \times V_{max}}{I_{sc} \times V_{oc}} = \frac{P_{max}}{I_{sc} \times V_{oc}} \quad (13)$$

$$\eta_{max} = \frac{P_{max}}{P_{in}} = \frac{I_{sc} \times V_{oc} \times FF}{P_{in}} \quad (14)$$

FF is directly affected by the values of the cells series and shunt resistance, as shown in figure 1.25. Increasing the shunt resistance (R_P) and decreasing the series resistance (R_S) could lead to larger FF and push the device output power (P_{max}) towards its theoretical maximum. According to Equation 14, power conversion efficiency (PCE), η is defined as the ratio of the maximum electric power extracted to the incident light intensity. Because of the light intensity dependence of the photovoltaic response, the efficiency should be measured under standard test conditions. The conditions normally

used are AM1.5 (air mass 1.5) corresponding to a solar irradiation with zenith angle of 48.2° which gives the pathway of the sunlight across atmosphere as long as 1.5 times of its thickness with the light intensity of 1000 W/m² and characteristic solar spectral distribution.⁵⁷

1.9 Aim of the projects

The goal of this research is 1) to design new semiconductor materials, 2) to fabricate and characterise OFET and OPV devices using some novel semiconductors with the aim to discover parameters of great importance for realizing high quality electronic devices. In organic field-effect transistors (OFETs), two types of interface are crucial determinants for device performance: 1) electrode/semiconductor interface – for charge injection; 2) semiconductor/dielectric interface for charge transport.^{58, 59} One of the few practical strategies is using a self-assembled monolayer in order to control the surface properties for favourable nanoscale ordering of OSCs.^{60, 61} Thus, self-assembled monolayer treatments on electrodes and dielectric (insulator) surfaces have been used to improve the morphology of subsequently deposited organic semiconductor. A molecular monolayer is only a few nanometres thick, however dramatically changes the electrical performance in terms of threshold voltage and mobility. SAMs can play an important role in controlling these parameters. The effect of the SAM depends on the chemical structure of the comprising molecules and on the location in the device, on the gate dielectric or on the S/D electrodes. Furthermore, the presence of a SAM layer can reduce charge trapping states at the interface by covering silanol groups and ionic impurities of SiO₂.⁶² In this thesis, the novel semiconductors OFET devices are fabricated using different solvents with the application of self-

assembled monolayers. We also discuss the effects of the molecular ordering and film morphologies of organic semiconductors on the electrical properties of OFETs.

In organic bulk heterojunction (BHJ) solar cells, high charge separation efficiency combined with the reduced fabrication costs associated with solution processing techniques offer an option for the next generation of flexible PV devices.⁶³ The control of the donor/acceptor blend morphology in BHJ materials is required for achieving high power conversion efficiency and of primary concern.⁶⁴ In this thesis, BHJ approach has been used in order to achieve higher efficiencies in organic photovoltaic devices. We will show that by using a high boiling point solvent, the power conversion efficiency of photovoltaic cells is substantially increased when compared to low boiling point solvent.^{65, 66} This method of optimization is now the most widely used processing option for polymeric and oligomeric systems. Previous examinations of the active layers from several groups have shown that the high boiling additive, added to host solvents, influence the size of the domains within the donor-acceptor blend.⁶⁷⁻⁷⁰ In this thesis, we will examine a new class of conjugated polymer and oligomer molecules with modular features that can be used to fine tune the phase separation and the optical absorption of the blend in order to achieve improved power conversion efficiency.

There is a growing interest in monodisperse conjugated oligomers for OFETs and OPVs with power conversion efficiencies greater than 3% in BHJ devices. Recently, the Skabara group has developed an H-shaped conjugated system with a tetrathiafulvalene unit as the bridging component between two oligothiophene

chains.^{65,71} It is a new hybrid electroactive compound with attractive optical and redox properties featuring the TTF unit fused directly to the conjugated oligothiophene backbone (**5T-TTF**). The incorporation of the TTF moiety in the oligothiophene architecture imparts to the materials the propensity to aggregate due to π - π stacking interactions, so they might be good candidates for organic electronic semiconductors. As a result, chapter 2 focuses on the charge-transport properties of this unusual material and some promising estimation of PCE values from BHJ solar cells.

Chapter three describes a novel donor-acceptor (D/A) conjugated co-polymer containing DPP and TTF moieties for use in OFET and OPV applications. A recent publication from PJS group reported a novel conjugated polymer **p(DPP-TTF)** with donor dithienylthieno-TTF and electron acceptor diketopyrrolopyrrole (DPP) units within the conjugated backbone and its performance in OFETs under ambient conditions.⁷² Donor and acceptor moieties were chosen in regard to their hole and electron transporting properties, respectively aiming for ambipolar characteristics. Optical, thermal, and electrochemical properties as well as nano morphology of this polymer indicated that it is a promising material for OFET and OPV applications. Expanding on this, chapter 3 emphasise on more in-depth study of FET and photovoltaic properties with their morphological studies.

Recently, Skabara's group has reported a new germanium-centred spiro compound (**5T-Ge**) with quinquithiophene arms that self-assembles in a unique fashion to give a two-dimensional packing motif.⁷³ Ge is the first of the group 14 elements to possess a full electron rich d-shell and expected to support an increased level of spiro-conjugation between oligothiophene chains. The use of a group 14 element in place of a metal centre can give access to purely covalent compounds featuring electron rich

dithiagermole rings bound via a neutral, tetrahedral sp^3 germanium centre, an area that is largely overlooked for the development of new unique and useful materials. Expanding on this, in chapter four, we have investigated by AFM measurements the surface morphology of oligomer films and its effect on the field effect mobility.⁷⁴

Chapter 5 includes an organic semiconductor, expressed as a quadrupolar linear conjugated system (**DPP Linear-c**), consisting of a 1,4-diketopyrrolo[3,4-c]pyrrole (DPP) central unit and two quaterfluorenylphenyl arms at the 3- and 6-positions of the DPP fragment. This material is studied in organic field-effect transistors (OFETs).⁶²

The 1,4-diketopyrrolo[3,4-c]pyrrole (DPP) unit is a well-known and topical building block in plastic electronics and has been incorporated into conjugated materials which have been studied as components in solar cells and FETs. The strong propensity of DPP Linear-c to 1D aggregation in the solid state favours the hole mobility of the semiconductor due to the alignment of HOMOs in the aggregates.⁷⁵ The fabrication of OFETs from this novel p-type semiconductor is reported, using different dielectrics to evaluate their effect on the overall device performance.

All the semiconductors mentioned above are p-type in which the conduction is due to the positive charge carriers. However, in order to realize applications such as organic complementary logic circuits,⁷⁶ both p-type and n-type organic semiconductors are needed with comparable electrical performance. Only a very few n-type organic materials are reported in which the conduction is due to the negative charge carriers, including fluorocarbon-substituted thiophene oligomers.⁷⁷⁻⁸¹ By adding fluorine (F) moieties to the benzene conjugated backbone, the benzene ring can be more electron-deficient and thus the electron affinity can be increased. Non-covalent interactions (F...F and F...S) have attracted more attention and been used to enforce packing

arrangements in aromatic crystals. As a result, it is expected that the electron-rich thiophene unit overlaps well with the electron-deficient perfluorophenyl rings, leading to a decrease in the intermolecular spacing. In addition, the increased electron affinity may allow good LUMO – LUMO electronic coupling between neighbouring molecules because of its improved π - π stacking ability.⁸⁰ Based on these arguments, chapter 6 describes the synthesis of the novel perfluorobenzene-thiophene based small molecule with the studies of its optical property, cyclic voltammetry, X-ray crystal determination and its suitability for n-type charge transport. Finally, Chapter 7 provides the general conclusions about all the work presented together with the description of the results obtained.

Chapter 2

Device fabrication of new hybrid organic semiconductor based on fused TTF/quinquithiophene (5T-TTF) for organic field effect transistors (OFETs) and photovoltaics (OPVs)

2.1 Abstract

There have been very few TTF fused thiophene semiconductors reported to date with mobilities above $1.4\text{cm}^2/\text{Vs}$.⁸²⁻⁸⁴ One of the promising approaches in creating high mobility organic semiconductors is the reinforcement of intramolecular interactions, which results in enhanced molecular π -orbital overlap and facile intermolecular charge transport. One such family of donor compound is based on quinquithiophene and utilizes tetrathiafulvalene (TTF) as a core unit. Due to the contribution from TTF-donor unit, the material will exhibit different morphology and hence charge transport characteristics from those reported for thiophene based oligomers.⁷¹ In this chapter, we report on the fabrication and characteristics of FET device with BG/BC geometry using 5T-TTF [4,4',6,6'-tetrakis(3'-hexyl-5'-methyl-[2,2'-bithiophen]-5-yl)-2,2'-bithieno[3,4-d][1,3]dithiolylidene] as a semiconductor to gain a better understanding of charge transport of new hybrid system. Here, we use a SAM of PFBT and ODTs at the interface between the organic semiconductor and gold contacts (gate dielectric) to alter the carrier density in the electrodes (provide better alignment of the crystalline domains in the channel). The interfaces between metal contacts and organic semiconductors in OFETs have been extensively modified to control the energy levels at the interfaces, which can change the energetic barriers for charge injection.⁸⁵⁻⁸⁷ Because of the shallow HOMO of 5T-TTF, results are analysed in detail from the perspectives of a p-type OFET device performance to understand the structure/property relationships. We also fabricated OPV devices and investigate the effect on the devices (OFET and OPV) performance of film morphology, which was varied upon using various solvents and annealing temperatures. From these studies, it

is clearly seen that the active layer structure depends heavily on the processing conditions such as interface modification, annealing temperature, solvents used etc., It is also evident that the processing induced microstructure of the active layer plays an important role in determining photovoltaic properties.⁷⁰

modified. Secondly, they may be made quite soluble in common solvents and the device fabrication can benefit from the solution processable methods. Thirdly, the planar molecular conformation with developed π -electron rich system and the high contents of sulphur atoms provide strong intermolecular interactions in the solid state induced by $\pi \cdots \pi$ stacking and S \cdots S short contacts. Fourth, the good electron donor ability with highest occupied molecular orbital (HOMO) levels close to the work function of usual metallic electrodes, (e.g. gold, silver) affording little energy barrier for charge injection from metal electrodes into their active layer.^{84, 89} Single component TTF species are increasingly being investigated as organic metals, semi- and even superconductor materials owing to their reliable redox behaviour, the high conductivity observed in their mixed valence salts, and their tendency to stack in the solid state, which maximises orbital overlap allowing for efficient charge carrier mobility. For these reasons TTFs are seen as some of the most promising candidates for p-type OFETs.⁸⁹⁻⁹²

A high-mobility OFET ($\mu=1.4\text{cm}^2/\text{Vs}$) has been reported using single crystals of the TTF derivative (Chart 2.2) as an active layer.⁸² Though, the single crystal and vacuum deposition methods⁸⁹ have been used for fabricating TTF based thin film transistors, thermal evaporation manufacture is expensive, and inadequate for attaining large area coverage thin films. To truly realize the low cost and large area coverage features of organic electronics, organic semiconductors must be deposited from solution with more economical and versatile technique like ink-jet printing.⁹³ This requirement has in turn driven the development of new solution processable TTF derivatives for OFETs.⁹⁴ TTF derivatives are mostly insoluble or less soluble in common solvents due to the strong π -interactions or the lack of flexible chains. An approach to afford

solution processable TTF derivatives is the attachment of flexible side chains or bulky groups to the π -skeleton that contains the TTF/thiophene unit. Chart 2.2 shows some of the TTF derivatives used for vacuum and solution processed thin film OFETs of mobilities up to $0.17\text{cm}^2/\text{Vs}$.

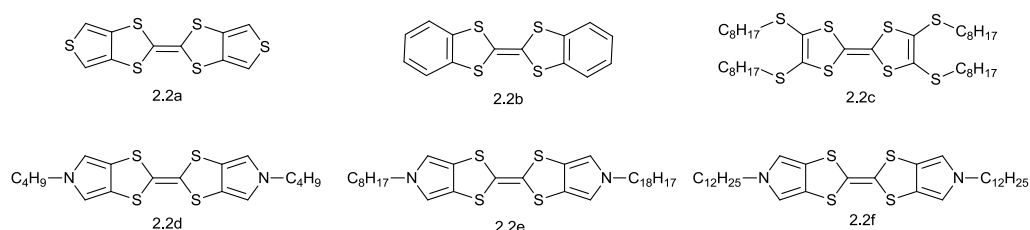


Chart 2.2 : Tetrathiafulvalene (TTF) derivatives

The fused ring systems dithiophene-tetrathiafulvalene (DT-TTF, 2.2a) and dibenzo-tetrathiafulvalene (DB-TTF, 2.2b) illustrate well the potential that TTF based systems offer. The devices based on dithiophene-TTF (2.2a) showed the best FET performance with the highest mobilities ($0.17\text{cm}^2/\text{Vs}$) that promotes the development of TTF based OFETs. Devices based on dibenzo-TTF (2.2b) showed high mobility up to $6 \times 10^{-2} \text{cm}^2/\text{Vs}$ with the on/off ratio on the order of 10^4 due to its π -expanded structure that benefits the intermolecular $\pi \cdots \pi$ interactions. The crystal packing of 2.2a and 2.2b is similar to that of pentacene, giving a herringbone pattern, with the short interplanar distance (3.56 \AA) and intermolecular $\text{S} \cdots \text{S}$ interactions (3.6 \AA).⁸⁴ The charge carrier mobilities observed in commercial field effect transistors based on amorphous silicon are in the range of $0.1\text{-}1\text{cm}^2/\text{Vs}$.⁹¹ In order to compete with these inorganic thin film transistors (TFT), OFETs should be able to at least match these values. Ukai et al. investigated the transport property of OFETs based on tetrakis(alkylthio)tetrathiafulvalene (TTC_n-TTF) derivatives with $n = 8$. TTC_n-TTF

(2.2c) was drop cast on the prefabricated substrates with BC device geometry from its saturated chloroform solution. The field effect hole mobility of 10^{-6} - 10^{-5} cm²/Vs was obtained for that compound. The mobility increased with the longer alkyl chains, which was attributed to the reduction of intermolecular distance between adjacent TTF units caused by the fastener effect of long alkyl chains. Besides the low mobility, the devices based on bottom contact showed other poor FET characteristics, such as the large off current at zero V_g , the small on/off ratio (<2), and the non-saturating behaviour.⁹⁵ Compound 2.2c has high HOMO levels, their thin films are unstable to oxygen, and the resulting oxidation dopants increase the conductivity of the film in the off (or ungated) state and lead to aforementioned poor FET performance. Table 2.1 represents fabrication methods and mobility parameters based on TTF derivatives. Recently, a series of N-alkyl substituted bis(pyrrolo[3,4-d])tetrathiafulvalenes (PyTTFs, alkyl=n-butyl, n-octyl) were synthesized by Takimiya and co-workers as soluble TTF derivatives for solution processable TTF based OFETs. The spin coated thin films of 2.2d and 2.2e showed inferior FET characteristics with mobility of 10^{-5} cm²/Vs or no reproducible field effect. Specifically, most of the 2.2e devices showed no current modulation on the application of gate bias and thus the FET parameters of the devices were not determined. On the contrary, OFET devices consisting of spin coated thin films of 2.2f exhibited higher FET performance with mobility about 10^{-2} cm²/Vs and on/off ratio up to 10^4 . Studies on single crystal analysis of 2.2d, 2.2e and 2.2f revealed the reason for their different FET performance. The XRD studies of compound 2f showed two dimensional solid state structure with columnar π -stacking and intercolumnar S \cdots S interactions, whereas no intermolecular π -stacking feature was observed for the cases of compounds 2.2d and 2.2e, there were only intermolecular

side-by-side S...S interactions. The length of the alkyl chains not only affected the solubility of PyTTFs but also influenced their solid state structures and thereby led to the different performance in OFET.⁹⁶

| | Fabrication method | Device geometry | Mobility (cm ² /Vs) | HOMO level (eV) | on/off ratio |
|------|--------------------|-----------------|--------------------------------|-----------------|--------------------|
| 2.2a | zone casting | TC | 0.17 | -5.1 | 10 ⁶ |
| 2.2b | vacuum deposition | BC | 6x10 ⁻² | -4.9 | 10 ⁴ |
| 2.2c | drop casting | BC | 3.4x10 ⁻⁶ | --- | <2 |
| 2.2d | Spin coating | TC | 1.7x10 ⁻⁵ | -4.6 | 10 |
| 2.2e | Spin coating | TC | --- | -4.6 | --- |
| 2.2f | Spin coating | TC | 6.8x10 ⁻² | -4.6 | 2x10 ⁻² |

Table 2.1: FET characteristics of vacuum and solution processed thin-film devices based on TTF derivatives

2.3 OFET fabrication of Oligothiophenes

Though oligothiophenes have been first synthesised and isolated in 1947, (chart 2.3 a,b) their electrical properties have been studied very recently.⁹⁷ A practical strategy for investigating the relationship between molecular structure and electrical performance is the systematic variation of the number of repeat units in a particular type of molecular semiconductor or varying the length of alkyl substituents. Oligothiophenes are most suitable compounds for these types of investigations, due to their straightforward synthesis and because of a wide range of possible modifications of their chemical structure. Due to the poor solubility of the oligomers longer than five thiophene units (quinquthiophene), most electrical measurements on oligothiophenes are carried out on vacuum evaporated thin films on substrates already equipped with a conducting electrode, generally gold. Organic TFT's based on oligothiophenes were

first reported by Horowitz and Garnier⁹⁸⁻¹⁰⁰ and later by Dodabalapur,¹⁰¹ Katz^{101, 102} and others.

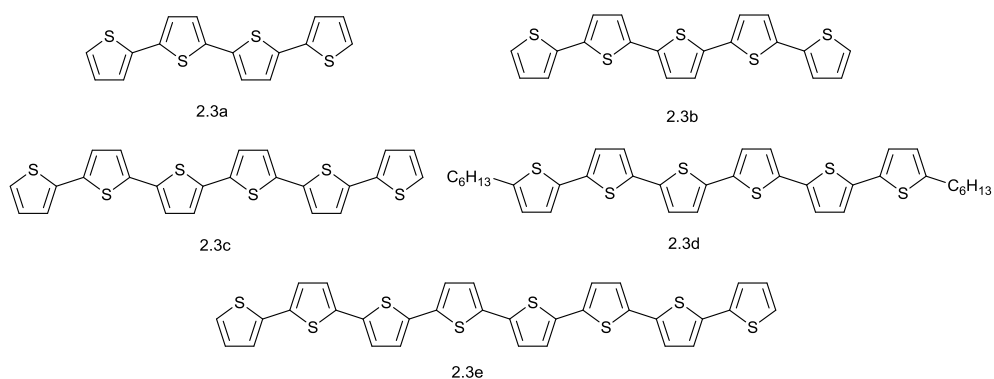


Chart 2.3: Unsubstituted and substituted oligothiophenes

The first FET based on an oligothiophene (sexithiophene, 2.3c) was reported in 1989 by Horowitz and co-workers, with a mobility of $10^{-4}\text{cm}^2/\text{Vs}$.¹⁰³ Since then, the performance of oligothiophene FETs has gradually improved, due to progress in the purity of the materials and the deposition techniques such as vacuum or spin coating. A first breakthrough occurred with the synthesis of oligothiophenes substituted by alkyl groups at the terminal position.^{104, 105} Importantly, the field-effect mobility of the substituted oligomer is ten to one hundred times higher than their non-substituted homologue. Surprisingly, Horowitz et al. noted that the mobility of the octamer (2.3e) is lower than that of the hexamer (2.3c). This was first assigned to the difficulty in purification due to its solubility. However, it later appeared that the mobility of the unsubstituted sexithiophene (2.3c) could reach values close to that of the terminal substituted sexithiophene (2.3d) compound by evaporating the material using low evaporation rates.^{106 101} Under such circumstances the molecules tend to orient parallel

to the film, an arrangement that is naturally occurring with the substituted oligomer. Moreover, recent measurements on shorter oligothiophenes (quaterthiophene (2.3a) and quinquithiophene (2.3b)) gave mobility very similar to that of the sexithiophene (2.3c) and octithiophene (2.3e).^{102, 107} Significant results are gathered in Table 2.2. Recent measurements on sexithiophene single crystals gave a mobility of $0.075\text{cm}^2/\text{Vs}$.¹⁰⁸ Even though this mobility is significantly higher than that reported for crystalline films, it does not indicate a real improvement of charge transport for large area applications.

| Non substituted | | Alkyl substituted at the terminal position | |
|------------------|----------------------------------|--|----------------------------------|
| Compound | Mobility cm^2/Vs | Compound | Mobility cm^2/Vs |
| Quaterthiophene | 2×10^{-7} | Quaterthiophene | 2×10^{-5} |
| Quinquithiophene | 3×10^{-5} | Quinquithiophene | 9×10^{-4} |
| Sexithiophene | 5×10^{-4} | Sexithiophene | 5×10^{-2} |
| Octithiophene | 2×10^{-4} | Octithiophene | |

Table 2.2: Organic Field Effect Transistor mobility of oligothiophenes

Halik et al. synthesized and demonstrated organic thin film transistors TFTs based on a series of alkyl end substituted oligothiophenes, employing top contact and bottom contact device structures, with ultrathin self-assembled monolayer (SAM) gate dielectrics. They found that the length of the oligomer (quater, quinquithiophene or sexithiophene units, chart 2.4) has no significant effect on the carrier mobility, whereas the length of α, α' -alkyl substituted oligothiophenes has a notable influence on the thin film transistor performance. The presence of long decyl side chains is likely to create a dense intrinsic barrier separating the conjugated thiophene backbones from source and gate terminals which lead to a significant contact resistance. When the length of

the molecules, hence increasing the two dimensional character of the material.¹⁰⁴ Furthermore, the alkyl chain at each end of the substituted molecule tends to decrease the conductivity in the direction perpendicular to the film, which is also the direction parallel to the chain of the molecules.

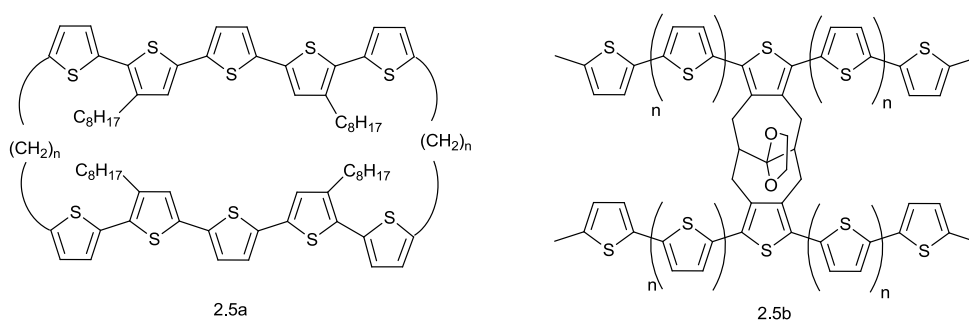


Chart 2.5: Linear conjugated oligothiophenes as π -dimeric model

In contrast to the case for linear systems, Otsu Bo et al. prepared a first example of cyclophane-type π -dimeric model compounds (Chart 2.5a) containing two quinquithiophene in which two ends of the oligothiophene units were linked to alkyl bridge groups.¹¹⁰ Various studies proposed the formation of π -dimers as charge carriers. However, the formation of these π -dimers has been explored only by analysing low temperature electronic spectra of oligothiophenes in various oxidation states.¹¹¹ Collard et al. synthesized cofacially stacked π -dimeric model oligothiophenes (2.5b), in which two oligothiophene units, fused to a bicyclo[4,4,1]undecane core, showed strong interchain interactions and stabilization of the radical cations.¹¹² Incorporation of fused 4,5,6,10,11,12-hexahydro-5,11-methanocyclodeca[1,2-c:6,7-c']dithiophene system into oligothiophene architecture provides control over the orientation of the two oligothiophenes stacked on top of each other to allow charge carriers to hop through from one oligomer to another. One and

two electron oxidation of these stacked oligomers afforded radical cations and dications that served as models for polarons and bipolarons in p-doped conjugated polymers and demonstrated the effect of π -stacking on the electronic structure of these species. The reliable synthesis of such molecules (Chart 2.5) has become possible only recently and their implementation in different areas of organic electronics has yet to be explored.

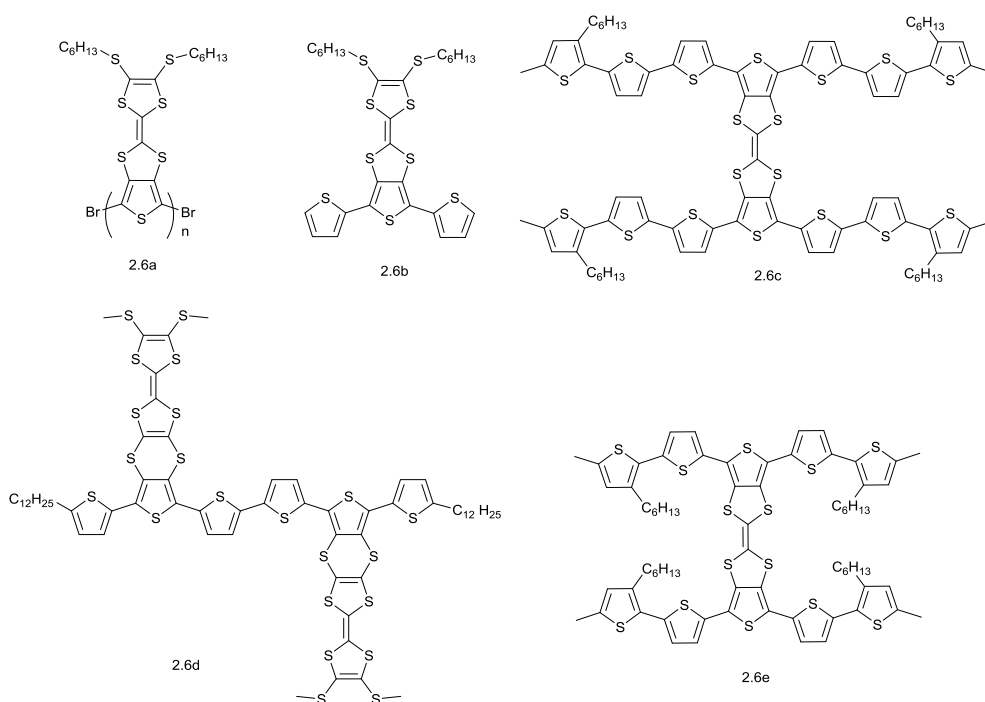


Chart 2.6: Fused TTF poly (thiophene)s and oligothiophenes previously developed in the Skabara group.

TTF derivatives have been studied as components in OFETs and there are several examples of materials with high mobilities,^{89, 91} including fused TTF/thiophene hybrids such as DT-TTF as shown above in chart 2.2a. Over the past decade, the Skabara group has developed a variety of new hybrid electroactive compounds based on poly- and oligo(thiophenes) featuring the TTF unit fused either directly to the conjugated poly- or oligo(thiophene) backbone, or via a non-planar dithiine ring (chart

2.6).¹¹³⁻¹¹⁶ It was found that, depending on the structure of the compounds the TTF units can either dominate the electroactivity of the compound or participate in a truly hybrid red-ox state. The incorporation of the TTF moiety in the oligo- and poly (thiophene) architecture imparts to the materials the propensity to aggregate due to π - π stacking interactions, so compounds with TTF units might be good candidates for organic electronic semiconductors. We have studied electronic and charge transport properties of one such a material on a basis of an unusual hybrid structure (chart 2.6e): methyl end capped bis(quinquithiophene) bridged by a fused tetrathiafulvalene (5T-TTF). The chains also bear hexyl groups on the 3-position of the terminal thiophene rings to improve solubility. The electrochemical band gap (HOMO-LUMO gap) of this material obtained was 2.14eV. The HOMO and LUMO levels were observed at -5.06 and -2.92eV respectively.⁶⁵

2.4 5T-TTF OFET results

OFETs were fabricated with various SAM reagents for gold contact and SiO₂ surfaces treatments to evaluate their effect on overall device performance of the 5T-TTF derivative (chart 2.6e). The representative output and transfer electrical characteristics of bottom gate, bottom contact devices A, B, C and D with the same channel length and width ($L = 10 \mu\text{m}$, $W = 1\text{cm}$) and different surface treatments are compared. The use of SAM reagents has proved to be an effective approach to optimize thin film growth and align the energy levels, that influence the device performance.¹¹⁷ Field effect mobilities and threshold voltages (V_{th}) were calculated in the saturation regime defined by standard FET models by fitting the square root of drain-source current ($\sqrt{I_{\text{ds}}}$) versus gate source voltage (V_{gs}) at $V_{\text{ds}} = -50\text{V}$ for all devices. Also extracted

from transfer characteristics are the threshold voltage (V_{th}) and the on/off current ratio (I_{on}/I_{off}). All the data (μ , V_{th} and I_{on}/I_{off}) are summarized in Table 2.3. Device fabrication started with commercially available silicon substrates, containing thermally grown 200 ± 10 nm thick silicon dioxide layer and pre-patterned source and drain (Au) electrodes, which were subsequently treated with UV ozone for 1 minute.

| Devices | Dielectric (nm)/Au/SiO ₂ modifying agent | Solvents used | V _{gs} interval range, V | μ , cm ² /Vs | I _{on} /I _{off} at V _{ds} of -50V | V _{th} , V |
|---------|---|---------------|-----------------------------------|-----------------------------|--|---------------------|
| A | 200/----- | CF | 20-55 | 1.94×10^{-3} | 10^5 | -7.56 |
| B | 200/PFBT | CF | 20-55 | 1.20×10^{-3} | 10^4 | -5.99 |
| C | 200/PFBT | CB | 20-55 | 1.89×10^{-4} | 10^4 | - |
| D | 200/PFBT/ODTS | CF | 20-55 | 9.56×10^{-3} | 10^5 | -15.4 |

Table 2.3: Device configurations produced with various SAM reagents and solvents

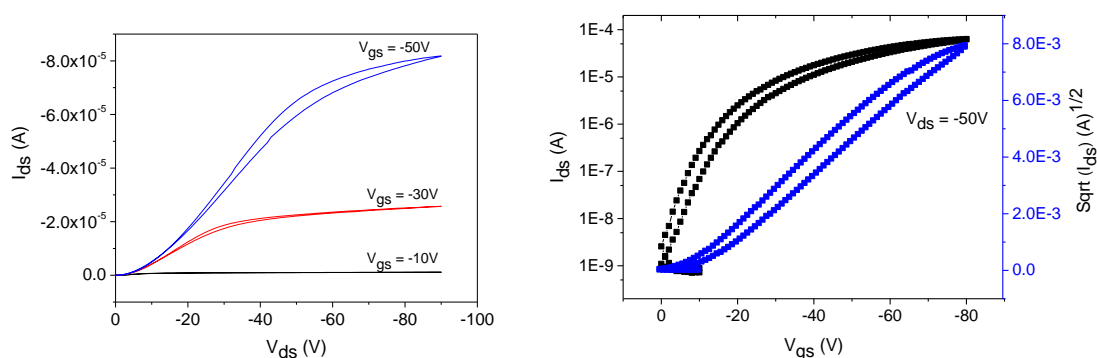


Figure 2.1 : Output characteristics (2.1a, left) and transfer characteristics (2.1b, right) of OFET fabricated by spin-coating 5T-TTF from chloroform on Si/SiO₂ substrates with untreated gold electrode

In the case of device A, the fabrication was completed without any surface treatments. An active semiconductor material (5T-TTF) is deposited by spin coating from solution (10mg/ml) at 800 rpm and then annealed at 120°C for 20 minutes. The output characteristics plotted in figure 2.1a shows the drain current (I_{ds}) as a function of source drain voltage (V_{ds}) for different values of gate voltage, (V_{gs}). A small hysteresis and a

non-linear injection (-50V), but a good saturation can be seen from the output characteristics.

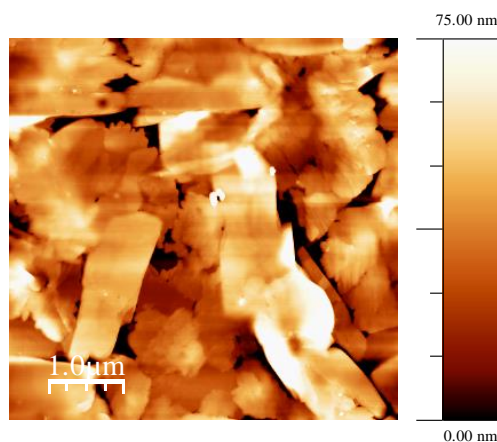


Figure 2.2: AFM image of 5T-TTF film cast from chloroform solution on Si/SiO₂ substrate

Traps may be present at the bulk material or at metal/semiconductor interfaces which results in hysteresis effects in electrical characteristics of the devices.¹¹⁸ The transfer characteristics, figure 2.1b, measured at $V_{ds} = -50V$ also show some hysteresis. The mobility of this device shows the value of $1.94 \times 10^{-3} \text{cm}^2/\text{Vs}$, with the on/off ratio of 10^5 , which are reasonable for an oligomer transistor. Figure 2.2 shows $5\mu\text{m} \times 5\mu\text{m}$ micrograph of the semiconductor film with rms roughness of 51nm obtained from tapping mode atomic force microscope (AFM) images. The combined effect of high solvation energy and a fast evaporation of solvated state CF upon annealing leads to a relative increase in the rate of crystal growth in comparison to that of nucleation and produces large crystalline domains.⁶⁵ Taking into account that the mobility calculated for transistors fabricated by spin-casting from CF is higher than those from CB one may assume that the relative stability of solvated states in the former produce upon annealing not only a larger size of crystalline domains but a smoother grain boundary as well. Also, the work function of the bare Au surface was previously found to be

around -4.9eV ¹¹⁷ from photoelectron spectroscopy (PES). Since 5T-TTF material has HOMO level of -5.06 eV , there may be an energy level mismatch between metal contacts (Au) and semiconductor (5T-TTF) which causes contact resistance. While for PFBT treated Au, the work function increases to 5.45eV and should match the energy levels at metal/semiconductor interface.¹¹⁷

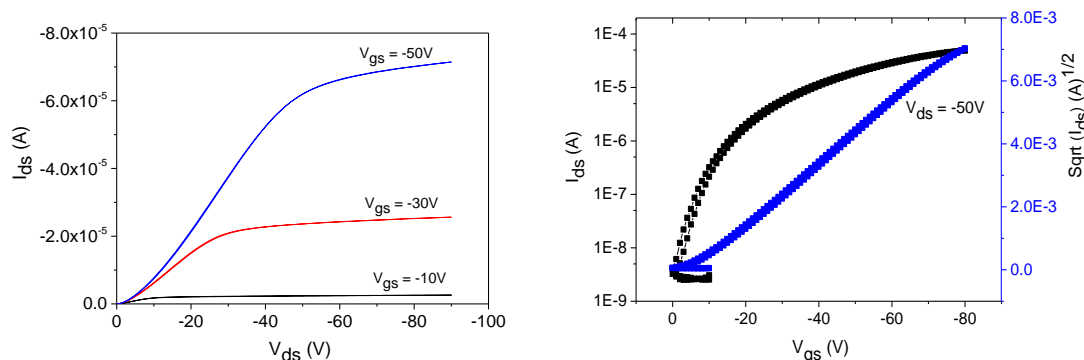


Figure 2.3: Output characteristics (2.3a, left) and transfer characteristics (2.3b, right) of OFET fabricated by spin coating 5T-TTF from its chloroform solution on Si/SiO₂ substrates with PFBT treated gold electrode

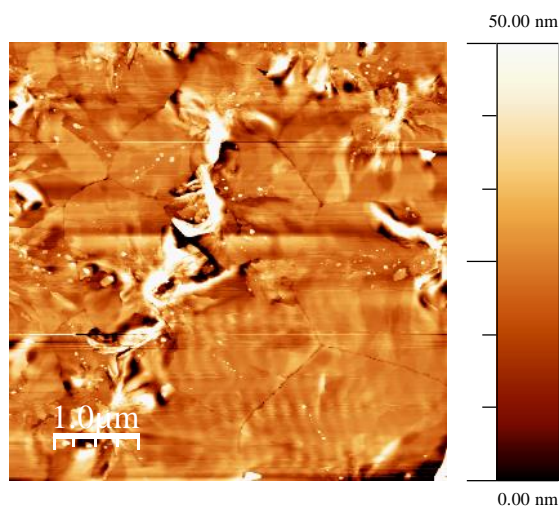


Figure 2.4: AFM image of 5T-TTF thin film spin cast from chloroform solution on Si/SiO₂ substrate with PFBT treated Au electrode.

In order to reduce the contact resistance between the source/drain metal (gold) and the 5T-TTF organic semiconductor, gold electrodes were treated with a dilute PFBT solution for 20 minutes. The entire substrate was immersed in a solution containing PFBT in 2-propanol (7mM) since thiols selectively bond to Au surfaces to form a self-assembled monolayer (SAM) and then rinsed with pure isopropyl alcohol to remove the residual PFBT. In this manner, we can selectively alter the surface energy of the Au contacts, while the surface energy of SiO₂ remains unchanged. Due to aforementioned alignment of energy levels on the metal-semiconductor interface, the transistors prepared using PFBT Au-treated substrates show improved output and transfer characteristics with less hysteresis. From the transfer characteristics, (figure 2.3b) the on/off current ratio of 10⁴ was measured at V_{ds}= -50V.

The field effect mobility of 1.20x10⁻³cm²/Vs and threshold voltage of 5.99V were estimated for device 'B'. In this case, lower mobility is observed but more reproducible if compared with device 'A'. Since the PFBT layer alters only the Au electrodes, we have not found any prominent difference in morphology between devices 'A' (fig. 2.2) and 'B' (fig. 2.4). In order to investigate the solvent effect on the morphology of spin cast films and OFET performance we used a solution of 5T-TTF in CB to fabricate device 'C' using thiol treated substrates. There was a significant change in morphology and hole mobility observed in the semiconductor film when CB was used as a solvent. The solution of 5T-TTF in chlorobenzene (10mg/ml) was spun over the pre-patterned source/drain electrodes at 800 rpm and annealed at 120°C for 20 minutes.

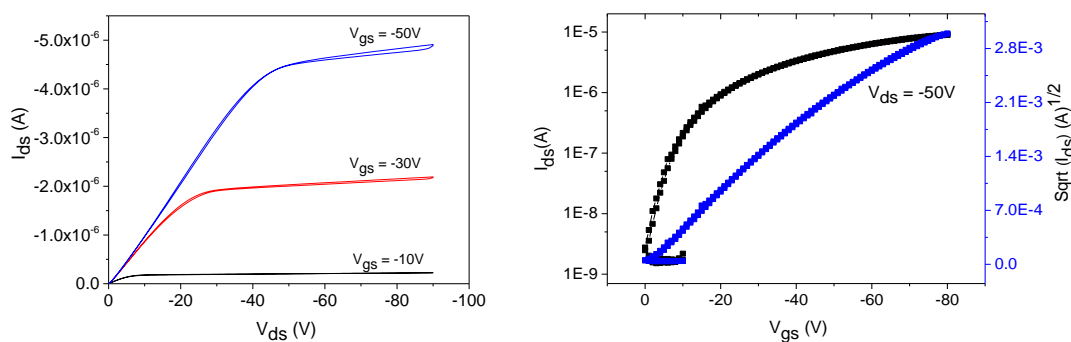


Figure 2.5: Output characteristics (2.5a, left) and transfer characteristics (2.5b, right) of OFET fabricated by spin-coating 5T-TTF from chlorobenzene on Si/SiO₂ substrates with PFBT treated gold electrode

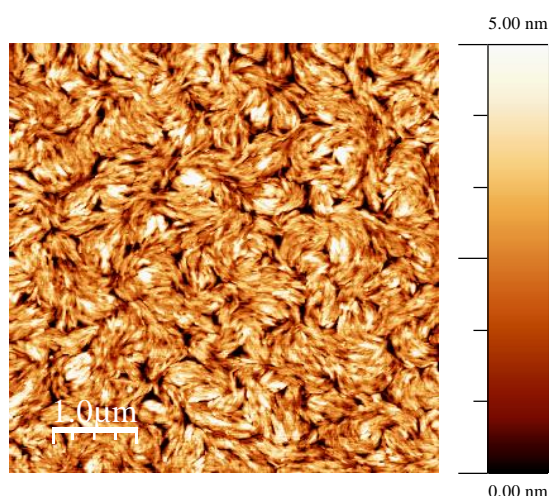


Figure 2.6: AFM image of 5T-TTF film cast from chlorobenzene solution on Si/SiO₂ substrate

The output and transfer characteristics of the resulting OFET are shown in figure 2.5. In each case, the forward and reverse voltage scans are shown. The output characteristics (figure 2.5a) present a very small amount of hysteresis, with the transfer characteristic showing no hysteresis at all. The device exhibits an extracted field effect mobility of $1.89 \times 10^{-4} \text{cm}^2/\text{Vs}$ with an on/off current ratio of 10^4 . Figure 2.6 shows $5 \mu\text{m} \times 5 \mu\text{m}$ micrographs of the 5T-TTF thin film with rms roughness of 1.1nm obtained by AFM. The morphology obtained from chlorobenzene is clearly different from those of

chloroform (figure 2.4). After annealing at 120°C, the height image shows a remarkable tight packing morphology, which is provided by strong propensity of quinquithiophene-TTF to aggregate in this solvent.⁶⁵ Upon spin-coating in chlorobenzene and annealing treatment, the rate of nucleation dominates over the rate of crystal growth which produces small crystalline domains with ordered structures formed by self-assembly of quinquithiophene through the strong π - π intermolecular interaction of its conjugated backbone.⁶⁵

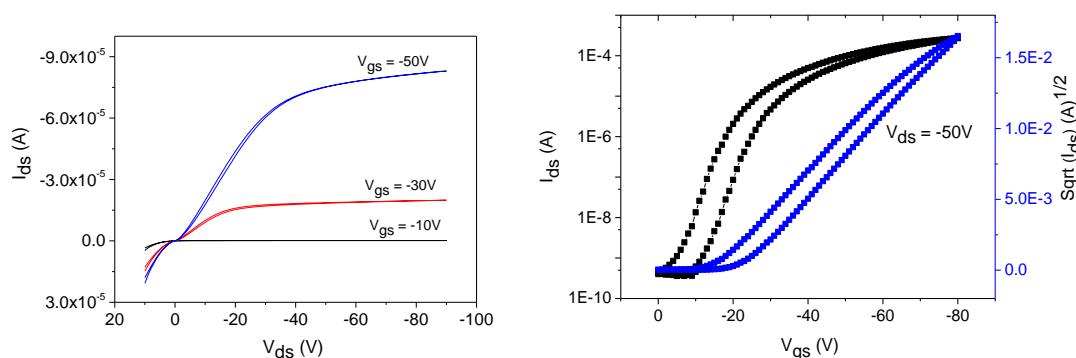


Figure 2.7: Output characteristics (2.7a, left) and transfer characteristics (2.7b, right) of OFET fabricated by spin-coating 5T-TTF from chloroform on ODTS treated Si/SiO₂ substrates with PFBT treated gold electrode

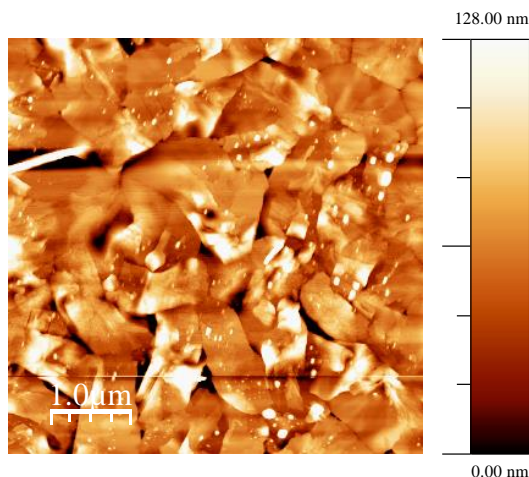


Figure 2.8: AFM image of 5T-TTF film spin-coated from chloroform solution on ODTS treated Si/SiO₂ substrate.

More optimizations are necessary to yield an oriented crystalline domain using a SAM layer, and this is investigated in the case of device 'D' by exploring an another processing method for fabricating organic electronic devices. In the case of device 'D' after PFBT treatment of the Au electrode, the substrate was then exposed to dilute ODTS solution in toluene. Both PFBT and ODTS treatment were performed under an ambient atmosphere. Good device characteristics are retained and shown in figure 2.7. However, the transfer characteristics (2.7b) show non-negligible, slight hysteresis. Due to the combined effects of ODTS and PFBT surface treatments, samples annealed under optimized conditions possess a hole mobility of $9.56 \times 10^{-3} \text{cm}^2/\text{Vs}$ with the on-off ratio ($I_{\text{on}}/I_{\text{off}}$) 10^5 . AFM image (fig. 2.8) shows relatively large domain size with roughness value of 24nm. The hydrophobic interactions between the ODTS treated substrate surface and alkyl chain of the semiconductor proved more favourable for field effect charge transport orientation of the crystalline domain in the channel.^{58, 65.}
¹¹⁹ The orientation of π - π stacking directions along the plane of the substrate provided by ODTS for large crystalline domains of the film obtained from the chloroform led to the maximum OFET performance for quinquithiophene-TTF.²³

In Table 2.3 the device configurations and mobilities calculated in the saturation regime are listed. Interestingly, device 'D' has reached the highest mobility among all the cases A, B, C, and D. The best values of mobility achieved for this material are attributed to several factors such as the quality of contacts and grain boundaries, trap or defect densities, molecular packing structures. The mobility and AFM data show that the microstructure in the channel area is one of the critical factors in determining OTFT performance. The improved mobility of device 'D' is likely provided by smooth

grain boundary between larger crystalline domain⁶⁵ and their orientation favourable²³ for charge transport due to hydrophobic interactions between ODTs SAM and alkyl chain of 5T-TTF.^{58, 65} The comparison of mobility we observed for compound 5T-TTF with that for end-capped quinquithiophene (9×10^{-4})¹²⁰ allow us to assume that the charge trapping due to formation of stable TTF centred cation-radicals is not significant for 5T-TTF.

2.5 OPV fabrication using oligothiophenes materials

A major breakthrough towards efficient organic solar cells was realised by Yu et al., with the development of the bulk heterojunction concept.¹²¹ These organic solar cells contain a photoactive layer blending conjugated donor polymers or oligomers with fullerene derivatives or n-type acceptor materials.^{122, 123} Among the wide selection of donor systems suitable for displaying photo induced charge transfer processes, TTF derived donors play an important role mainly in organic semiconductors research.^{122, 124} Strong donor properties of TTF are due to the gain of aromaticity as a result of the formation of the thermodynamically stable heteroaromatic cation upon oxidation of the TTF molecule.¹²⁵

Suzuki et al., reported the fabrication and characterization of a C₆₀/tetrathiafulvalene solar cell.¹²⁶ C₆₀ and TTF (Chart 2.1a) (10 mg, weight ratio of 1/1) dissolved in *o*-dichlorobenzene (1 mL) was spin-coated on PEDOT: PSS film pre-deposited on ITO glass substrate. The thickness of the bulk heterojunction films were approximately 150 nm. Aluminium (Al) metal at thickness of 100 nm was evaporated on a top of the organic layer. The bulk heterojunction was treated by the annealing process, V_{oc} , J_{sc} , fill factor (FF), and power conversion efficiency (PCE) were obtained at 0.002V,

$3.5 \times 10^{-5} \text{ mA/cm}^2$, 0.24 and $1.9 \times 10^{-8} \%$, respectively. Recently,¹²⁷ a bulk heterojunction organic solar cell has been fabricated and characterized using as an active layer the blend of C_{60} and DBTTF (Dibenzo-TTF, chart 2.2b). The active layer in the donor-acceptor weight ratio of 1:1 has been dissolved in o-dichlorobenzene (1 mL) and spin-coated on PEDOT: PSS film pre-deposited on ITO glass substrate, the thickness of the active film being maintained around 200 nm. The photovoltaic properties of the bulk heterojunction solar cell were optimized in which the measured parameters of V_{oc} , J_{sc} , FF and PCE were obtained to be $3.6 \times 10^{-4} \text{ V}$, $8.0 \times 10^{-2} \text{ mA/cm}^2$, and $7.2 \times 10^{-6} \%$ respectively. The bulk heterojunction solar cell had low power conversion efficiency due to the charge recombination near BHJ interface. The heat treatment was carried out at 100°C for 30 min in N_2 atmosphere. The heat treatment was assumed to recover microstructure near the inner interface between DBTTF and C_{60} , yielding a slight improvement of the photovoltaic performance.

The first demonstration of linear oligomer donors for heterojunction photovoltaic cell was reported in 1995 with a PV device fabricated with quinquithiophene (5T) (chart 2.3b) and thiophene octamer (8T) (chart 2.3e) as donors and a perylene pigment as an acceptor. In the case of using octamer (8T) as a donor with perylene dye the heterojunction cell exhibited a fill factor (FF) of 0.5 and a PCE of 0.6% under irradiation of white light. The application of α -8T would allow vacuum deposition techniques to be used in the production of the cells.¹²⁸ From the same group, a heterojunction photovoltaic cell with quinquithiophene (5T) as a donor and a perylene pigment as an acceptor exhibited a conversion efficiency of 0.02% with a fill factor of 0.29. An open circuit voltage of 0.7V and a short-circuit photocurrent of $7 \times 10^{-2} \text{ mA/cm}^2$ were obtained for an irradiated white light at 62 mW/cm^2 .

The one order of magnitude higher conversion efficiency of 8T over 5T may be attributed to series of aspects such as higher charge carrier mobility as determined from the performance characteristics of field-effect transistors, longer wavelength absorption, a lower oxidation potential, and probably a better quality of the film for 8T.¹²⁹ Sakai et al., investigated the device structures and device fabrication procedures of sexithiophene (chart 2.3c) (6T):C₆₀ bulk heterojunction PV cells which showed the PCE of 1.5% with V_{oc} of 0.68V, FF of 0.39 and J_{sc} of 5.6mA/cm². The PCE of the 6T:C₆₀ (1:5) device is three times higher than that of the 6T:C₆₀ (1:1) device which is only 0.52%. As for the relationship between the blend morphology and the photovoltaic characteristics, it is clear in the case of blend ratio 1:1 that charge separation does not occur efficiently because there are many grains and a required carrier transport interpenetrating network does not exist, which explains why charge carrier transport is poor. Consequently, J_{sc} is low. On the other hand, in the case of blend ratio 1:5, excess C₆₀ in the blend leads to the formation of homogeneous film and the desired interpenetrating network, which results in higher J_{sc}.

| | Device Geometry | D/A ratio | V _{oc} , V | J _{sc} , mA/cm ² | FF | PCE, % |
|------|------------------------|-----------|----------------------|--------------------------------------|------|----------------------|
| 2.1a | Solution Process | 1:1 | 0.002 | 3.5x10 ⁻⁵ | 0.24 | 1.9x10 ⁻⁸ |
| 2.2b | Solution Process | 1:1 | 3.6x10 ⁻⁴ | 8x10 ⁻² | 0.25 | 7.2x10 ⁻⁶ |
| 2.3b | Vapour deposition | --- | 0.70 | 7x10 ⁻² | 0.29 | 0.02 |
| 2.3c | Vapour deposition(p-n) | 1:5 | 0.68 | 5.6 | 0.39 | 1.5 |
| 2.3e | Vapour deposition | --- | 0.42 | 2.9 | 0.5 | 0.59 |

Table 2.4: Photovoltaic parameters of TTF based organic semiconductors prepared by solution and vacuum evaporation techniques

As for increasing V_{oc}, it may be presumed that V_{oc} approaches the maximum value as the blend morphology approaches the ideal structure, along with improved interface

conditions.¹³⁰ Table 2.4 collects the photovoltaic parameters of some examples of TTF based organic semiconductors.

2.6 5T-TTF OPV results

Very recently, a series of fused TTF and thiophene based donor materials (chart 2.6) has been synthesised by the Skabara group, aimed towards OSCs due to their strong tendency towards aggregation through π - π interactions. Among those materials, 5T-TTF (chart 2.6e) has demonstrated higher OFET mobility ($9.56 \times 10^{-2} \text{cm}^2/\text{Vs}$) and might be a good choice for fabrication of photovoltaic cells. For active layer (BHJ) formation, the optimum 5T-TTF: PC₇₁BM weight ratio is found to be 1:4, and the two best suited solvents for this blend are CF and o-DCB. Active materials were cast on the PEDOT: PSS layers by spin coating in a nitrogen filled glove box. After the organic layers were coated, each device was annealed for 20 minutes at 120°C. The thickness of the organic layers was maintained at 150 ± 10 nm. After completion, calcium and aluminium electrodes (40 nm thick each) were deposited subsequently by a thermal evaporation process. Table 2.5 summarizes the solar cell parameters of 5T-TTF/PC₇₁BM devices fabricated by using two different solvents. In the dark, I-V curves (figure: 2.9a) showed poor rectification in the case of the blend deposited from chloroform. On the contrary, the devices prepared from o-DCB (figure: 2.10a) showed higher rectification, suggesting better diode behaviour due to smoother surface of the active layer and uniform coverage of the PEDOT: PSS layer, resulting in much lower series resistance comparing to the devices from CF.

Upon illuminating under AM 1.5 standard light the devices fabricated with chloroform showed an efficiency of 1.7%. The short circuit current density observed was

7.44 mA/cm², with V_{oc} being 0.7 V. However, due to the developed BHJ interface, the charge carrier transport toward electrodes is dominated by the percolation process, which is sensitive to material morphology and grain size, and tends to result in low efficiency and small fill factor.¹³¹ Conversely, devices made with o-DCB showed higher PCE of 2.5% (as shown in the figure 2.10). The short circuit current density is more significantly affected by the solvent (increased to 9.81 mA/cm²) than the open circuit voltage (0.78 V). The relatively low fill factor (33%) from both cases can be explained by a recombination of charge carriers in the bulk and a contact resistance at the electrode interfaces which requires further investigation.

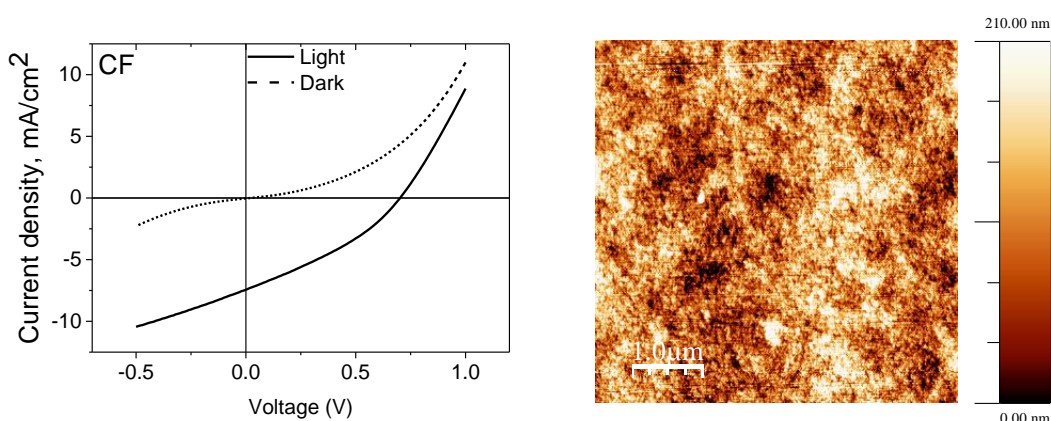


Figure 2.9 : Current density-voltage characteristics under dark and illumination (2.9a, left) for OPV fabricated by spin-coating from chloroform and AFM image in tapping mode of 5T-TTF: PC₇₁BM (1:4) active layer deposited from chloroform (2.9b, right)

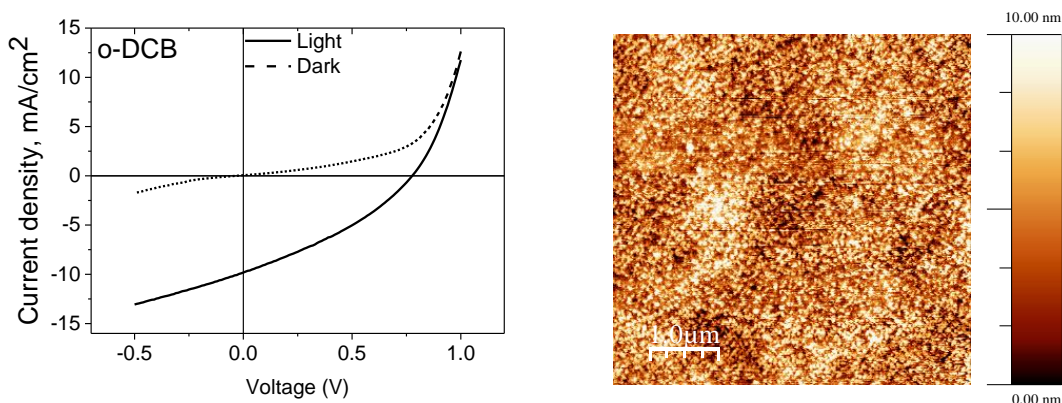


Figure 2.10 Current density-voltage characteristics under dark and illumination (2.10a, left) for OPV fabricated by spin-coating from o-dichlorobenzene and AFM images in tapping mode of 5T-TTF: PC₇₁BM (1:4) active layer deposited from o-dichlorobenzene (2.10b, right)

| Active layer 5T-TTF:PC ₇₁ BM | Solvents used | V _{oc} , V | J _{sc} , mA/cm ² | FF | PCE, % |
|--|------------------|---------------------|---|------|-----------|
| 1:4 | CF | 0.70 | 7.44 | 0.33 | 1.7 |
| 1:4 | o-DCB | 0.78 | 9.81 | 0.33 | 2.5 |

Table 2.5: A collection of the data obtained for solar cell devices: Power Conversion Efficiency (PCE), open circuit voltage (V_{oc}), short circuit current density (J_{sc}), and fill factor (FF)

Although there has been considerable progress in energy conversion efficiencies of OPV devices recently¹³² our results are significantly enhanced in comparison with characteristics of the devices prepared from the blends of fullerene with related donor compounds.^{130, 133} Controlling the morphology of the bulk heterojunction in order to ensure maximum exciton dissociation at the interface between the donor and the acceptor, in parallel to an efficient charge carrier extraction, was found to be the key for high photovoltaic performance. AFM image of quinquithiophene-TTF: PC₇₁BM (1:4) film spin-coated from chloroform (Fig.2.9b) shows a formation of cavities in the BHJ layer with surface roughness of over 50 nm. The morphology of the film in this case might be attributed to the propensity of the blend to phase segregation in CF. It

would decrease J_{sc} due to exciton recombination in larger donor domains.^{134, 135} The surface of the film produced from o-DCB (Fig: 2.10b) was significantly smoother with roughness of about 2 nm. The more homogenous morphology of the film in this case is consistent with more developed interpenetrating nano-scale network which is favourable for effective charge separation and provide increased J_{sc} . It has been shown that vertical orientation of quinquithiophene can be favoured by attachment of linear alkyl chains at backbone of quinquithiophene, and such an orientation would be detrimental for solar cells as it strongly limits the absorption of the incident light as well as the charge transport across the donor phase of the film of the solar cell.²³ In our case the presence of TTF unit in 5T-TTF makes the horizontal alignment more favourable due to donor-acceptor interactions between developed conjugated system of quinquithiophene-TTF and PEDOT-PSS hole injection layer.

2.7 Conclusions

A quinquithiophene/TTF (5T-TTF) hybrid electroactive compound has been used as an organic semiconductor for fabrication of OFET and BHJSC. In summary, we have shown that the performances of field effect transistors with 5T-TTF films are dependent on the preparation conditions such as solvent and SAM surface treatments. Good hole mobilities as high as $9.56 \times 10^{-3} \text{cm}^2/\text{Vs}$ with I_{on}/I_{off} greater than 10^5 are measured. AFM characterization of the spin coated film reveals crystallinity, with the size of crystalline domain being highly dependent on the solvent used for spin-coating. The OFET performance turned out to be better for the films with large crystalline domain obtained by spin coating from chloroform solution. Quinquithiophene/TTF oligomer shows good photovoltaic properties when employed in BHJ devices by

solution process due to its good film forming property and high hole mobility. Tapping mode AFM images were recorded to study the morphology of 5T-TTF: PC₇₁BM (1:4) blend film spin coated from different solvents. The results show that the morphology of the 5T-TTF: PC₇₁BM thin films depends strongly on the preparation solvent. The more homogeneous morphology of the film spin-cast from o-DCB provides better performance for corresponding OPV device than that prepared with CF as a solvent. This is assumed to be due to better developed nanoscale interpenetrated network of the blend in the former case.

Chapter 3

An air stable polymer, p(DPP-TTF) for
OFET and OPV applications

3.1 Abstract

Following an approach developed in the PJS group to incorporate TTF units in conjugated polymeric systems, a new low band gap polymer p(DPP-TTF) has been synthesised and characterised. This polymer is based on a fused thieno-TTF unit which enables the direct incorporation of the TTF unit into the polymer, and a second comonomer is based on a DPP core. These (DPP and TTF) units are well-known for D-A copolymer systems and show strong absorptions in the UV-visible region of the spectrum. Optimized p(DPP-TTF) polymer organic field effect transistor (OFET) and a single layer organic photovoltaic (OPV) device showed excellent performance with a hole mobility of $1.6 \times 10^{-2} \text{cm}^2/\text{Vs}$ and a power conversion efficiency (PCE) of 0.46%. The bulk hetero junction OPV devices of p(DPP-TTF) blended with PC₇₁BM exhibited a PCE of 1.8%.

3.2 Introduction

The performance of organic electronic materials depends largely on the processing conditions used during device fabrication. In the last two decades, a vast number of conjugated materials have been synthesized and characterized (small molecules, oligomers, dendrimers and polymers). These compounds have been extensively tested in different devices such as organic photovoltaics (OPVs),¹³⁶⁻¹³⁸ organic field-effect transistors (OFETs),¹³⁹⁻¹⁴¹ organic light-emitting diodes (OLEDs)^{142, 143} and electrochromic devices.¹⁴⁴ Besides the synthesis and development of new families of materials with improved properties the conditions for fabrication of devices are of great importance for obtaining their best performance. The charge carrier mobility is highly influenced by the nano-morphology of the materials in the bulk which can be controlled by processing conditions and molecular design. A classic and an excellent example to illustrate the importance of both fine synthesis control and device fabrication to obtain the best results is the development of poly (3-hexyl-thiophene), referred to as P3HT. The unprocessability of polythiophenes led first to the incorporation of alkyl chains to obtain polymers soluble in common organic solvents.¹⁴⁵ In 1992, McCullough *et al.*¹⁴⁶ and Rieke *et al.*,¹⁴⁷ synthesized highly regioregular P3HT. In comparison to the amorphous regiorandom P3HT, self-organized and crystalline regioregular P3HT showed a significant increase in conductivity. The relative ease to produce regioregular P3HT along with its stability has led to this polymer being one of the most studied systems in organic electronics. Despite some inherent drawbacks (relatively high band-gap 1.7eV and poor absorption in the visible-near infrared region of the spectrum), regioregular P3HT in combination

with PC₆₁BM has exceeded 5% power conversion efficiency in organic photovoltaic cells.¹⁴⁸ The most common strategy for designing and synthesising low band gap polymeric semiconductors for high performance devices is to use appropriate fused and planar aromatic donor and acceptor building blocks in the conjugated backbone. Diketopyrrolopyrrole (DPP) pigment has proven to be one of the best and suitable choices as an electron acceptor for making donor-acceptor (D-A) copolymers.¹⁴⁹⁻¹⁵² Such D-A copolymers are also called “push-pull” systems due to electron donating (push) and electron accepting (pull) moieties inserted in the main chain. Figure 3.1 presents the structure of thiophene substituted DPP unit (DBT), which is very often used for building up the D-A copolymers. The nature of the conjugated blocks used in the polymer synthesis strongly affects the interchain interactions due to $\pi - \pi$ stacking and non-covalent bonding and changes the electronic energy levels of the semiconductor. Recently, several research groups have synthesized some of the DPP based π -functional low band gap polymeric semiconductors for high performance OFET and OPV applications [Chart 3.1(a-f)].¹⁵³⁻¹⁵⁷ These materials are synthesized via different organometallic couplings routes such as Suzuki and Stille couplings in a straight forward manner using a variety of building blocks combined with thiophene flanked DPP acceptor moiety (DBT) with branched alkyl chain.

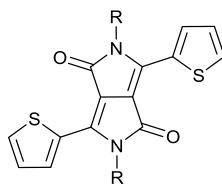


Figure 3.1: The general structure of a DPP-based D–A molecule (DBT)

3.2 OFET studies for DPP-based polymers

DBT is known to be a combination of the electron-accepting DPP core and two electron donating thiophene units. Polymers with DBT as the repeat unit (i.e., DBT homopolymers) are the simplest DPP-based D–A polymers. When the substituents on the DPP core are straight alkyl chains, the resulting polymers are poorly soluble in any solvent because of the very strong intermolecular interactions.¹⁵⁸ When substituted with long branched alkyl side chains such as 2-hexyldecyl or 2-octyldecyl, polymers 3.1a and 3.1b showed good solubility in various solvents. The rather low HOMO and LUMO energy levels (Table: 3.1) are the result of strong electron withdrawing effect of the DPP unit. Such HOMO and LUMO levels would facilitate ambipolar charge transport when a conductor with a suitable work function such as gold or calcium is used as the source/drain electrodes.

The copolymer of DBT and thiophene, 3.1a, was first reported by Bijleveld et al., which exhibited ambipolar charge transport behaviour with hole/electron mobilities of 0.04/0.01 cm²/Vs.¹⁵³ Recently Zhang et al. carried out a further detailed study on polymer 3.1a.¹⁵⁹ It showed unipolar p-type transport behaviour with a high hole mobility of up to 0.6 cm²/Vs in top gate/bottom-contact OTFTs with Au source and drain electrodes. When this polymer was tested in bottom gate/top contact devices with low work function calcium as source/drain electrodes, an electron mobility of up to 1.2x10⁻² cm²/Vs was obtained. Lee et al. investigated the influence of the solubilising substituents of the DPP moiety on the OTFT performance by comparing 3.1a with 3.1b.¹⁵⁴ The polymer 3.1a with 2-octyldecyl side chains showed ambipolar

performance with a hole mobility of $0.14\text{cm}^2/\text{Vs}$ and an electron mobility of $0.02\text{cm}^2/\text{Vs}$ for the non-annealed thin films.

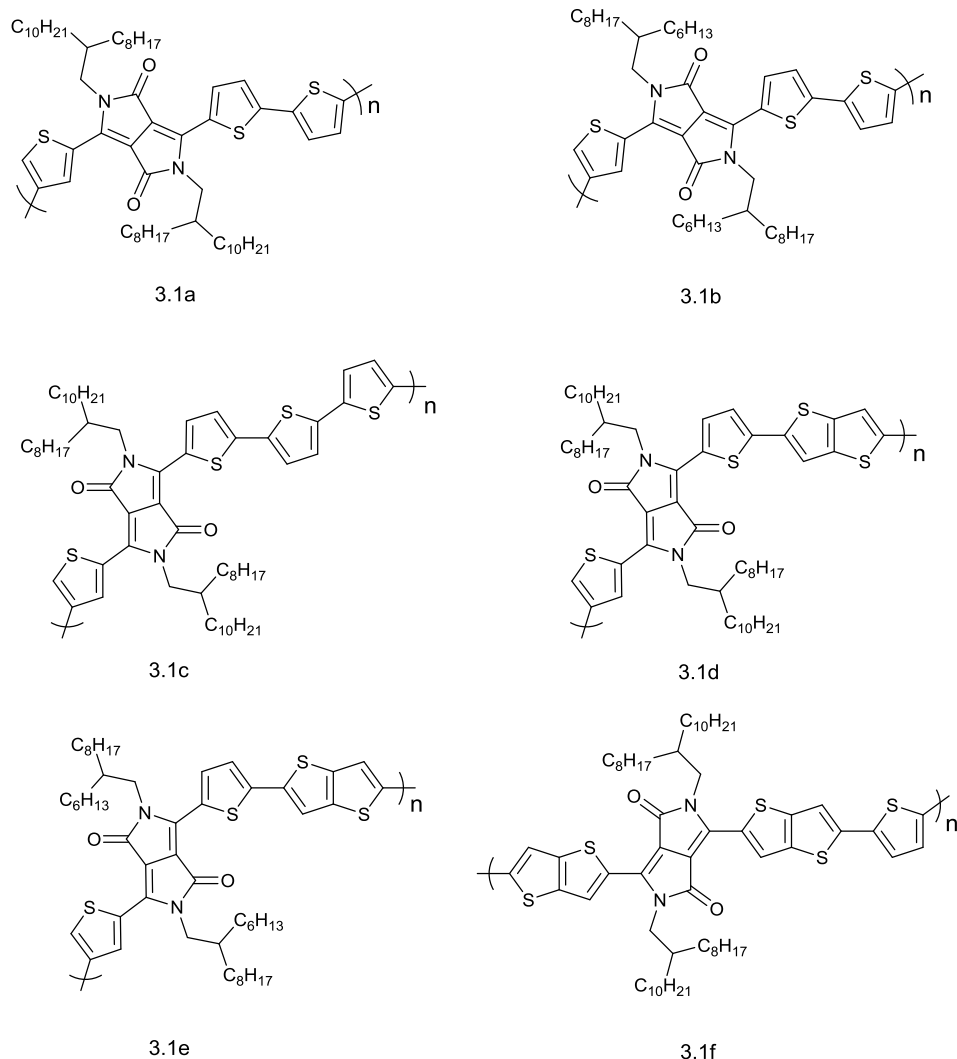


Chart 3.1: structures of DPP-based copolymers with a fused thienothiophene and non-fused thiophene donor moieties.

When the polymer films were annealed at 150°C , both hole and electron mobilities were increased significantly to 1.57 and $0.18\text{cm}^2/\text{Vs}$, respectively. On the other hand, hole/electron mobilities of the polymer 3.1b with smaller 2-hexyldecyl side chains, improved upon annealing to a lesser degree, from $0.11/0.01\text{cm}^2/\text{Vs}$ for the as cast thin films to $0.30/0.12\text{cm}^2/\text{Vs}$ for the sample annealed at 150°C . Copolymer 3.1c,

comprising a DBT and a non-substituted dithiophene in the repeat unit, was developed by Li et al.¹⁵⁵ The optical band gap of polymer 3.1c was estimated to be 1.2eV. It was found that the molecular weight of 3.1c significantly influenced the thin film morphology. The AFM analysis clearly showed that the thin film of high molecular weight (HMW, 106 KDa) 3.1c comprised closely connected nano-grains, while small pinholes were present in the thin film of the low molecular weight (LMW, 45 KDa) polymer. HMW 3.1c exhibited a high hole mobility of up to 0.89 cm²/Vs in OTFTs without thermal annealing, which is very close to the maximum mobility of 0.97cm²/Vs achieved for the 100°C annealed polymer thin films. The significantly improved charge transport property of 3.1c compared with 3.1a and 3.1b is likely due to compensation of the electron-accepting effect of DPP by the long electron-donating quaterthiophene units. Incorporation of a fused ring donor moiety into the backbone of a DBT-based polymer was envisioned to increase the π - π overlap area and to further strengthen the intermolecular interactions.

Based on this consideration, Li et al. designed a copolymer 3.1d comprising a DBT and a thieno[3,2-b]thiophene (TT) in the repeat unit.¹⁵⁶ The HOMO level of 1d (-5.25eV) is very close to that of 3.1c. A hole mobility of 0.94cm²/Vs for the films annealed at 200°C was achieved which is similar to the performance obtained for 3.1c. Later a study by Chen et al. found that 3.1d could exhibit ambipolar transport performance under certain device fabrication conditions.¹⁵⁷ Much higher electron mobility was achieved at a high annealing temperature of 320°C due to the effective removal of electron-traps from the polymer. It was also found that OTFT devices with O₂-plasma treated gold source/drain electrodes showed much lower electron mobility

than that for devices fabricated without an O₂-plasma treatment, due to a higher work function (-5.0 to 5.5eV) of O₂-plasma treated gold compared to that of non-treated one (-4.7 to 4.9eV). The increased work function of the O₂-plasma treated gold would build up an energy barrier for electron injection from gold to the semiconductor. The best ambipolar performance with hole/electron mobilities of 1.18/1.86cm²/Vs was achieved for devices using polymer films annealed at 320°C and gold electrodes without an O₂-plasma treatment. Very recently Lee et al., studied the influence of side chain substitution on the properties of 3.1d and 3.1e.¹⁵⁴ It was found that 3.1d with longer side chains (2-octyldodecyl groups) has higher crystallinity and a more homogeneous surface morphology in thin films compared to that of 3.1e, which has shorter side chains (2-hexyldecyl groups). Both polymers showed ambipolar charge transport performance in OTFTs. After annealing at 150°C polymer 3.1e showed hole/electron mobilities of 0.79/0.04cm²/Vs, while polymer 3.1d showed much higher average hole/electron mobilities of 1.93/0.06cm²/Vs. High molecular weight (M_n=110 kDa) polymer was tested in bottom gate/top contact and bottom gate/bottom contact OTFTs on silicon wafer substrates.¹⁵⁸ All devices showed ambipolar charge transport performance. The hole mobility as high as 10.5 cm²/Vs was achieved, which is the record mobility value reported for polymer based OTFTs so far.

| | M _n /M _w Kg/mol | HOMO, eV | LUMO, eV | μ (h), cm ² /Vs | μ (e), cm ² /Vs |
|------|--|-------------|-------------|-------------------------------|-------------------------------|
| 3.1a | 104/310 | -5.2 | --- | 0.60 | 1.2x10 ⁻² |
| 3.1b | 54/170 | -5.1 | -3.6 | 0.04 | 1.0 x10 ⁻² |
| 3.1c | 25/61 | -5.2 | -4.0 | 0.97 | --- |
| 3.1d | --- | -5.2 | -3.4 | 1.93 | 0.06 |
| 3.1e | 21/81 | -5.3 | -4.0 | 0.79 | 0.04 |
| 3.1f | --- | -5.0 | -3.6 | 1.42 | 0.063 |

Table 3.1: High mobility DPP-based compounds for OFETs

OTFTs based on 3.1d showed good environmental stability with only slight changes in mobility and current on/off ratio after the devices were stored for over one year. DBT is the most widely investigated moiety in DPP-based polymers so far. However, several research groups have also been investigating other DPP building blocks, which have the DPP core flanked by furan (DBF), selenophene (DBS), and thieno[3,2-b]-thiophene units (DBTT). Incorporation of these building blocks was expected to bring about new optoelectronic properties due to their different electronic structures and geometries compared with DBT. One of the examples based on DBTT polymer (3.1f) is shown in the Chart 3.1. Bronstein et al., developed a new building block, DBTT, by replacing thiophenes in DBT with the larger thieno[3,2-b]thiophene (TT) units.¹⁶⁰ The thieno thiophene (TT) units would promote a more delocalized HOMO distribution along the backbone, which was expected to enhance intermolecular charge transport. Due to the strong interchain interactions, the DBTT-based polymer (3.1f) showed poor solubility. This polymer has HOMO/LUMO levels of -5.05/-3.68eV and showed ambipolar transport behaviour in OTFT devices. The results obtained for all polymers clearly indicate that longer side chains are beneficial for achieving improved molecular organization and charge transport.

3.3 OPV studies for DPP-based polymers

In developing new conjugated organic materials for BHJ solar cells, a well-known architecture, alternatively composed of electron-donating and strong electron-accepting units, has been utilized to manipulate their electronic properties in order to attain low band gap, high V_{oc} and efficient charge separation. Electron-donating units

such as phenylene have high aromatic resonance stabilization energy, π -electrons are relatively localized within the phenylene ring in the molecule. Thus, molecular units containing phenylene can be classified as weak electron-donating units. When the weak electron-donating unit is used as a building block for an alternating conjugated copolymer, the copolymer is expected to have a deep HOMO energy level and as a result afford high V_{oc} in OPVs.¹⁶¹ On the other hand, a hetero-aromatic ring such as thiophene has less aromatic resonance stabilization energy; thus, π -electrons are delocalized along the conjugated backbone. As a result, the molecular units containing thiophene raise the HOMO energy level as compared to those containing phenylene.¹⁵³ Such a synthetic strategy can effectively be used to tune the frontier molecular orbital energy levels for high efficiency OPV solar cells. Incorporating both acceptor and donor not only allows to control the HOMO level but affects the energy of LUMO and creates materials with a narrow band gap. As was mentioned above, the polymers with a donor-acceptor component along their conjugated backbone, e.g. polymers (1b-1f), are prone to form an ordered structure in the film which is extremely beneficial for increasing charge mobility.¹⁶²

The HOMO and LUMO levels of polymer 3.1b are -5.17 and -3.68eV, respectively, might be suitable with those of the commonly used electron acceptor material, [6,6]-phenyl-C₇₁ butyric acid methyl ester (PC₇₁BM), (LUMO -4.3eV, HOMO -6.1eV) for bulk heterojunction polymer OPVs.⁴⁷ The LiF/Al back electrode was evaporated in vacuum. Cells with an active layer spin coated from chloroform had a relatively low performance because of formation of larger phase separated domain. Control over the morphology is crucial for bulk-heterojunction solar cells, and several strategies to

accomplish a more favourable morphology, such as thermal treatment and the use of processing additives, have been developed.¹⁶³ Adding a small amount (25 mg/ml) of di-iodooctane (DIO) to the mixture before spin coating significantly improved the efficiency of the cells, mainly as a result of an increase in photocurrent.

| | Solvents Used | D/A ratio | V _{oc} , V | J _{sc} , mA/cm ² | FF | PCE, % |
|------|----------------|-----------|---------------------|--------------------------------------|------|--------|
| 3.1b | CF | 1:2 | 0.65 | 11.8 | 0.60 | 4.7 |
| 3.1c | o-DCB:CF (1:4) | 1:1 | 0.63 | 15 | 0.60 | 5.6 |
| 3.1d | CB | 1:2 | 0.62 | 5.86 | 0.44 | 1.6 |
| 3.1e | CF | 1:1.5 | 0.63 | 2.8 | 0.61 | 1.2 |
| 3.1f | o-DCB:CF (1:4) | 1:2 | 0.58 | 15 | 0.61 | 5.4 |

Table 3.2: OPV results based on DPP-based copolymers

The cell with a blend of 3.1b:PC₇₁BM at a weight ratio of 1:2 provided an open circuit voltage (V_{oc}) of 0.65V, a short circuit current density (J_{sc}) of 11.8mA/cm², and a fill factor (FF) of 0.60, resulting in a high power conversion efficiency (PCE) of 4.7%.¹⁵³

OPVs with polymer 3.1c as a donor and PC₇₁BM as an acceptor were reported by Liu et al.¹⁶⁴ The device performances of as prepared PV cells using 3.1c: PC₇₁BM (1:1 weight ratio) blends were studied under different processing conditions. When only CF was used as the solvent, a low J_{sc} and FF were obtained, indicating a non-optimal charge carrier separation process arising from an ill-defined morphology. Janssen and co-workers reported that a mixture of CF and o-DCB could enhance the performance of a similar DPP polymer.¹⁶⁵ This mixed solvent approach was therefore used here. It should be noted that the solvent mixture of CF and o-DCB behaves very similarly to the additive approach where the solvent dissolves the polymer well while the higher

boiling additive, a non-solvent for the polymer, fully solubilises the PC₇₁BM.^{166, 167} During casting the blend solution, the lower boiling solvent evaporates, continuously increasing the concentration of the additive, thereby reducing the solubility of the polymer, while keeping the PC₇₁BM fully solubilized. The polymer 3.1c will then crystallize into fibrils. Ultimately, the remaining 3.1c and PC₇₁BM will be deposited within the interfibrillar regions, where the polymer can form ordered clusters, forcing a phase separation with the PC₇₁BM. Consequently, a different morphology will be generated than that from a single solvent process. By using o-DCB:CF (1:4 volume ratio), the J_{sc} was significantly improved to 15mA/cm², and the overall device efficiency reached 5.6%. The observed improvement can be directly attributed to the ordering of the polymer enabled by the ability of o-DCB to selectively solubilise the PC₇₁BM.

Zhang et al. evaluated polymer 3.1d as a donor for OPVs using PC₇₁BM as an electron acceptor.¹⁶⁸ At a polymer 3.1d: PC₇₁BM ratio of 1: 2, and with 1, 8-diiodooctane (DIO) as a solvent additive, the best PCE was only 1.6%. Polymer 3.1e also showed poor OPV performance with a PCE of 1.2%.¹⁶⁹ The poor OPV performance of polymers 3.1d and 3.1e was mainly due to their low short circuit currents. An offset energy of 0.3–0.4eV between the LUMO levels of the donor and acceptor is considered the minimum for optimal exciton dissociation.^{170, 171} However, the LUMO–LUMO offset energy between polymers (3.1d, 3.1e) and PC₇₁BM is only 0.24eV, which might be responsible for the poor charge separation and thus low short circuit currents. Also, the moderate performance on PCE of polymer solar cell devices is likely attributed to un-optimized composite morphology. When straight dodecyl and branched hexyldecyl

chains were used in dithiophene-diketopyrrolopyrrole (DT-DPP) monomers, the resulting polymers were completely insoluble in any solvent. Larger branched side chains had to be used in synthesis of this polymer that effectively improved the solubility of the polymer. However, bulky side chains might also greatly reduce the crystallinity and the hole mobility of a polymer, thereby, result in low device performance. In OPV devices based on polymer 3.1f: PC₇₁BM blend at a ratio of 1:2 a PCE of 5.4% with J_{sc} of 15mA /cm², V_{oc} of 0.58V and FF of 0.61 are achieved. An increase in PCE exhibited by polymer 3.1f was explained by the authors to be a result of the larger distance between the DPP moieties which would allow for intercalation of the acceptor molecules.¹⁶⁰ It is also suggested that the increased distance between the solubilizing alkyl chains in polymer 3.1f results in reduced steric interactions that could improve the nature of the polymer packing in the solid state. The nature of the solid-state packing has been found to profoundly influence the charge-carrier mobility or solar cell performance of a conjugated polymer. In all cases of polymers [Chart 3.1(a-f)] the PCE values have been obtained after steady improvement in fabrication conditions of the devices such as solvents, thermal annealing, blend (polymer/PCBM) ratio and a better understanding of the correlation between morphology and photo generated charge carrier dynamics. Another way to control the bulk morphology by the polymer design is incorporation of such a strong electron-donor as tetrathiafulvalene (TTF) by fusing it to the conjugated backbone. The well-known electron donor tetrathiafulvalene (TTF) (explained in detail in chapter 2) and its derivatives have been extensively used as small molecules in the preparation of highly electrical conducting mixed valence salts;¹⁷² however the incorporation of the TTF unit into conjugated polymer architectures has been less studied. In our group, we

developed a methodology for the synthesis of a thieno-TTF fused heterocyclic system which can be directly incorporated into the conjugated backbone through a thiophene ring.^{113, 114} Recently, we have synthesized a novel conjugated polymer p(DPP-TTF) (fig: 3.2) with donor thieno-TTF and electron acceptor diketopyrrolopyrrole (DPP) units within the conjugated backbone and reported its performance in OFETs under ambient conditions. Optical, thermal, and electrochemical properties as well as nano morphology of this polymer indicated that it is a promising material for OFET and OPV applications.⁷² Here, we report a more in depth study of the photovoltaic properties and the optical characteristics. Interestingly, we have found a remarkable power conversion efficiency for the single material organic solar cell (SMOC) with p(DPP-TTF) as a semiconductor. These values are comparable to those observed for the SMOCs fabricated from a fully donor-acceptor conjugated polymer.¹⁷³ Recently, a SMOC fabricated with P3HT and C₆₀ derivatized copolymer gave an efficiency of 1.70% and J_{sc} of 6.15mA/cm² and these values are the highest reported so far for SMOC.¹⁷⁴ Equally, we also have investigated the processing induced morphology related charge carrier transport using OFET characteristics and AFM microscopy.

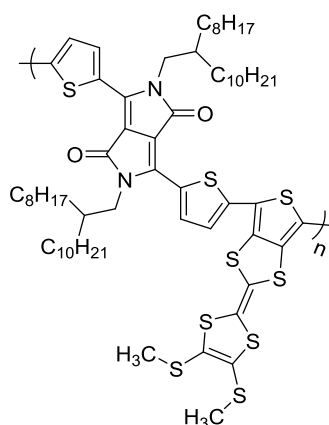


Figure 3.2: Chemical structure of diketopyrrolopyrrole-tetrathiafulvalene polymer, p(DPP-TTF)

3.4 OFET results for DPP-TTF polymer

Figure 3.3 shows the output characteristics for p(DPP-TTF) devices fabricated from CF and CB solutions separately and measured at different gate voltage up to -90V at intervals of -10V.

| | Substrate | Geometry | Capacitance per unit area, F/cm ² | solvent used | V _{gs} interval range, V | V _{ds} , V | I _{on} /I _{off} | μ, cm ² /Vs | V _{th} , V |
|---|---------------------|--------------|--|--------------|-----------------------------------|---------------------|-----------------------------------|------------------------|---------------------|
| A | Si/SiO ₂ | TG/ CYTOP | 2.1x10 ⁻¹⁰ | CB | -50-80 (sat) | -70 | 10 ⁴ | 3.8x10 ⁻² | -30 |
| | | | | | -40-65 (lin) | -20 | 10 ⁴ | 1.2x10 ⁻² | -20 |
| B | Si/SiO ₂ | TG/ CYTOP | 2.1x10 ⁻¹⁰ | CF | -50-80 (sat) | -70 | 10 ⁴ | 5.3x10 ⁻² | -38 |
| | | | | | -60-80 (lin) | -15 | 10 ⁴ | 3.8x10 ⁻² | -40 |
| C | Si/SiO ₂ | BG/ ODTS | 1.7x10 ⁻⁸ | CF | -30-58 | -50 | 10 ⁴ | 7.3x10 ⁻³ | -8.6 |
| | | | | | -50-80 | | | 2.0x10 ⁻² | -39 |

Table 3.3: OFET performance for devices of various configurations fabricated using different solvents

Figure 3.4 shows the transfer characteristics of an OTFT device with p(DPP-TTF) thin film annealed at 200°C for half an hour. Devices ‘A’ and ‘B’ were fabricated using top gate configuration and cytop as an insulator while device ‘C’ was constructed using SiO₂ as gate dielectric with bottom gate as shown in table 3.3. Electron mobility measurements were also attempted by using a low work function metal such as calcium and molybdenum as source and drain electrodes, but we did not observe any decent output or transfer characteristics. Due to the presence of the TTF unit, the HOMO may be spatially extended compared to the LUMO that is localised on the DPP.¹⁷⁵ So it is highly unlikely that there is any meaningful overlap between LUMOs, which is necessary to provide electron mobility. This is confirmed by comparing HOMO and LUMO levels of the polymer in solution and the solid state.

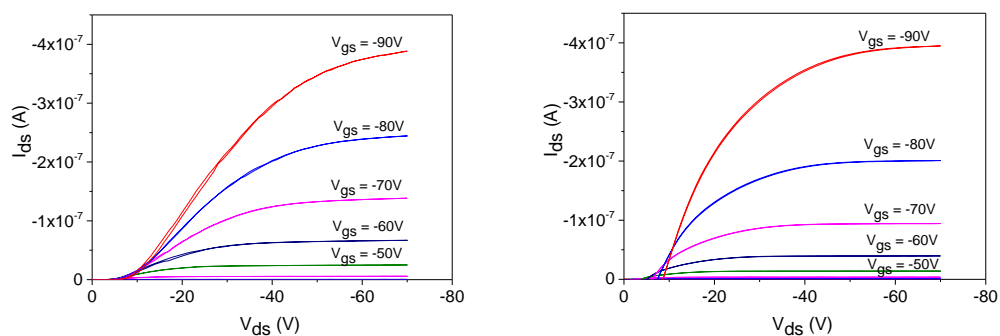


Figure 3.3: Output characteristics of OFETs fabricated by spin-coating of p(DPP-TTF) from chlorobenzene (3.3a, left) and chloroform (3.3b, right) solutions. Measurements at gate voltage intervals of -10V in a top gate configuration.

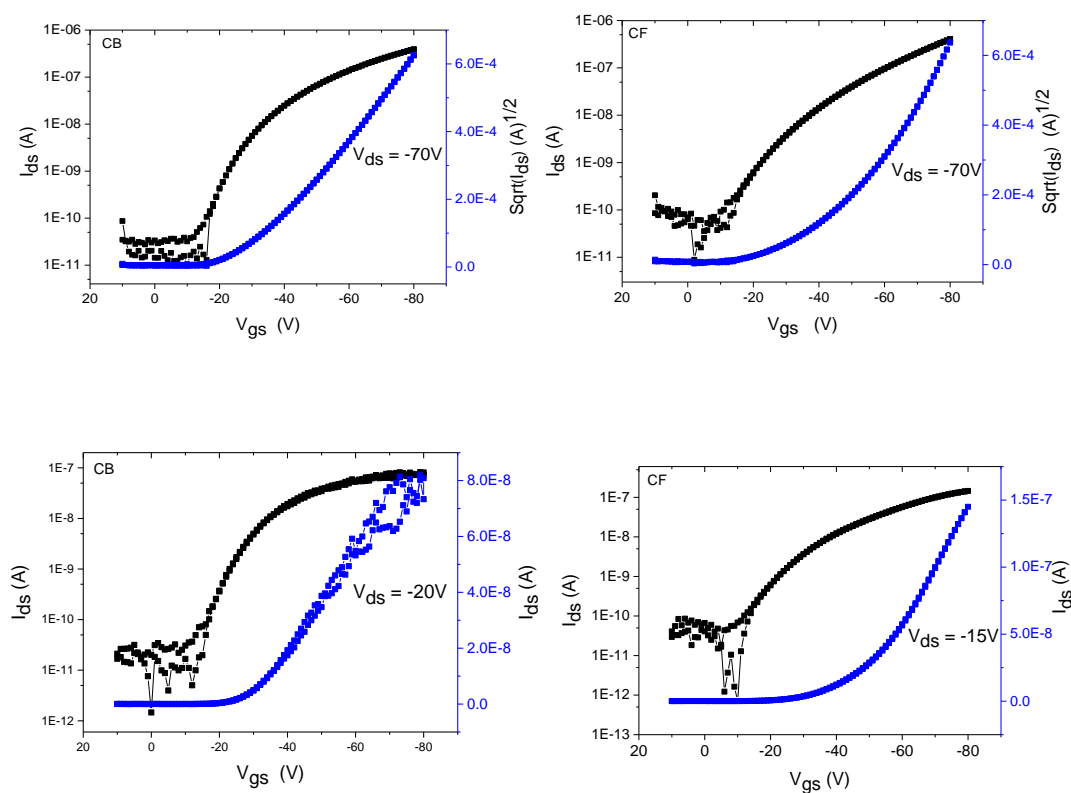


Figure 3.4: Transfer characteristics of OFETs fabricated by spin coating of p(DPP-TTF) from chlorobenzene (left) and chloroform (right), measured in a top gate configuration at V_{ds} of -70V (upper panels) and at V_{ds} of -20V (for CB, left bottom panel) and -15V (for CF, right bottom panel).

As was reported before⁷² the polymer in the solid film has a deeper HOMO (-5.13eV) and a little bit more shallow LUMO (-3.49eV) level than those in solution

(HOMO of -4.95eV and LUMO of -3.55eV), which is the evidence of π - π interactions between donor and acceptor sites in the solids. However, the realization of high I_{on}/I_{off} values in DPP based semiconductors should prove invaluable in optimizing organic transistors based on this air stable, solution processable, p-type organic semiconductors. To gain a better understanding of the morphology effect on the charge carrier mobility, atomic force microscopy (AFM) has been utilized to describe the distinctive feature of the polymer. Tapping mode AFM images (figure 3.5) were recorded on the same devices used for OFET measurements. AFM images showed that the film formed from CB is composed of closely packed grain like structures with quite small size of domains and really flat surface (rms of 0.53 nm). This type of morphology is due to the strong propensity of p(DPP-TTF) to aggregate in this solvent. Upon annealing the rate of grain nucleation, higher the rate of their growth which produces small crystalline domains with the structures formed by strong π - π inter-chain interactions between donor and acceptor sites. Previously, similar tight grain packing morphology in the case of poly(2,5-bis(3-hexadecylthiophen-2-yl)thieno[3,2-*b*]thiophene proved to be beneficial for OFET applications.¹⁷⁶ For this type of morphology the top-gate OFET device revealed a hole mobility of $3.8 \times 10^{-2} \text{cm}^2/\text{Vs}$ in saturation and $1.2 \times 10^{-2} \text{cm}^2/\text{Vs}$ in linear regime.

The situation with morphology of the thin film spin-coated from CF solution is different. The energy of solvation in this solvent should be higher than that in CB due to interaction of polarised C-H bond of the solvent molecules with TTF and with lone pairs of DPP carbonyl oxygen atoms. This will prevent quick formation of the aggregate, so the rate of nucleation in this case is going to be lower than the rate of

grain growth upon annealing. This leads to morphology of the film with larger size of domains. The situation with the effect of the solvent used for spin-coating on the morphology of the film is similar to that we observed above for 5T-TTF compound (see previous chapter). As in the 5T-TTF case, here we've got a higher mobility observed for top gate configuration of the OFET fabricated by spin-coating of p(DPP-TTF) from CF ($5.3 \times 10^{-2} \text{cm}^2/\text{Vs}$ in saturation and $3.8 \times 10^{-2} \text{cm}^2/\text{Vs}$ in linear regime) compared to that from CB, which makes us conclude that in the former case the relative stability of solvated states in the film produce upon annealing not only a larger size of crystalline domains but a smoother grain boundary as well, which conforms with a still small roughness of the surface (rms of 4.5nm). The bottom gate configuration had been tried for OFET fabricated by spin-coating of p(DPP-TTF) from chloroform, which exhibited the lower device performance.

The mobility values in p(DPP-TTF) thin film with SiO₂ gate electric (figure 3.6b, right) were largely different when estimated from the forward and reverse sweeps because of a large hysteresis. The hysteresis gap (ΔV_{th}) is defined as the difference in threshold voltage between the backward and forward V_{gs} sweeps, as determined by the linear extrapolation method. The observed hysteresis is a current-increasing type, where I_{D} was lower during the backward sweep of V_{ds} than I_{ds} during the forward sweep. It is frequently observed in the current-voltage (I/V) characteristics of organic semiconductor devices, and can complicate the mobility extraction.¹⁷⁷ From the forward sweep the calculated mobility was $7.3 \times 10^{-3} \text{cm}^2/\text{Vs}$ with threshold voltage of 8.6 V.

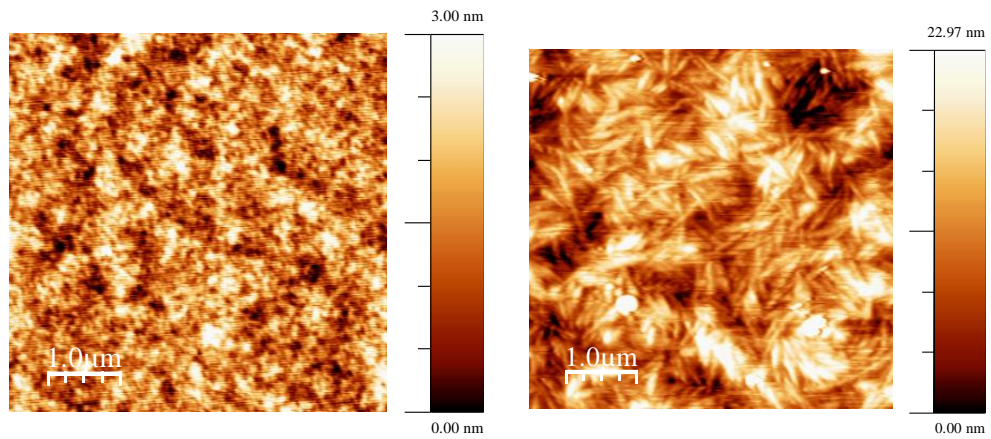


Figure 3.5: Tapping mode AFM height images of p(DPP-TTF) using chlorobenzene (3.5a, left) and chloroform (3.5b, right) as solvents on PFBT and ODTS treated SiO₂ surfaces after annealing at 200°C for half an hour.

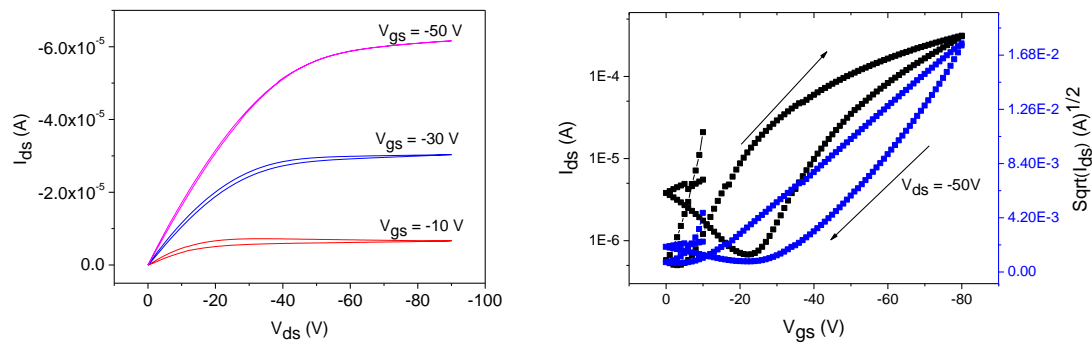


Figure 3.6: Output characteristics (3.6a, left) and transfer characteristics (3.6b, right) of p(DPP-TTF) in chloroform on ODTS treated Si/SiO₂ substrates

Conversely, from the reverse sweep the mobility is increased more than twice ($2.0 \times 10^{-2} \text{ cm}^2/\text{Vs}$) with V_{th} of 39V because of the higher drop of current on the backward sweep of V_{gs} . We list in table 3.3 the calculated mobility and threshold voltage for both cytop and SiO₂ gate dielectrics. Hysteresis showed on-to-off transfer curves shifted towards a higher V_{gs} (figure 3.6, right) compared with off-to-on sweeps. There are two possible mechanisms that can link the structural change with the current (I_{ds}) increase: (1) slow polarization of gate dielectric, (2) charge trapping and detrapping at the

semiconductor/dielectric interface.^{178, 179} While attempting the treatment of ODTS (SAM) layer on SiO₂ substrates, some of the ODTS molecule may appear to be hydrolysed and these hydroxyl groups at the dielectric interface may appear to act as ionic impurities which are capable of slow polarization under applied voltage.¹⁷⁸ When the gate is swept from off to on, polar species in the dielectric medium are polarized at the interface between the semiconductor and the gate electrode. If the polarized species do not respond quickly to the changes in the gate electric field, they may remain polarized without being able to return to their original sites during the on-to-off gate sweep. As a result, the on-to-off transfer curve shifts to higher V_{gs} values compared to the off-to-on sweep.¹⁸⁰ Slow polarization also artificially increases the capacitance of the gate dielectric, resulting in a large increase in I_{ds} and the overestimation of mobility.

Recently Gu and Kim et al found that, in the case of pentacene based OFETs containing OTS modified SiO₂ dielectrics, the hysteresis observed during the full swing of a gate was due to long lived charge traps present at the interface between semiconductor and gate dielectric, where trapping and detrapping of holes and electrons took place under an applied gate voltage.^{178, 181} This concludes that the extraction of mobility from both forward and reverse sweep in the case of device 'C' does not correspond to the field effect characteristic only. However the complete absence of hysteresis in the case of devices 'A' and 'B' thin film FETs with cytop gate dielectric may be due to more hydrophobic nature of the cyclic fluoropolymer than SiO₂ gate dielectrics. The performance of devices 'A' and 'B' highlights the advantage of top gate configuration where the channel is not affected by the possible impurities introduced by a chemical treatment of substrate surface. Another advantage of the

devices 'A' and 'B' is application of cytop as a dielectric with low permittivity. Although the higher dielectric constant of gate insulator provides a higher charge injection in the channel at the same gate voltage and can be used for lowering operational V_{gs} ,¹⁸² using low permittivity polymers allows us to avoid trap states by reducing energetic disorder. An extensive study of fluoropolymer and the other low-k polymer based gate dielectrics has previously been done by Veres et al in regards to their application with solution processed organic semiconductors.¹⁸³ The hole mobility of p(DPP-TTF) semiconductor might be improved by adjusting the structure of the polymer. Shorter branched alkyl substituents might be beneficial for increased π -stacking interactions and polymer crystallinity.¹⁸⁴

3.5 OPV results for blend layer and single layer

Bulk hetero-junction solar cells (BHJSCs) were fabricated from p(DPP-TTF):PC₇₁BM in both o-DCB and CF. The HOMO and LUMO levels of p(DPP-TTF) are -5.13eV and -3.49eV, respectively, which match well with those of the commonly used electron acceptor material, (PC₇₁BM), for bulk heterojunction (BHJ) polymer OPVs. The ratio of 1: 4 was found to be optimum for this system. Figure 3.7 shows the OPV characterises of p(DPP-TTF):PC₇₁BM (1:4) blend spin cast from CF. The device prepared by spin coating of CF solution has a J_{sc} of 4.9mA/cm², a V_{oc} of 660 mV and a power conversion efficiency of 1.0%. However, the devices prepared with o-DCB showed a 2-fold increase in PCE over those spin coated from CF. These o-DCB devices (figure 3.8) exhibited a fill factor of 0.32, a V_{oc} of 710mV and a J_{sc} of 8 mA/cm² and PCE of 1.8% as shown in Table 3.4. Figures 3.7 (right) shows the tapping mode AFM images of OPV device fabricated by spin-coating of p(DPP-

TTF):PC₇₁BM(1:4) blend from chloroform solution annealed at 120°C for 20 minutes and reveals a coarse surface morphology consisting of discontinuous film (dark areas) with mostly clustered blend matrix. This can be a sign of an increased demixing between p(DPP-TTF) and PC₇₁BM.

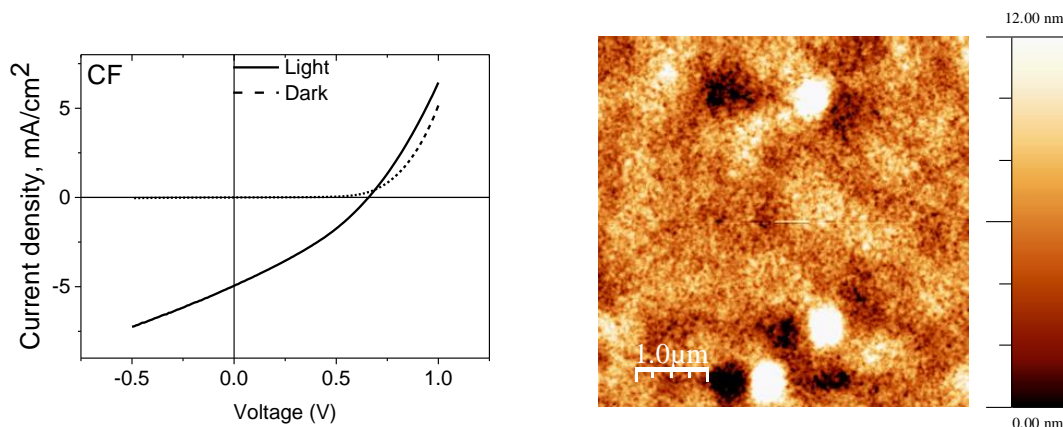


Figure 3.7: I/V curves (left) of OPV fabricated by spin coating of p(DPP-TTF):PC₇₁BM (1:4) blend from chloroform solution after annealing at 120°C. AFM image (right) of p(DPP-TTF):PC₇₁BM films spin-coated on ITO/PEDOT:PSS substrates and annealed at 120°C for 20 minutes

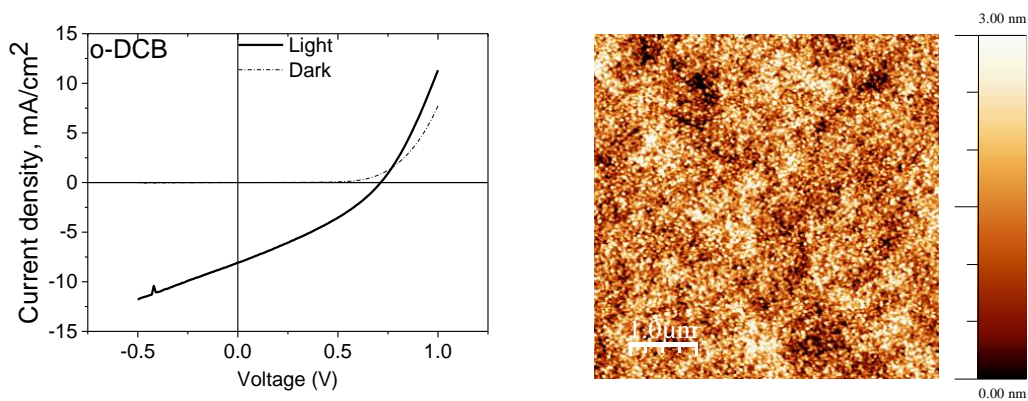


Figure 3.8: I/V curves (left) of OPV fabricated by spin coating of p(DPP-TTF):PC₇₁BM (1:4) blend from o-dichlorobenzene solution after annealing at 120°C. AFM image (right) of p(DPP-TTF):PC₇₁BM films spin-coated on ITO/PEDOT:PSS substrates and annealed at 120°C for 20 minutes

| Active layer p(DPP-TTF):PC ₇₁ BM | Solvents used | V _{oc} , V | J _{sc} , mA/cm ² | FF | PCE, % |
|--|------------------|------------------------|---|------|-----------|
| 1:4 | CF | 0.66 | 4.9 | 0.31 | 1.0 |
| 1:4 | DCB | 0.71 | 8.0 | 0.32 | 1.8 |
| 1:0 | DCB | 0.61 | 1.8 | 0.28 | 0.3 |

Table 3.4: Comparison of device characteristics for OPV fabricated with using different solvents and annealed at 120°C. Here, J_{sc} is the short circuit current density, V_{oc} is the open-circuit voltage, FF is the fill factor, and PCE is the overall power conversion efficiency.

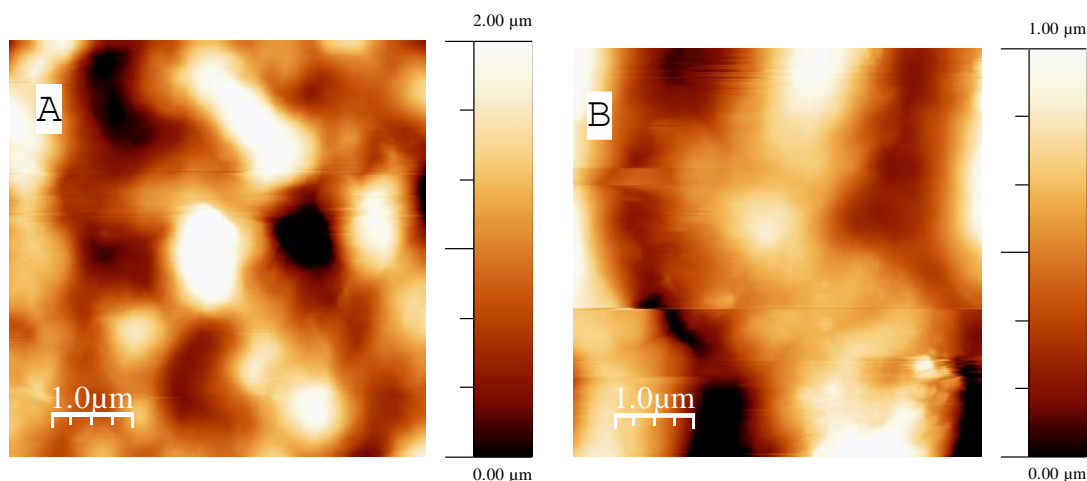


Figure 3.9: AFM images of p(DPP-TTF):PC₇₁BM films spin-coated on ITO/PEDOT:PSS substrates and annealed at 120°C for 20 minutes. Height images for 1:5 (A) and 1:6 (B) blend ratios from o-dichlorobenzene.

On the contrary the p(DPP-TTF):PC₇₁BM film spin-cast from o-DCB (figure 3.8, right) exhibits more homogenous morphology than that from chloroform (figure 3.7, right). This homogeneous morphology provided by more pronounced donor-acceptor interactions in this solvent leads to more developed nano-scaled interpenetrating network and hence a relatively higher PCE of 1.8%. As the blend ratio increases to 1:5 and 1:6, the p(DPP-TTF) and PC₇₁BM domains seems to segregate into larger domains as observed in figure 3.9. This results in poor charge carrier transport in addition to lower fill factor and open circuit voltage. SMOC devices of p(DPP-TTF) were prepared by spin-coating from o-DCB, since bulk hetero-junction solar cell fabricated

from p(DPP-TTF) :PC₇₁BM in this solvent showed better performance than that in CF, and subsequent annealing at 120°C for 20 minutes. SMOC exhibited a power conversion efficiency of 0.3% with a J_{sc} of 1.8 mA/cm² and V_{oc} of 610mV. The I/V characteristics of the device and the AFM image of the film are shown in figure 3.10. The SMOC PCE is modest compared to those of the devices fabricated from donor – acceptor block copolymers,^{66, 185} due to poor charge separation and lack of electron mobility in DPP-TTF copolymer. Nevertheless, the design of the DPP-TTF copolymer with its electronic properties appears to be elegant for SMOC application. This outcome also gives large input into the field of fully functionalized self-organizing molecular devices and molecular electronics in general.^{43, 186, 187} To rationalise these findings, we investigated the semiconductor morphology of the thin films (figure 3.10 (right)). Though the overall surface roughness is very low (rms of ca. 1.0 nm), there are larger particle-like grain structures embedded into the uniform domains and cavities. These particle-like grain structures and cavities are detrimental to charge carrier transport and results in an overall lower PCE.

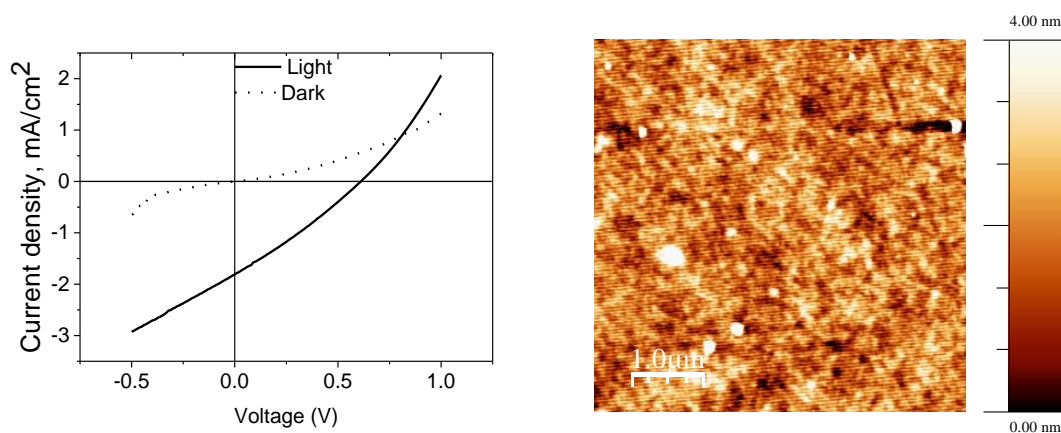


Figure 3.10: I/V characteristics (left) for p(DPP-TTF) as a single component OPV and AFM height image (right) of pure polymer DPP-TTF film spin-coated on ITO/PEDOT: PSS substrates and annealed at 120°C for 20 minutes.

3.6 Conclusions

In summary, we have demonstrated that the donor-acceptor copolymer, containing DPP and TTF units, is a high mobility p-type semiconductor for organic thin film transistors and solar cells. The best solvent for fabrication of OFETs has been found to be chloroform, which provides larger crystalline domains with smoother grain boundaries. Here, we report on combinations of the p(DPP-TTF) semiconductor with fluoropolymer (cytop) and SiO₂ gate dielectrics, which lead to field-effect transistors with unprecedented electrical air stability. The best solvent for OPV fabrication is o-DCB (1.8%), which provides the device with more developed nano-scale interpenetrating network compared to chloroform. The effect of the solvent on morphology of the films of p(DPP-TTF) and its blends with PC₇₁BM and on device performances is similar to that for 5T-TTF. The lack of electron mobility observed in OFET measurements could be the reason for low power conversion efficiency in single component solar cells.

Chapter 4

Oligothiophene cruciform with a germanium spiro center (5T-Ge): A promising material for organic field effect transistors

4.1 Abstract

Increasing the dimensionality of intermolecular interactions in organic semiconducting materials is a promising strategy for improving electronic device performance.^{188, 189} The most studied multidimensional conjugated systems for organic electronics are based on star-shaped oligomers and dendrimers, which exhibit improved device performance compared to their linear analogues.^{190, 191} Swivel-type oligothiophene cruciforms were shown to form crystalline films and provide promising materials for field effect transistors.¹⁹² In contrast, rigid spiro-centered cruciform conjugated structures were believed to discourage aggregation and were therefore considered suitable for applications as highly luminescent materials.¹⁹³ Recently it has been shown that a Ge spiro-centered oligothiophene cruciform structure (5T-Ge) 4,4',6,6'-tetrakis(3'-hexyl-5'-methyl-[2,2'-bithiophen]-5-yl)-2,2'-spirobi[thieno[3,4-d][1,3,2]dithiagermole] self-assembles with the formation of efficient π - π stacking in two mutually orthogonal directions yielding a material which can be used as a donor for efficient bulk heterojunction solar cells.⁷³ Chapter four demonstrates the fabrication of field effect transistors using two different solvents (chloroform and chlorobenzene) with 5T-Ge as a semiconducting material. We also show that the morphology of Ge-cruciform is greatly affected by post-processing thermal treatment and that this change in morphology can lead to favourable charge transport and improved device performance.

4.2 Concept of spiro linkage

In recent years, an intense multidisciplinary research effort has generated considerable progress in the performances of devices based on OSCs, by using a few classes of active materials derived from 1D conjugated system. Although these materials can reach high charge-carrier mobilities, the anisotropy of their electronic properties can be a source of problems, especially for the fabrication of devices in which the directionality of charge transport is particularly critical. Until now, solutions to this problem have been sought in the frame of the optimization of the material processing. However, this physical approach is likely to complicate device fabrication, especially when dealing with large area and flexible substrates. Because these problems clearly originate from the anisotropy of linear π -conjugated systems, the development of OSCs with higher dimensionality of a conjugated backbone and an isotropic charge transport could represent an exciting alternative strategy. Swivel cruciform 2D conjugated systems represent a first type of chemical structure solution to the anisotropy problem and these compounds have attracted increasing interest.

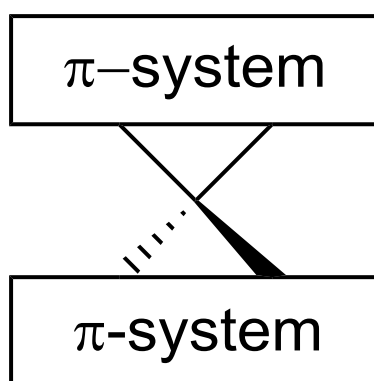
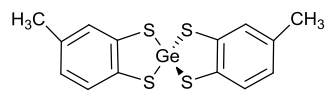


Figure 4.1: Generic spirocentre structure

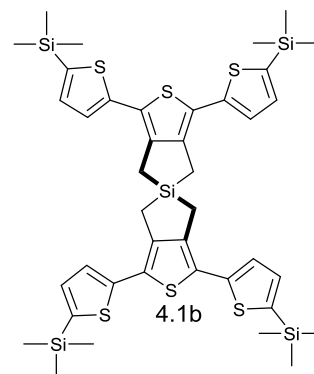
Spirocyclic compounds have been widely studied for materials applications and have demonstrated promising properties for use in a number of organic electronic devices¹⁹⁴⁻¹⁹⁶ notably as hole transport mediums in highly efficient solid-state dye sensitized solar cells (DSSC).^{197, 198} Spiro-linked conjugated molecules feature two conjugated chains which are connected orthogonally via a common tetrahedral sp^3 -hybridised atom (figure 4.1).¹⁹⁴ Despite the perpendicular arrangement of the two halves of the molecule brought about by the sp^3 spirocentre there is evidence of electronic communication between the two spiro-linked π -systems.¹⁹⁴ If the extent to which the two halves of the molecule interact can be improved, then the benefits of longer effective conjugation lengths, such as reduced and tunable HOMO-LUMO gaps can be accessed. One way to achieve this could be to increase the electron density around the spirocentre.

A small number of aromatic or extensively unsaturated/conjugated spirocyclic bis(dithiolate) compounds featuring C¹⁹⁹⁻²⁰¹ and Si²⁰² centres have been developed. Compounds containing spirocyclic bis(dithiolate) Ge, centres,^{200, 203} referred to as 2,2'-spirobi[[1,3,2]dithiagermole], are rarer but some examples were reported since the first synthesis of molecules of this class, featuring Si, Ge, Sn and Pb spirocentres (chart 4.1a), in 1966.^{204, 205} The electron rich nature of the chelating thiolene moieties as in 4.1a, and the conductivity and superconductivity observed from its transition metal complexes have been widely and continuously explored for almost 50 years.²⁰⁶⁻²⁰⁹ However, "complexes" featuring main group element spiro-centres have been much less widely explored.²¹⁰ Similarly linked bis (oligothiophenes), fused to a common all carbon spiro [4, 4] nonane or Si centred 5-silaspiro [4, 4] nonane have been reported in the 1990's as shown in chart 4.1b.^{59, 211} Salbeck and co-workers have developed

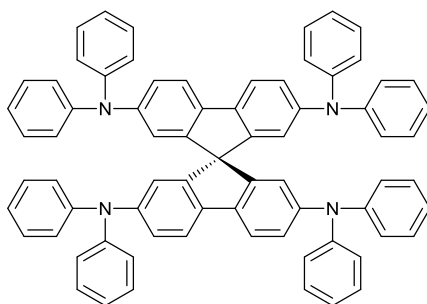
molecular materials based on hybrid 3D systems combining triphenylamine (TPA) and spirobifluorene (chart 4.1 c).^{191, 197, 212}



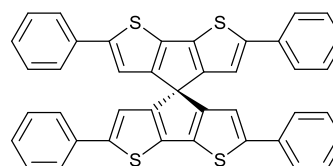
4.1a



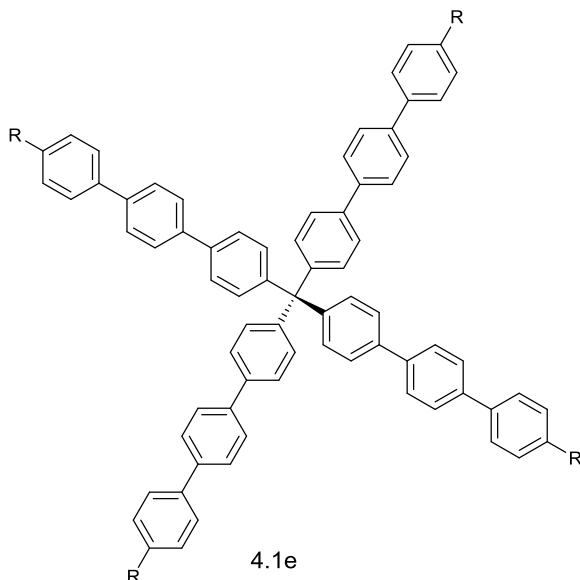
4.1b



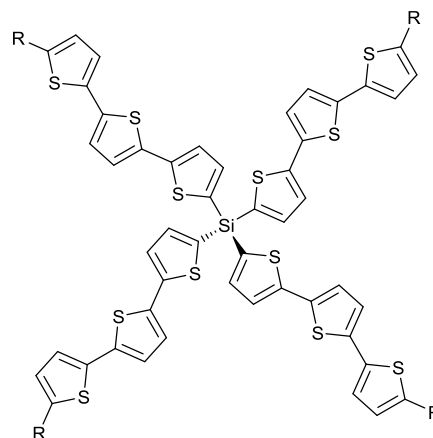
4.1c



4.1d



4.1e



4.1f

Chart 4.1: Compounds containing spirocyclic bis (dithiolate) with 'Ge' and 'Si' spiro-centres

In case of symmetrically spiro-linked compounds, the molecules have two identical chromophores connected through a central carbon atom. These conjugated systems have been used as hole-transporting materials in light-emitting devices²¹³ and solar cells.¹⁹⁷ Field-effect transistors have been realized by thermal evaporation of compounds 4.1c and 4.1d on bottom-contact SiO₂ substrates. The devices show rather low hole mobilities of $7 \times 10^{-5} \text{cm}^2/\text{Vs}$ for 4.1c and $2 \times 10^{-4} \text{cm}^2/\text{Vs}$ for 4.1d, but a high on/off ratio and excellent long-term stability.^{212, 214} More recently, the same group has analysed the charge-transport properties of a series of spiro-linked hybrid compounds of the TPA/spirobifluorene family with reference to the parent linearly conjugated systems.¹⁹¹ Though, only few examples were reported for OFET characteristics in case of spiro-linked compounds, various examples of extended conjugated systems with tetrahedral geometry have been developed in recent years.²¹⁵⁻²¹⁸ Wilson and Griffin first reported tetrahedral molecules with oligo-p-phenylene arms.²¹⁵

A family of monodispersed star-shaped macromolecules has been prepared (chart 4.1e). The controlled and efficient synthesis of molecules of this type would provide synthetic foundation for the molecular engineering approach to the design and construction of complex macromolecular targets. Tetrahedral star shaped molecules comprising a silicon centred core and four conjugated terthiophene arms (chart 4.1f) with solubilising alkyl or alkylthio-substituents in terminal positions have been used as a donor material in heterojunction solar cells.¹⁸⁹ The interest in such systems is attributed to the random orientation of the conjugated segments in films of the 3D compounds, which allows a better absorption of the incident light compared to the vertically oriented chains of the linear systems and diminishes anisotropy in charge

carrier mobility. It would be interesting to develop parent systems containing longer conjugated branches or segments specifically tailored for shifting the absorption towards longer wavelengths. However, the use of the silicon node poses some particular problems related to the relative weakness of the silicon–thiophene bond.²³ To this end, charge transport in star shaped or cruciform systems with high dimensionality is inferior compared to linear and highly crystalline molecules. It remains a challenge, therefore, to identify a core structure that will ‘seed’ a molecule with high dimensionality into a material with an isotropic charge transport.¹⁸⁸ With all these in mind, a novel bis(quinquithiophene) cruciform with germanium as a spirocentre has been reported recently.⁷³ The use of a tetrathiolato germanium spirocentre in place of the traditional solely carbon based one has been explored. Ge is the first of the group 14 elements to possess a full d-shell and is much more electron rich than either C or Si; as such it could be expected to support an increased level of spiro-conjugation.

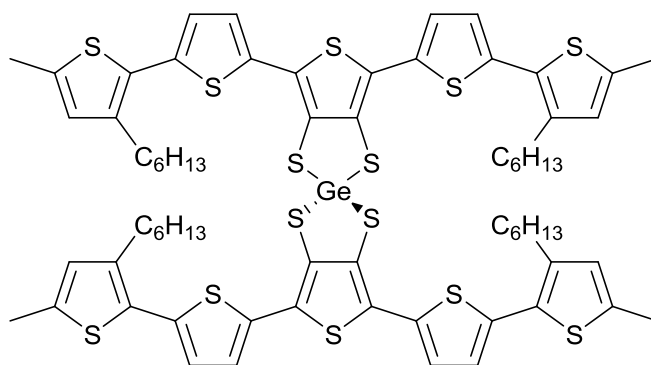


Chart 4.2: New 2,2'-spirobi([1,3,2]dithiagermole) molecule.

The use of a group 14 element in place of a metal centre can give access to purely covalent compounds featuring electron rich dithiole rings bound via a neutral,

tetrahedral sp^3 centre, an area that is largely overlooked for the development of unique and useful new materials. The optical HOMO-LUMO gap of 5T-Ge material obtained was 2.47eV. The HOMO and LUMO levels were observed as -5.00 and -3.64eV respectively. Time-of-flight (TOF) measurements give a mobility of $4.2 \times 10^{-5} \text{cm}^2/\text{Vs}$ for bis(quinquithiophene) material, chart 4.2.⁷³ Thus, in this chapter, the field effect mobility for this material has been extensively investigated. To explore the transport properties and processing possibilities of this new material, field-effect transistors (FETs) were fabricated by a number of methods some of which are discussed here. OFETs were fabricated on PFBT-Au treated SiO_2 substrates to evaluate the device performance with 5T-Ge as a semiconductor. The representative output and transfer electrical characteristics of bottom contact, bottom gate devices A, B,C and D fabricated on the chip with the channel length (L) of 10 μm and the width (W) of 1cm by spin-coating from two different solvents (CF and CB) are compared. Field effect mobilities and threshold voltages (V_{th}) were calculated from transfer characteristics in the saturation regime defined by standard FET models by fitting the $\sqrt{I_{\text{ds}}}$ versus V_{gs} data at $V_{\text{ds}} = -50\text{V}$ in all the cases. Also extracted from transfer characteristics are the turn on voltage (V_{th}) and the on/off current ratio ($I_{\text{on}}/I_{\text{off}}$). The parameters characterizing the device performance such as μ , V_{th} and $I_{\text{on}}/I_{\text{off}}$ are summarized and compared in Table 4.1.

| | Dielectric (nm)/Au modifying agent | Solvents used | Annealing, °C | V _{gs} interval range, V | μ, cm ² /Vs | I _{on} /I _{off} at V _{ds} of -50V | V _{th} , V |
|---|------------------------------------|---------------|------------------|-----------------------------------|------------------------|--|---------------------|
| A | 200/PFBT | CF | 120(straight) | 20-55 | 2.41×10 ⁻⁵ | 10 ⁴ | -9.23 |
| B | 200/PFBT | CB | 120(straight) | 20-55 | 4.35×10 ⁻⁶ | 10 ⁴ | -9.59 |
| C | 200/PFBT | CB | RT | 20-55 | 5.01×10 ⁻⁶ | 10 ³ | -6.3 |
| D | 200/PFBT | CB | 120(step anneal) | 20-55 | 1.77×10 ⁻⁵ | 10 ⁴ | -19.8 |

Table 4.1: OFET performance for devices of various configurations fabricated using different solvents

4.3 OFET results for devices fabricated by spincoating from chloroform solutions

The electrical characteristics of a spiro 5T-Ge in figure 4.2 are given for a device ‘A’ measured in N₂ atmosphere. The device operated in the p-channel region and revealed an average charge carrier mobility of 2.41×10⁻⁵cm²/Vs in the saturation regime and on/off ratio is 10⁴.

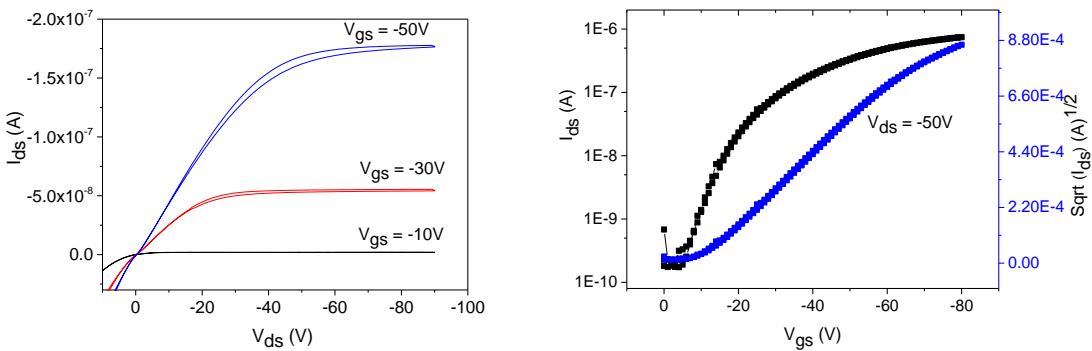


Figure 4.2: Output characteristics (4.2a, left) and transfer characteristics (4.2b, right) of device fabricated by spin-coating 5T-Ge from chloroform on Si/SiO₂ substrates with PFBT treated gold electrode

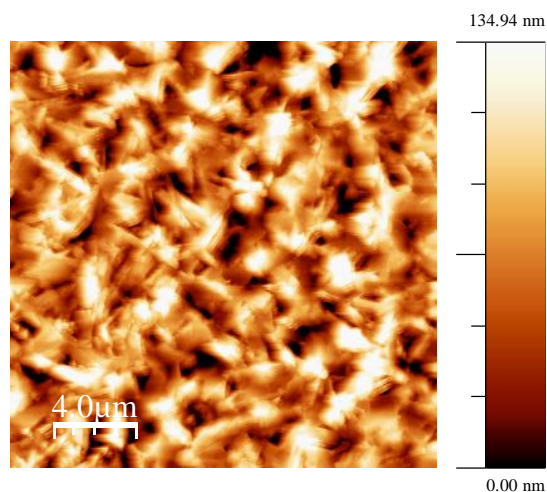


Figure 4.3: AFM image of 5T-Ge film spin cast from chloroform solution on Si/SiO₂ substrate

Figure 4.3 shows an image of 5T-Ge thin film spin coated from chloroform solution which exhibits fibrous crystals with a scatter of grains, the surface roughness value being 32.5nm. This morphology may be induced by the propensity of Ge-cruciform to aggregation due to 2D π - π stacking interactions.

4.4 OFET results for devices fabricated by spincoating from chlorobenzene solutions

Bottom contact FETs were fabricated on substrates consisting of highly doped silicon (the gate electrode), and thermally grown SiO₂ as gate dielectric. Pre-patterned source and drain Au contacts were chemically treated with PFBT prior to film deposition to improve crystallization and charge injection. The organic semiconductor (5T-Ge) is dissolved in CB and deposited on these substrates using spin coating method. The output characteristics of a device annealed straight at 120°C 'B' are depicted in figure 4.4a for several source-gate (V_{gs}) voltages and indicates that hole transport is characteristic for this material when Au contacts are used. The transfer characteristic

of the device at $V_{ds} = -50V$ is shown on the figure 4.4b. The on/off ratio of 10^4 was estimated using semi-logarithmic plot (left Y axis). The field-effect mobility ($\mu=4.35\times 10^{-6}cm^2/Vs$) was found using the square root plot (right Y axis). In the case of samples annealed straight to $120^\circ C$, the tapping mode AFM height image (figure 4.5a) shows a nice spaghetti-like structure. The rod-like elements of the structure were of $\sim 10\ \mu m$ length and $\sim 1\ \mu m$ width with the rms value of 24nm. The horizontal separations between these crystalline rods were as long as $8\ \mu m$ with random alignment. This type of morphology is detrimental for achieving high mobility due to rough domain interfaces and unfavorable alignment of these domains to the direction of the electric field. This observation was further confirmed with thin film XRD graph shown in the figure 4.5b and that compared with 5T-Ge single crystal structure. From X-ray analysis Ge-5T crystals show two dimensional stacking structures with pi-stacking interplanar distance of 3.417\AA in one direction and 3.704\AA in another.⁷³

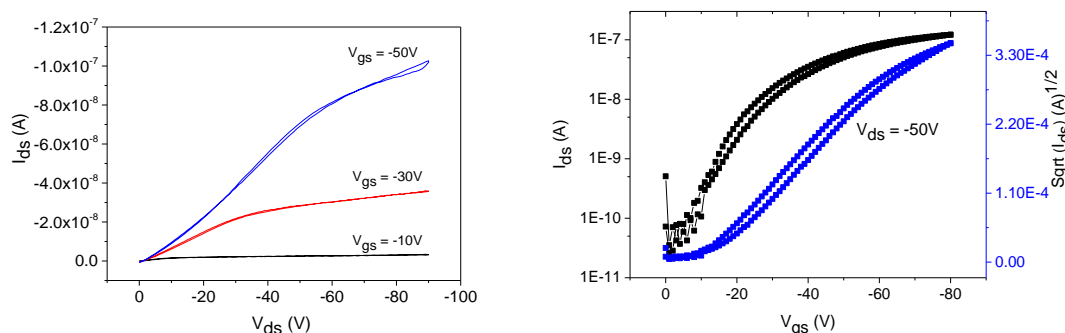


Figure 4.4: Output characteristics (4.4a, left) and transfer characteristics (4.4b right) of OFET fabricated by spincoating 5T-Ge from chlorobenzene solution on PFBT treated gold electrode containing Si/SiO₂ substrates

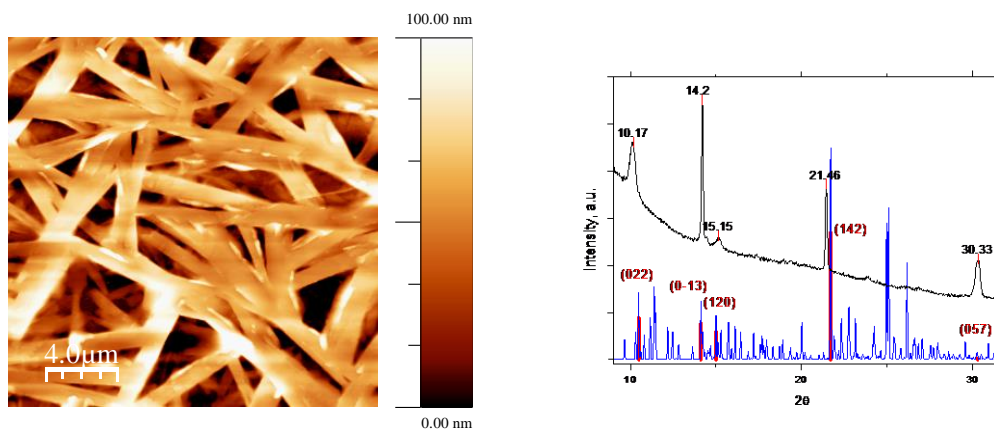


Figure 4.5: AFM image (4.5a, left) of 5T-Ge film spin-cast from chlorobenzene solution on Si/SiO₂ substrate and annealed straight at 120°C; (4.5b, right) OFET device XRD pattern of crystalline 5T-Ge film (black line) compared with that calculated from single crystal X-ray data (blue line) and separate reflexes (red bars with hkl indices marked above by red font) the 2θ value of which coincide with the maxima positions of experimental pattern (shown in black font)

The right panel of figure 4.5 shows the experimental XRD pattern of the film (black line), along with that calculated from the crystal structure (blue line). Red bars represent reflections with marked hkl indices, the 2θ values of which more or less coincide with the experimental XRD peak values. In order to study further the correlation between morphology and charge transport, we compared the OFET performance of devices step-annealed at 50°C, 75°C, 100°C and up to 120°C, to those annealed straight at 120°C for 20 minutes.

4.5 Dependence of OFET performance on annealing temperature (chlorobenzene)

Field effect transistor mobilities were measured in BG/BC configurations and FET characteristics were recorded on annealed samples. Figure 4.6 shows output and transfer characteristics of non-annealed devices whereas figure 4.7 shows an electrical characteristics of samples after being step annealed (each step) at 50, 75, 100 and

finally 120°C for 20 minutes. The effect of contact resistance on the output characteristics of samples annealed straight at 120°C (fig. 4.4a) is stronger than that of samples step-annealed up to 120°C (fig. 4.7a). It can be clearly seen that mobility increases 3.5 times moving from $5.01 \times 10^{-6} \text{ cm}^2/\text{Vs}$ for non-annealed (device 'C') up to $1.77 \times 10^{-5} \text{ cm}^2/\text{Vs}$ after being step-annealed up to 120°C (device 'D'). Meanwhile, the samples annealed straight at 120°C exhibited much lower mobility ($4.35 \times 10^{-6} \text{ cm}^2/\text{Vs}$) compared to that of step-annealed devices. However, for all fabrication conditions, the on/off current ratio remains quite high indicating the overall good quality of all transistors. Although organic semiconducting materials have been known for exhibiting improved performance after annealing closer to their glass transition temperature,²¹⁹⁻²²¹ 5T-Ge appears to show lower mobility.

It is well known that annealing can have a pronounced influence on the morphology of organic thin films. Therefore, we investigated the effect of annealing on the crystallinity of 5T-Ge cruciform. Tapping mode AFM (figure 4.8) appears to be amorphous surface morphology of as cast film. The samples step annealed at 50°C and higher up to 100°C reveal similar crystalline structures⁷⁴. However, the rms surface roughness of samples subsequently annealed at 75 and 100°C is almost double (2.2nm and 2.3nm) compared to that of samples annealed at 50°C and RT (1.5 and 1nm).

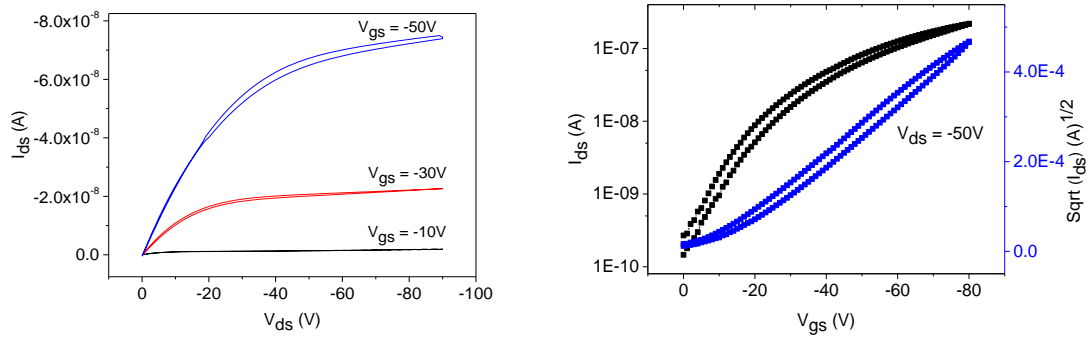


Figure 4.6: Output characteristics (4.6a, left) and transfer characteristics (4.6b, right) of OFET fabricated by spin-coating 5T-Ge from chlorobenzene solution on Si/SiO₂ substrates with PFBT treated gold electrodes without any annealing.

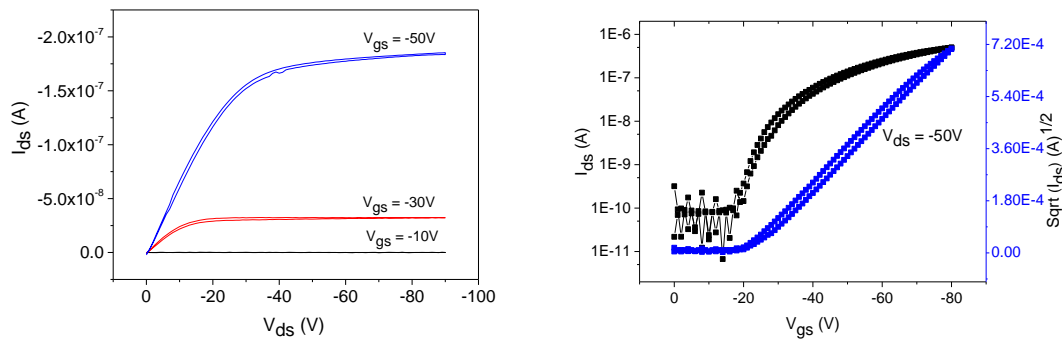


Figure 4.7: Output characteristics (4.7a, left) and transfer characteristics (4.7b, right) of OFET fabricated by spin-coating 5T-Ge from chlorobenzene solution on Si/SiO₂ substrates with PFBT treated gold electrodes after being step-annealing from to 120°C in 20 minutes steps.

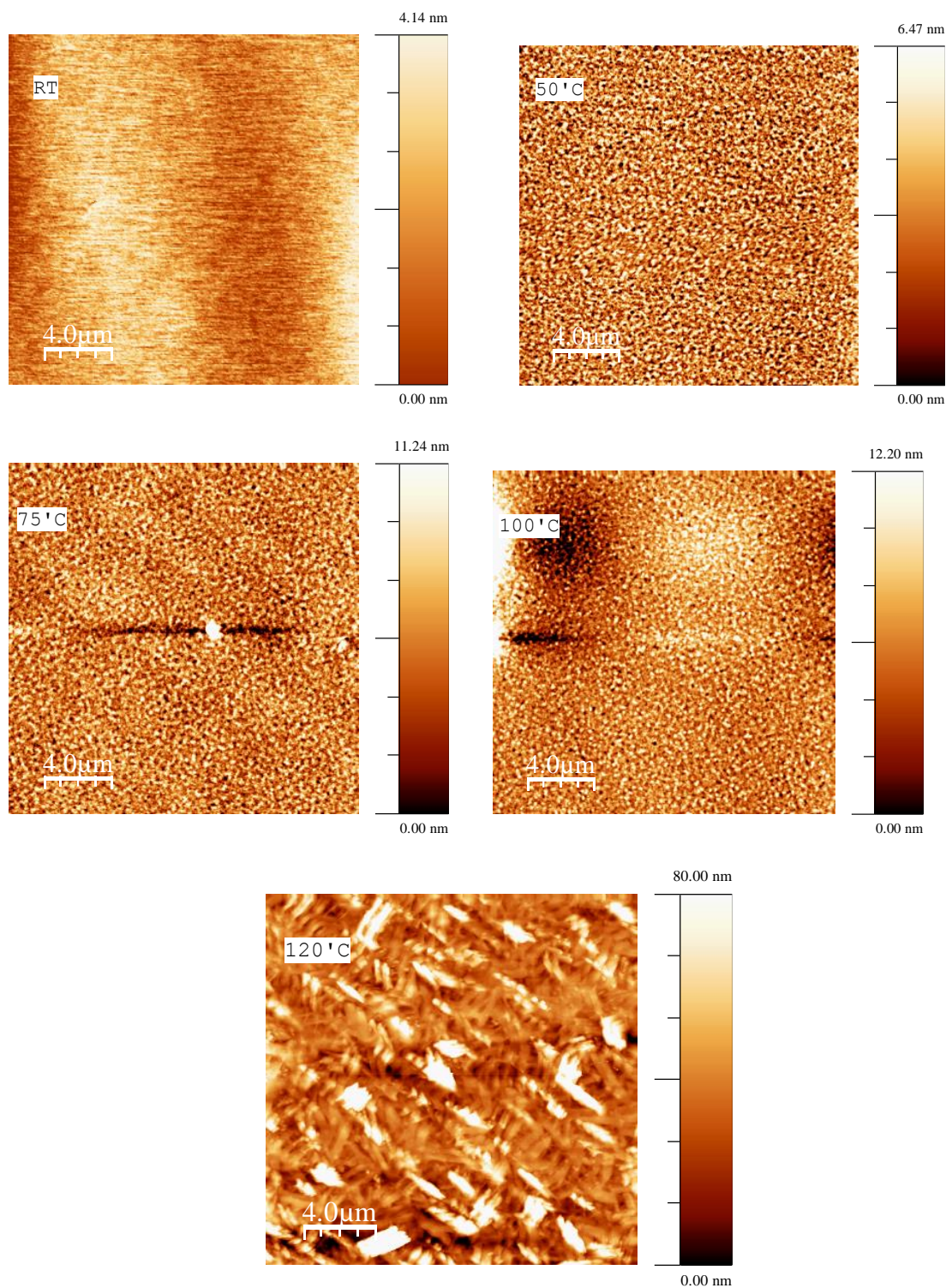


Figure 4.8: Tapping mode AFM images of Ge-cruciform annealed at 120°C for 20 minutes after subsequent annealing at 50, 75, 100°C for 20 minutes

Annealing of the same samples further at 120°C for 20 minutes produces broken rod-like crystalline domains of ~200 nm length and 20nm width (figure 4.8). The rms value for the step-annealing device at 120°C is 14nm meanwhile the device annealed straight at 120°C from chlorobenzene (fig: 4.5) is 24nm. Annealing the samples at 120°C might have given all the molecules similar relatively elevated molecular mobility so that they can form thermodynamically stable aggregates, resulting in the long spaghetti-like structures shown in figure 4.5a.

In contrast, successive step-annealing and cooling up to 120°C might have reduced the molecular mobility due to the formation of smaller crystals at temperatures lower than 100°C. Once the temperatures are further raised to 120°C, the crystalline structures already formed at 100°C may block movements of mobile molecules to form a dense shorter range ordered (DSRO) medium. Nevertheless, this type of DSRO medium would be favorable for any type of electronic devices based on charge transport, such as solar cells or OFETs. A significant variation in morphology due to different annealing protocols is very interesting and may play an important role in device performance. This indicates that the charge transport pathways in directions parallel to the substrate plane are greatly enhanced by successive annealing and cooling. Here we show for the Ge-cruciform that step-annealing leads to the formation of smaller crystalline domains which favor isotropic transport compared to those annealed directly to the final temperature, where we see the formation of larger crystalline spaghetti-like structures which are not favorable for charge transport. Therefore, the introduction of the spiro center between two identical moieties creates a great variety of morphologies which can be achieved by applying different annealing techniques and strongly improves the morphological stability of the corresponding thin films.

4.6 Conclusions

The highest hole mobility of $2.41 \times 10^{-5} \text{cm}^2/\text{Vs}$ for the Ge cruciform semiconductor was found for OFET devices fabricated by spin-coating from chloroform and annealed at 120°C . Applying different annealing protocols (stepwise or straight) for OFET spin-coated from CB a great variety of semiconductor film morphologies has been achieved which provide different device performance. Spaghetti-like crystalline morphology was produced by single annealing at 120°C , while stepwise thermal treatment at 50°C , 75°C , and 100°C and finally at 120°C leads to tight grain packing morphology which proved to be beneficial for OFET performance. The control over morphology by different annealing procedures is provided by the strong propensity of Ge-cruciform to form aggregates, due to 2D π - π stacking interaction in the crystalline domains.

Chapter 5

OFET and morphological characterisation of DPP-fluorene based oligomer

5.1 Abstract

The organic semiconductor on the basis of a quadrupolar linear conjugated system (DPP Linear-c), that consists of 1,4-diketopyrrolo[3,4-c]pyrrole (DPP) central unit and two quarterfluorenylphenyl arms at 3 and 6 position of DPP, is described. The strong propensity of DPP Linear-c to aggregate in the solid favours hole mobility of the semiconductor due to alignment of different molecule's HOMOs in the aggregates. In this chapter, the fabrication of OFETs from this novel p-type semiconductor with different dielectrics, to evaluate their effect on the overall device performance, is reported.

5.2 Introduction

Fluorene is a cyclic aromatic hydrocarbon found in an engine exhaust (Chart 5.1). Fluorene has long been known for the intense violet fluorescence, after which it was named as fluorene.²²² Fluorene based conjugated oligomers can emit deep blue light at an efficiency of up to 99% in solution and 90% in neat solid films,²²³ which is rare in this spectral region. The effect of alkyl substituents at fluorene 9-position is also remarkable, as these groups are almost orthogonal to the plane of the molecule's π -conjugated system. This allows a fluorene compound's solubility and aggregation behaviour to be modulated independently of its electronic properties.²²⁴ These properties have been exploited extensively in polyfluorenes that have grown to be a major material in organic electronics and photonics,²²⁵⁻²²⁷ exhibiting blue electroluminescence,²²⁸ impressive lasing gain,²²⁹⁻²³¹ and promising performance in organic solar cells.²³²⁻²³⁴ The field of organic electronics has also seen a growing focus on oligomer materials,²³⁵ with sizes and properties intermediate between small molecules and polymers.²³⁶ Having a well-defined structure, these monodisperse systems are the perfect object for studying structure/property relationships²³⁷⁻²³⁹ and exhibit higher field-effect mobilities,^{140, 240, 241} and better lasing efficiency²⁴²⁻²⁴⁴ than their polymeric analogues.

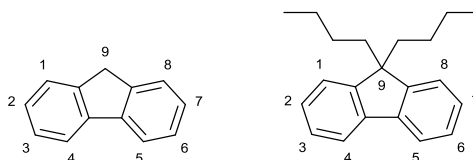
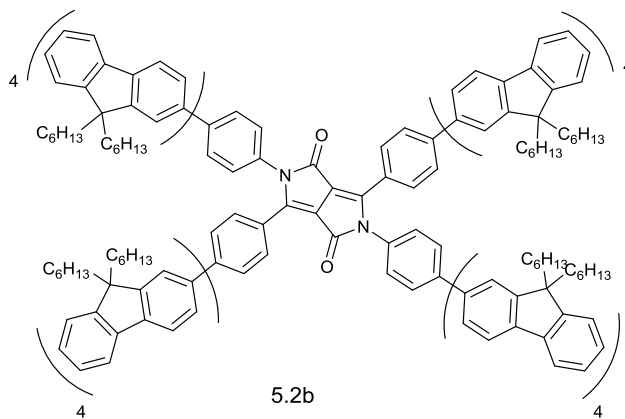


Chart 5.1: An illustration of the fluorene structure showing numbering of sites available for substitution, and alkyl groups at 9-position

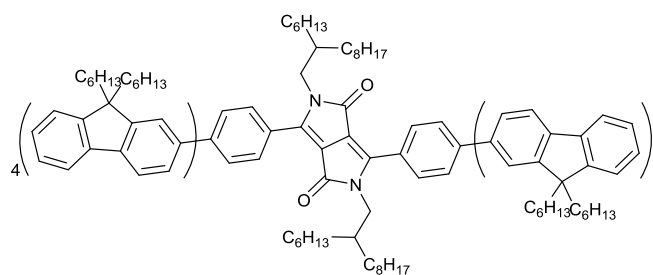
Moreover, oligomers are generally devoid of chain folds²⁴⁵ and chain defects²⁴⁶ that tend to compromise polymer performance. Even though, the synthesis of long oligomers becomes harder in comparison to that of polymers; the more rigorous purification techniques available to oligomers are advantageous for practical applications.²⁴⁷ Oligofluorene's LUMO and HOMO energy levels are slightly further apart than those of polyfluorenes because of the shorter conjugation lengths and larger band gaps.²⁴⁸ A study by Wegner et al reveals that the oligomer length dependence of its properties approaches that of the analogous polymer.²⁴⁹ These unique properties of oligomers make them an ideal complement to conjugated polymers in organic electronics and photonics. This chapter initially focuses on some of the monodisperse fluorene based conjugated oligomers as examples, to assess their performance. Included herein are examples that contain acceptor units such as diketopyrrolopyrrole (DPP) and fluorene donor units in their backbone structures referred as D/A conjugated systems, with potential applications to organic electronics and photonics. DPP-fluorene based compounds synthesized by Yi Qu et al are shown to be colorimetric and ratiometric red fluorescent sensors for fluoride anions with high sensitivity and selectivity.²⁵⁰ The mechanism of the sensing was explained by the intermolecular proton transfer (IPT) process between the amide moiety and fluoride ion and the change of the former from electronically neutral (Ar-DPP(NH)-Ar) without a fluoride ion to negatively charged (Ar-DPP(N⁻)-Ar) with a fluoride ion (Chart 5.2a). The modulation in the electron-donating capabilities of the lactam group in the presence and absence of fluoride directly influences the internal charge transfer (ICT) from the nitrogen lone pair to the conjugated system of the sensors.



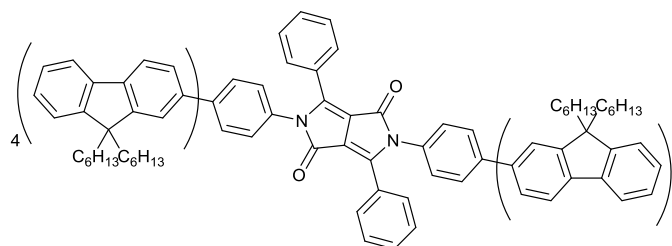
5.2a



5.2b



5.2c



5.2d

Chart 5.2: a) DPP-fluorene based compound for fluoride sensing alongside with quaterfluorene-DPP conjugated systems b) Star DPP c) DPP Linear-c d) DPP Linear-nc

In the presence of fluoride ion, de-protonation of the amide moiety and consequent formation of the amide anion enhance the ICT effect from non-substituted lactam unit to the electron-deficient conjugated system causing a dramatic change in colour and fluorescence of the compounds. This type of fluoride sensing is one of the examples of using an NH-containing receptor for molecular recognition of nucleophilic anions.²⁵¹ The DPP unit has been incorporated into conjugated materials that have been studied as components in solar cells²⁵² and as efficient light emitters.²⁵³ Using electro-polymerisation technique tetraaryl substituted DPP has been incorporated into cross-linked polymers, featuring conjugation paths both in 2,5 and 3,6-directions of DPP.²⁵⁴ Recently, the well-defined star-shaped macromolecular compound with DPP core and the four quarterfluorene arms has been synthesised.⁷⁵ The arms located in the 3,6-positions are conjugated through the core but the arms in the 2,5-positions act independently because the conjugation is disrupted at the lactam nitrogen (fig: 5.2b).

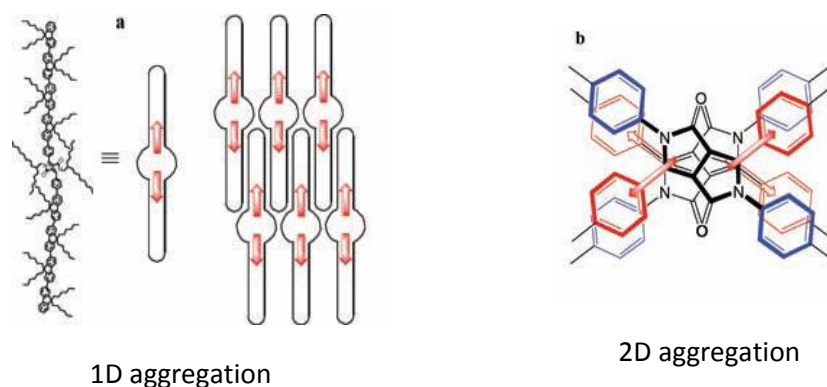


Chart 5.3: Schematic representation of a) 1D and b) 2D interactions between molecules in DPP aggregates.

Twofold substitution of the core with quarterfluorenes is represented by Linear-c (chart 5.2c) and Linear-nc (chart 5.2d), the terminology here refers to the conjugated

pathway, which effectively propagates throughout the central part of the molecule in the former and is mostly restricted to quarter-fluorenyl phenylenes in the latter. The DPP Linear-c features the linear conjugated system with more pronounced quadrupole moment compared to DPP Linear-nc due to better coupling of quaterfluorenylphenyl donor and DPP acceptor units. The crystallinity of DPP Linear-c was assumed to be a result of quadrupole-quadrupole interactions in the condensed phase, which lead to the alignment of the quadrupoles in one direction as shown in chart 5.3a. Star DPP was found to aggregate even in hexane solutions which was explained by intermolecular interactions between more electron rich phenylene rings located in the 2,5-positions and the electron deficient ones in the 3,6-positions leading to alignment of the quadrupole ellipsoids in different directions (2D aggregation, chart 5.3b). This type of intermolecular interaction is favoured by the conformational change around the DPP core.

In the isolated molecule the 3-Ph-DPP-6-Ph fragment remains planar, and in the aggregated state the tetraphenyl-DPP core adopts a propeller-like conformation in which all four phenyl rings are twisted equally. Furthermore, the hydrophobic interactions between the solubilising alkyl chains hinder the longitudinal displacement of adjacent Star-DPP molecules, assisting aggregation in hexane.⁷⁵ DPP Linear-nc presents a similar pattern to Star DPP in the condensed state due to the 2D aggregation, but to a lesser extent, because the initial lower degree of ICT in this conjugated system and the linear shape of the molecule do not provide such strong intermolecular interactions as in the case of Star DPP. Due to 1-D aggregation of Linear-c (figure 5.3a) the quarterfluorene arms of different molecules in the aggregate become really close to each other in the solid state, which increases the probability of electron

hopping from the HOMO of one of the molecules to the SOMO of the cation radical of another. This situation is favourable for increasing hole mobility within the domain of molecules aggregated in such a way. With this in mind the Linear-c has been tried as organic semiconductor for OFET. The electrochemical HOMO-LUMO gap of this compound was reported to be 2.3eV. The HOMO and LUMO levels were observed at -5.4 and -3.1eV respectively.⁷⁵ OFETs were fabricated with different dielectrics to evaluate their effect on overall device performance of DPP Linear-c (chart 5.2c). The representative output and transfer electrical characteristics of devices A, B, C and D with the channel length of 10 μm and the width of 1cm and with different surface treatments (ODTS and HMDS) are compared. In each case the devices with identical geometry (BG/BC) were fabricated and measured to extract electrical parameters such as μ , V_{th} and $I_{\text{on}}/I_{\text{off}}$ which are summarized in Table 5.1.

| Devices | Dielectric (nm)/Au/SiO ₂ modifying agent | Solvents used | V _{gs} interval range, V | μ , cm ² /Vs | I _{on} /I _{off} at V _{ds} of -50V | V _{th} , V |
|---------|---|---------------|-----------------------------------|-----------------------------|--|---------------------|
| A | 200/PFBT | CF | 20-50 | 1.77x10 ⁻⁴ | 10 ⁴ | -19.2 |
| B | 200/PFBT | CB | 20-55 | 7.54x10 ⁻⁵ | 10 ⁵ | -14.0 |
| C | 200/PFBT/ODTS | CF | 20-50 | 5.56x10 ⁻⁵ | 10 ⁵ | -16.7 |
| D | 200/PFBT/HMDS | CF | 20-50 | 1.91x10 ⁻⁴ | 10 ⁵ | -10.4 |

Table 5.1: The electrical performance of DPP Linear-c OFET devices using various dielectrics

5.3 OFET results for DPP Linear-c compound

Figure 5.1 shows the output and transfer characteristics of the device fabricated using PFBT Au treated source/drain electrodes and untreated SiO₂ dielectric. With the PFBT treated source/drain electrodes, significant hysteresis in the drain current can be

observed when comparing the forward and backward voltage scans in transfer characteristics for all these devices.

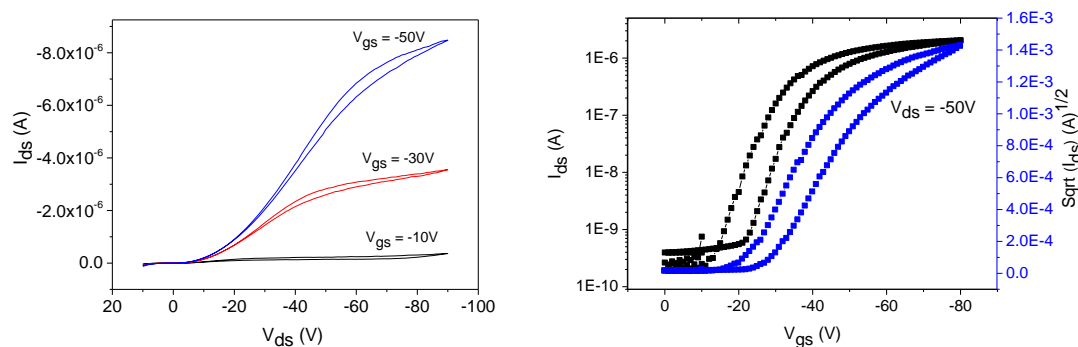


Figure 5.1: Output characteristics (5.1a, left) and transfer characteristics (5.1b, right) of the device fabricated by spincoating of DPP Linear-c from chloroform solution on PFBT treated gold electrode annealed at 140°C for half an hour

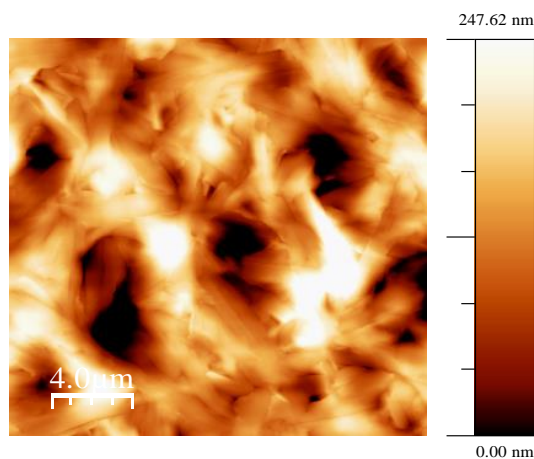


Figure 5.2: Tapping mode AFM images of DPP Linear-c thin film spin cast from chloroform solution on SiO_2 substrate after annealing at 140°C for half an hour.

This effect is also revealed in the transfer characteristics as well. This non-ideality is an indication of an increase in the current in a forward scan due to charge trapping in the semiconductor and the decrease in the current due to charge release in the backward scan. The trap sites might be associated either with chemical impurities in the semiconductor layer, introduced during device processing or morphological structure

of semiconductor/dielectric interface. From the transfer characteristics, (5.1b) a threshold voltage of 19.2V and a charge carrier mobility of about $1.77 \times 10^{-4} \text{ cm}^2/\text{Vs}$ are derived in the saturation regime, with the on/off ratio being 10^4 . Since the interchain interactions should strongly impact on the charge transport properties, we investigated the microscopic morphology of DPP/fluorene oligomer thin film. Figure 5.2 shows the microscopic morphology of a thin film of DPP Linear-c oligomer. The AFM image shows disordered aggregates that are a few hundreds of nm wide and few tens of nm high (bright objects), on the SiO_2 substrate (dark). The rms value of 58nm was calculated for device ‘A’.

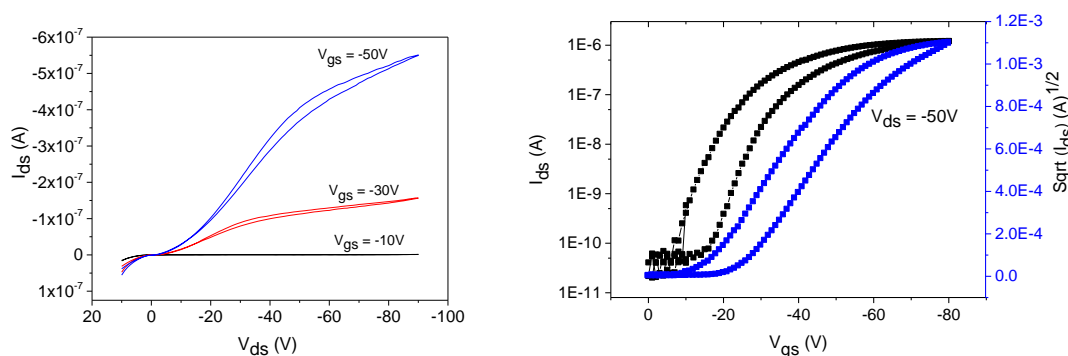


Figure 5.3: Output characteristics (5.3a, left) and transfer characteristics (5.3b, right) of devices fabricated by spin-coating of DPP Linear-c from chlorobenzene solution on Si/SiO₂ substrates with PFBT treated gold electrode

Figure 5.3 shows the output and transfer characteristics of OFET fabricated by spin-coating of DPP/oligofluorene from CB solution. The field effect mobility estimated in the saturation regime shows the value of $7.54 \times 10^{-5} \text{ cm}^2/\text{Vs}$ which is lower compared to the previous case of device ‘A’. However, the on/off ratio of devices fabricated with chlorobenzene and annealed at 140°C increased up to 10^5 . The corresponding AFM

image of thin film spin-cast from chlorobenzene solution is shown in figure 5.4. The AFM image of the film surface shows an uneven morphology with some nanorod like crystalline domains. The surface has an rms roughness of 46 nm which is a little bit decreased compared to the film spun from chloroform (shown above in figure 5.2). To provide better substrate coverage by hydrophobic organic semiconductor and avoid pinhole in the films we next used SAM treatment of the gate dielectric. The effect of the dielectric surface on device performance was investigated.

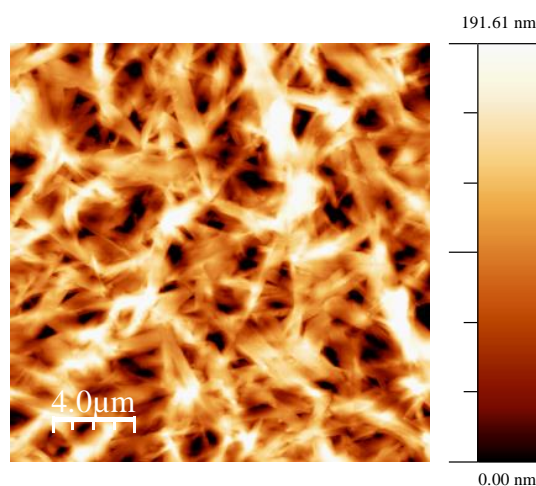


Figure 5.4: Tapping mode AFM images of DPP Linear-c thin film spin-cast from chlorobenzene solution on SiO₂ substrate and annealed at 140°C for half an hour.

5.4 Effect of ODTS and HMDS treatment of SiO₂ substrates on device performance of OFETs with DPP Linear-c as an active layer:

Representative output and transfer curves for ODTS treated Si/SiO₂ devices are shown in figure 5.5. The FET mobility of the thermally annealed devices at 140°C is found to be $5.56 \times 10^{-5} \text{ cm}^2/\text{Vs}$, with an average on/off ratio of 10^5 . Although the film quality was better than that for non-treated substrates, we could not observe any reasonable

transistor behaviour without hysteresis. Since a decrease in mobility was observed for device spin-coated on ODTS treated SiO₂ substrates, compared to that for device cast on untreated SiO₂ surface, the HMDS treatment has been chosen for the surface modification instead. General FET studies from many researchers reveals that HMDS treatment removes residual water and polar groups on SiO₂, leading to an increase in field-effect mobility.²⁵²

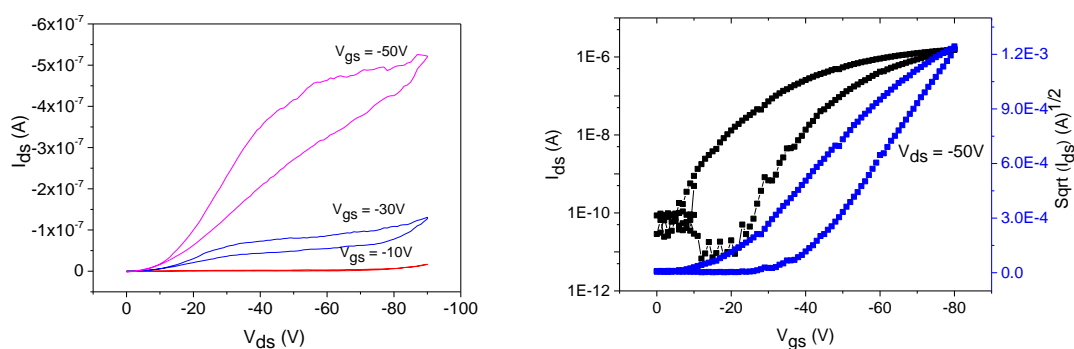


Figure 5.5: Output characteristics (5.5a, left) and transfer characteristics (5.5b, right) of OFET fabricated by spin-coating of DPP Linear-c from chloroform solution on PFBT and ODTS treated Si/SiO₂ substrates and annealed at 140°C

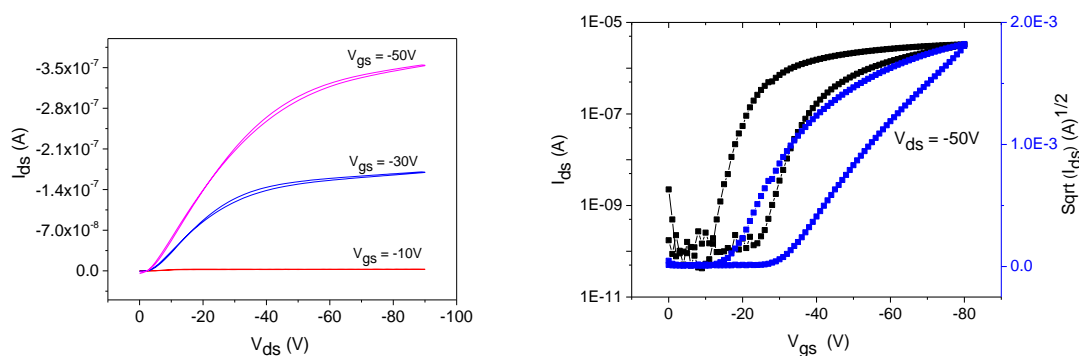


Figure 5.6: Output characteristics (5.6a, left) and transfer characteristics (5.6b, right) of OFET fabricated by spin-coating of DPP Linear-c from chloroform solution on PFBT and HMDS treated Si/SiO₂ substrates and annealed at 140°C

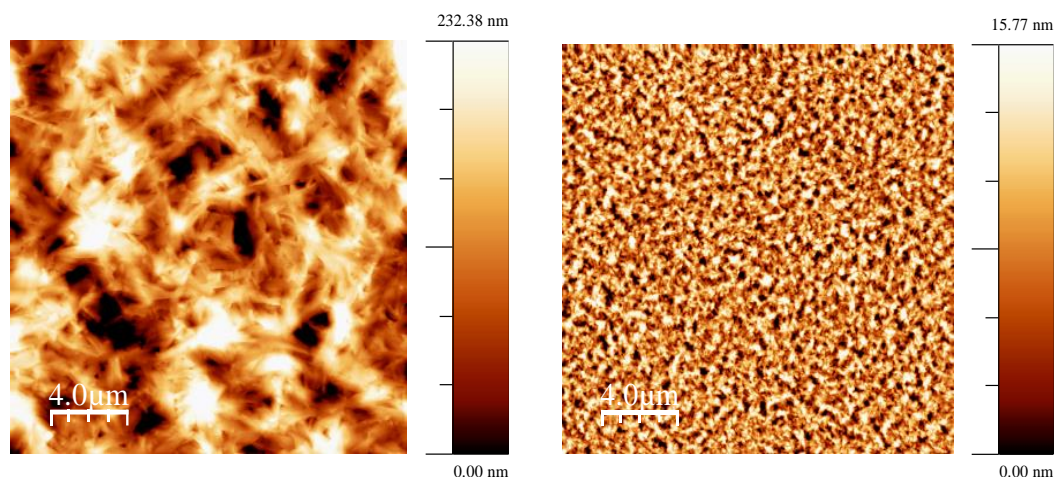


Figure 5.7: Tapping mode AFM image of DPP Linear-c film spin-cast from chloroform solution on ODTS modified SiO₂ substrate (5.7a, left) and on HMDS modified SiO₂ substrate (5.7b, right), after being annealed at 140 °C for half an hour.

Consistently, the FETs fabricated on HMDS treated substrates showed reasonable increase in mobility compared to those with ODTS treated dielectrics with almost no hysteresis in output characteristics. Figure 5.6 shows the output and transfer characteristics of DPP/oligo-fluorene employed FET using BG/BC configuration with HMDS modified substrates. This device exhibits mobility of $1.91 \times 10^{-4} \text{ cm}^2/\text{Vs}$ with a high on/off ratio of 10^5 . Due to the combined effects of PFBT and HMDS treatment the highest mobility has been observed with no significant hysteresis in output characteristics. Figure 5.7 shows the surface morphology of thin films on ODTS (left) and HMDS (right) treated substrates. The film spin-coated on ODTS treated substrate (device ‘C’) exhibits quite rough surface morphology with the rms value of 55.5nm which is very similar to that of device ‘A’ (rms of 58nm). The strong hydrophobic interactions between octadecyl chains of ODTS treated surface and Linear-c alkyl chains lead to non-homogeneous distribution of small crystalline domains along the surface of substrate. Besides, non-favourable orientation of ordered domain due to

these hydrophobic interactions in the case of device 'C' is responsible for more than threefold drop of mobility in comparison to device 'A'. On the contrary, methyl groups of HMDS treated SiO₂ surface are just enough to provide homogeneous distribution of the smaller crystalline domains (rms value of 3.78nm) all over the substrates which yields slightly improved mobility of device 'D' compared to device 'A'.

5.5 Conclusions

In conclusion, we have demonstrated a p-type semiconductor material DPP Linear-c. The morphology and its effect on field effect mobility were studied using various dielectric surface treatments. At annealing temperature of 140°C the fibre domains were formed, which gave the highest mobility. ODTS and HMDS were used to modify the SiO₂ surface. The morphology of DPP Linear-c layer was different for each surface treatment. Larger crystalline structures were observed for films spin-coated on non-treated and ODTS treated SiO₂ substrate whereas film spin cast on HMDS treated surface revealed small domains distributed homogeneously all over substrate which led to the best performing OFETs with a maximum mobility of $1.91 \times 10^{-4} \text{ cm}^2/\text{Vs}$ and a high on/off ratio of 10^5 .

Chapter 6

Synthesis and characterisation of perfluorobenzene based novel organic semiconductors

6.1 Abstract

Chapter six focuses on (1) the synthesis and characterization of thiophene perfluorophenylene based materials for organic field effect transistors (OFET) and (2) the optimization of OFET device fabrication. Charge transport properties of thiophene based semiconductor are expected to be modified by incorporation of perfluorinated phenylene units. By the introduction of electron-withdrawing fluorine substituents, the energies of unoccupied orbitals can be lowered, making n-type charge transport channels possible, however, most of the organic semiconductors have been found to be p-type semiconductors. The electron-rich (donor)/electron-deficient (acceptor) intermolecular interactions sufficiently promote molecular π - π overlap which improves electronic properties of materials and make them attractive for OFET application. The presence of non-covalent interactions between thiophene and perfluorophenylene units also results in planar structures and improves their conjugation. Self-assembly and planarization of thienyl-perfluorophenyl oligomers in the solid state are identified by a combination of x-ray diffraction studies, absorption spectroscopy, and cyclic voltammetry. The x-ray diffraction data show that these materials exhibit flip stacking and thiophene-fluorine molecular interactions. We discuss OFET results with respect to the corresponding morphology determined by AFM and X-ray diffraction measurements.

6.2 Introduction

π - Conjugated halogen substituted organic materials are prone to self-assemble into well-ordered thin films and have significant potential for OFET application. The electronic structure of this type of organic semiconductor has a great influence on the charge transport mobility in thin films, and electron transports (n-type) is facilitated by a low energy barrier to the injection of electrons. This has been attributed to the halogens which lower both the highest occupied molecular orbital (HOMO) and the lowest unoccupied molecular orbital (LUMO) energy levels in the molecule or polymer.²⁵⁵

Fluorinated organic molecules exhibit series of features such as thermal and oxidative stability, enhanced hydrophobicity and high lipophobicity. Amongst the electronegative substituent (-F, -CN, -Cl, -NO₂, -C=O, etc.)²⁵⁶, according to their van der Waals radii, fluorine is the smallest one, $r=1.35 \text{ \AA}$, and larger than hydrogen by only 0.15 \AA . The aforementioned features of fluoroorganic compounds are related to the unique properties of the fluorine atom to be the most electronegative element, with a Pauling electronegativity of 4.0.²⁵⁷ The use of fluorine substituted organic semiconductor molecules in a p-type channel is counterintuitive because fluorine substitution typically transform a p-type semiconductor to an n-type semiconductor.⁵⁹ Stabilization of LUMO energy level results in an increase of electron affinity, that appears to be an important feature for enhancing the electron charge carrier mobility (n-type).^{258,259} Thus, it is easier for the LUMO level to accept electrons and therefore the material will have electron carrier instead of hole carriers. Additionally, these fluorine atoms often have an influence on inter and intramolecular interactions by

forming non-covalent C----F, F----F and C-F...H, C-F...S bonding which in turn results in planar structures in the solid state.⁸⁰ Thus, the introduction of fluorine into conjugated organic compounds allow for the energy gap of materials to be modified with significant impact on optical and electrical properties. Therefore, substitution with fluorine atoms can be used to generate organic p-type, n-type or even ambipolar semiconducting materials with improved stability.

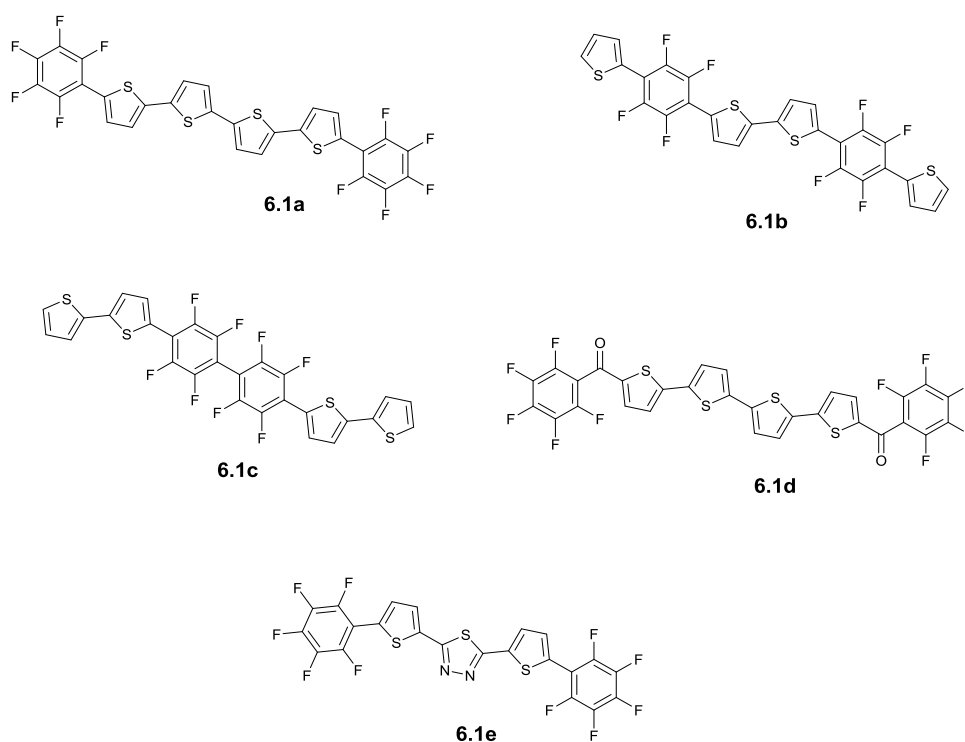


Chart 6.1: List of oligomers 6.1a-6.1e

The organic semiconductors (**6.1a-e**), displayed in table 6.1 have been synthesized and tested for OFET applications. Some of them showing remarkable n-type characteristics in OFETs, others maintaining the p-type character and exhibiting enhanced environmental stability.²⁶⁰ The oligomer compounds **6.1a-c**, synthesized by Antonio Fchetti⁷⁹, via Stille or Suzuki cross-coupling reactions, exhibit regiochemically modulated semiconducting behaviour. Due to the different position of the

perfluorinated arene units in the conjugated backbone the systems **6.1a** and **6.1b** show higher mobility than compound **6.1c**. Oligomers **6.1a** and **6.1b** exhibit n and p type character, respectively, whereas none of these two shows ambipolar charge carrier properties. Both compounds form π - π stacking in the solid state. Due to limited twisting of the arene-thiophene units the compounds **6.1a** and **6.1b** display planar configuration of the conjugated backbone whereas, compound **6.1c**, containing the two consecutive perfluorophenylene units, has considerably higher torsional angle. For p-type materials, the HOMO levels are typically -4.9–5.5eV, while for n-type materials the LUMO levels are normally at -3–4eV. In the case of compounds **6.1a-b** efficient charge transport is attributed to the extended pi-system with strong intermolecular overlaps.²⁸

| Oligomers | E _{LUMO} [eV] | | E _{HOMO} [eV] | | Band gap, eV | μ cm ² /Vs | I _{on} /I _{off} value |
|-------------|------------------------|-------|------------------------|-------|---------------------|---------------------------|---|
| | THF | FILM | THF | FILM | | | |
| 6.1a | -2.85 | -2.69 | -5.48 | -5.27 | 2.58 | 0.08 (n) | >10 ⁵ |
| 6.1b | -2.82 | -2.67 | -5.64 | -5.32 | 2.65 | 0.01 (p) | 10 ⁵ |
| 6.1c | -2.81 | -2.53 | -5.81 | -5.40 | 2.87 | 4X10 ⁻⁵ (p) | 10 ² |
| 6.1d | -3.59 | - | -5.99 | - | 2.40 (<i>opt</i>) | 0.45 (n) | 10 ⁸ |
| 6.1e | -2.96, <i>DCM</i> | - | - | - | 2.96 (<i>opt</i>) | - | - |

Table 6.1: HOMO and LUMO levels, mobility (μ), and band gap values for compounds 6.1a-e.

In particular, the oligomer **6.1a** is found to be n-type semiconductor, demonstrating that fluoroarene end group promotes charge carrier sign inversion, independent of the thiophene core extension. Interestingly, this compound with the LUMO values of -2.85eV and -2.69eV for solution (THF) and film respectively showed electron

mobility of $0.08\text{cm}^2/\text{Vs}$ and $I_{\text{on}}/I_{\text{off}}$ value of 10^8 . Due to higher electron affinity, the low lying LUMO level was observed, which is likely responsible for the n-type conductivity of the compound **6.1a**.²⁶¹ A narrow band gap of 2.58eV was found for this compound. Compound **6.1b** exhibits hole mobility of $0.01\text{cm}^2/\text{Vs}$ with current on/off ratio of 10^4 and the band gap of 2.65eV . Moreover in a film, E_{LUMO} values are maintained in a narrower range of -2.69 and -2.67 for materials **6.1a** and **6.1b** respectively. The perfluoroaryl rings of both compounds contribute more significantly to the LUMO, as expected when compared to compound **6.1c**. Oligomer **6.1c** showed significantly lower hole mobility of $4 \times 10^{-5}\text{cm}^2/\text{Vs}$ with on/off ratio of 10^2 . The LUMO level of -2.53eV was observed but not sufficiently low for electron charge injection, in compound **6.1c**.⁷⁹ Simply switching to perfluorobenzoyl substitution by Friedel-Crafts acylation followed by Stille coupling reaction resulted an n-type semiconducting oligothiophene **6.1d** synthesized by J.A. Letizia.²⁶²

When applying a positive gate voltage the material **6.1d** shows excellent OFET performance as n type semiconductor.^{28, 261, 263} This compound reveals the HOMO level of -5.99eV with a very low-lying LUMO level of -3.59eV . UV-Vis absorption in THF indicates that the optical band gap (E_g) is 2.40eV . Due to the strong electron withdrawing resonance effect of perfluorobenzoyl group, LUMO level was decreased enough to provide high electron mobility, $\mu = 0.45 \pm 0.07\text{cm}^2/\text{Vs}$ for OFET fabricated by vapour deposition film with $I_{\text{on}}/I_{\text{off}}$ value of 10^8 .²⁶² Thiadiazole based oligomer **6.1e**, synthesized via formation of hydrazone followed by sulphur insertion and attaching perfluorophenyl units by Stille coupling reaction, was characterized using electrochemistry (ΔE_{elec}) and absorption spectroscopy (ΔE_{opt}). However, no oxidation

waves were observed for the electron deficient thiadiazole **6.1e** as a consequence of enhanced stabilization of the HOMO level. An increased optical band gap of 2.96V, LUMO level of -2.96V and two reduction waves at -1.48V and -1.71V were exhibited by this compound.

6.3 Results and discussion

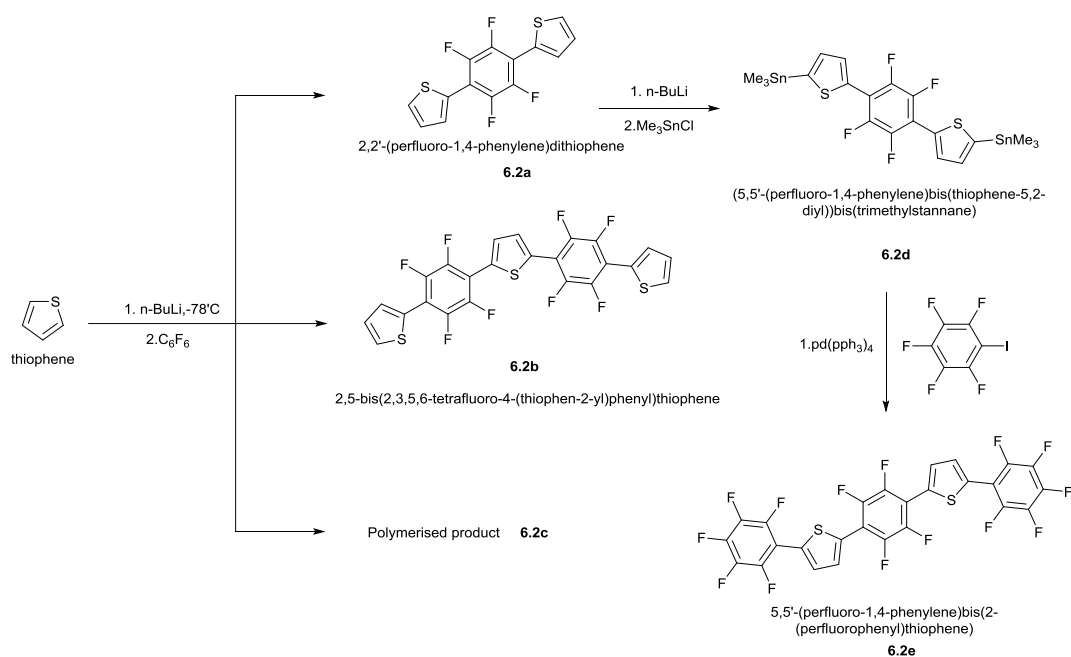


Chart 6.2: Synthesis of the compounds 2,5-bis(2,3,5,6-tetrafluoro-4-(thiophen-2-yl)phenyl)thiophene (**6.2b**) and 5,5'-(perfluoro-1,4-phenylene)bis(2-(perfluorophenyl)thiophene) (**6.2e**)

Following the previous results obtained in Prof Skabara group^{16, 261, 264}, thiophene oligomers bearing perfluorophenylene core (i.e., fluorinated phenylene units) have been synthesized as potential organic semiconductor materials especially for organic field-effect transistors (OFETs). Progressing with this project, the compounds were synthesized according to the chart 6.2. Initially, thiophene was lithiated at -78°C followed by addition of hexafluorobenzene to the reaction mixture, which produced a

very exothermic reaction. In other words, the lithiation of thiophene involved a deprotonation step, and reaction with hexafluorobenzene involved nucleophilic substitution reaction at the aromatic center (S_NAr reaction). The reaction between thiophenyl lithium species and hexafluorobenzene had been known to produce 2, 2'-(perfluoro-1, 4-phenylene) dithiophene **6.2a** as the sole product¹⁶, more detailed examination of this reaction allowed us to isolate another product of this reaction, previously unknown, 2,5-bis(2,3,5, 6-tetrafluoro-4-(thiophen-2-yl) phenyl) thiophene **6.2b** and indicated that the yield of the initial target compound **6.2a** is lowered by formation both compound **6.2b** and polymeric species **6.2c** due to possible lithiation of thiophene on both α -positions. To diminish the effect of this route on the yield of the target compound **6.2a** the reaction was attempted using a large excess of thiophene. Even at high ratio of thiophene to BuLi (5:1 equivalents) it was not possible to avoid formation of compounds **6.2b** and **6.2c** by suppression of lithiation on the other α -position of thiophene, probably due to higher acidity of compound **6.2a** compared to unsubstituted thiophene. The polymer **6.2c** was separated by filtration. Column chromatography was performed to separate the mixture of compounds **6.2a** and **6.2b** with hexane as eluent. The reaction conditions were varied, and the procedure was optimized to achieve the maximum yield of both compounds **6.2a** and **6.2b**.

The following step consisted of introducing trimethyltin group in the compound **6.2a**. This was achieved by lithiation of the compound **6.2a** with two equivalent of n-BuLi at -78°C , followed by quenching with trimethyltin chloride, which afforded ((perfluoro-1,4-phenylene)bis(thiophene-5,2-diyl))bis(trimethylstannane)²⁶⁵, **6.2d**. By microwave acceleration, the stannylated product was then coupled with

iodopentafluorobenzene via Stille coupling reaction using as the tetrakis (triphenylphosphine) palladium (0) catalyst at 120°C, in THF solution. The yield of the target molecule, 5,5'-(perfluoro-1,4-phenylene)bis(2-(perfluorophenyl)thiophene) **6.2e**, was 15%. Attempts to improve the yield by changing the solvent to DMF, dioxane; altering the temperature of the reaction were unsuccessful.²⁶⁶

6.4 UV-Vis and CV spectra of the organic semiconductors **6.2b** and **6.2e**

Optical absorption and emission spectra of 2,5-bis(2,3,5,6-tetrafluoro-4-(thiophen-2-yl)phenyl)thiophene, **6.2b** and 5,5'-(perfluoro-1,4-phenylene)bis(2-(perfluorophenyl)thiophene, **6.2e** were measured. The absorption spectrum of compound **6.2b**, figure 6.1, shows π - π^* transition with a maximum λ_{abs} at 359 nm.

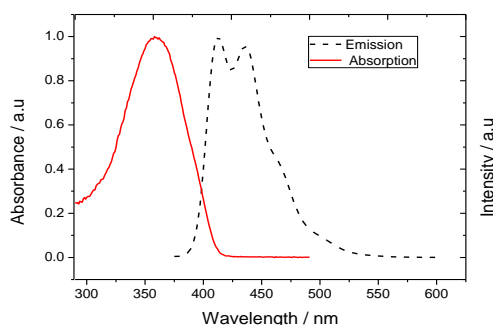


Figure 6.1: Absorption and emission spectra of 2,5-bis (2,3,5, and 6-tetrafluoro-4-(thiophen-2-yl)phenyl)thiophene (**6.2b**) measured in CH₂Cl₂

The splitting of the band in the emission spectrum due to vibrational coupling shows two peaks at 413 and 435 nm. From the onset of red edge of absorption, optical band gap for compound **6.2b** was calculated to be 3.00eV. The cyclic voltammetry of compound **6.2b** was performed in dichloromethane (figure 6.2). This compound

exhibits HOMO/LUMO level of $-6.02/-2.85\text{eV}$ with electrochemical band gap of 3.17eV .

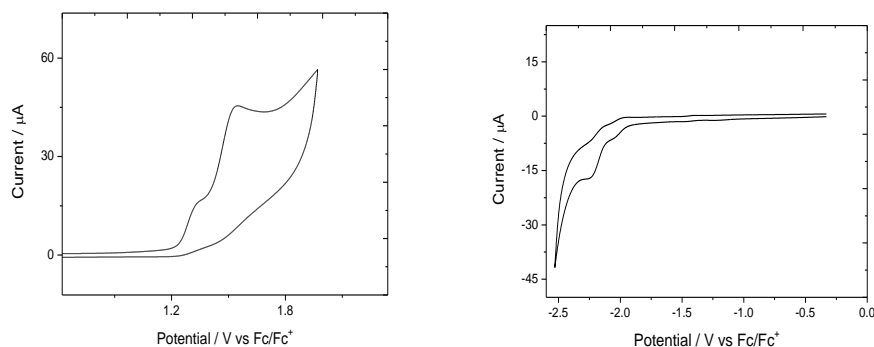


Figure 6.2: Monomer oxidation (left) and reduction (right) of ca. 9.9×10^{-5} M CH_2Cl_2 solution of 2,5-bis(2,3,5,6-tetrafluoro-4-(thiophen-2-yl)phenyl) thiophene (6.2b), on a glassy carbon working electrode, with an Ag wire reference electrode, Pt counter electrode, , 0.1 M TBAPF₆ as supporting electrolyte, at a scan rate of 100mVs^{-1} . The data is referenced to the Fc/Fc⁺ redox couple.

The oxidation process of compound 6.2b shows two irreversible peaks at +1.34 and +1.55V related to the sequential removal of two electrons from the thiophene units with formation of a radical cation and dication respectively. The reduction process shows irreversible peak at -2.24V , from addition of electrons to tetrafluorobenzene units of this compound. The absorption and emission spectrum of compound 6.2e are displayed in figure 6.3. The absorption maximum at 353 nm is hypsochromically shifted by ~ 6 nm compared to that of 6.2b due to the greater steric effect of fluorine atoms. The emission spectrum showed two peaks at 406 and 428 nm. The optical band gap was determined to be 3eV.

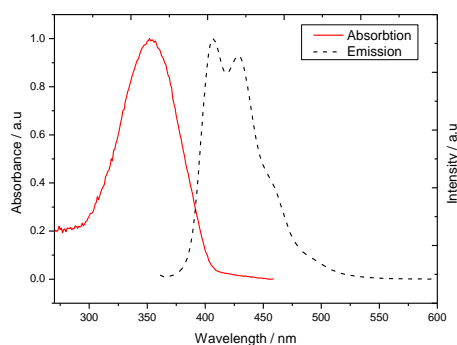


Figure 6.3: Absorption and emission spectra of 5,5'-(perfluoro-1,4-phenylene) bis(2-(perfluorophenyl)thiophene) (6.2e) measured in CH₂Cl₂ respectively

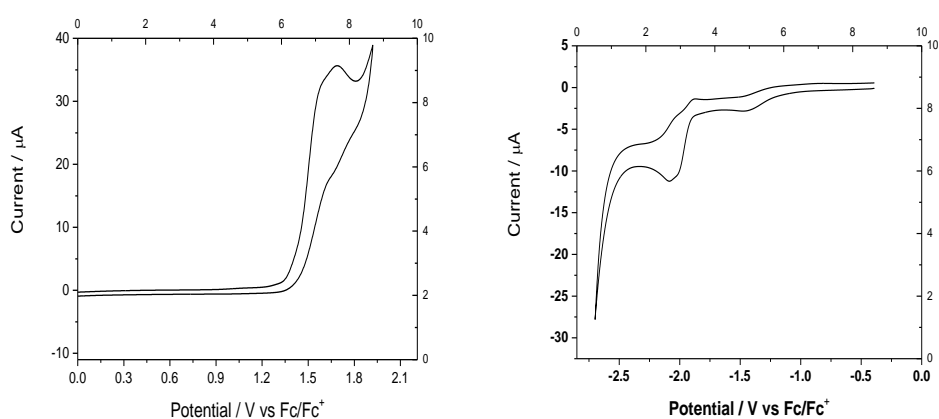


Figure 6.4: Oxidation (left) and reduction (right) of the compound 6.2e (ca. 10⁻⁴ M in CH₂Cl₂) on a glassy carbon working electrode, with Ag wire reference electrode, Pt counter electrode, 0.1 M TBAPF₆ as supporting electrolyte at a scan rate of 100mVs⁻¹. The data is referenced to the Fc/Fc⁺ redox couple.

| | Onset of Oxidation, V | Onset of Reduction, V | HOMO, eV | LUMO, eV | Electrochemical band gap, eV | Optical band gap, eV |
|-------------|-----------------------|-----------------------|----------|----------|------------------------------|----------------------|
| 6.2b | +1.22 | -1.95 | -6.02 | -2.85 | 3.17 | 3.00 |
| 6.2e | +1.41 | -1.91 | -6.21 | -2.89 | 3.32 | 3.00 |

Table 6.2: Representation of oxidation/reduction onsets, HOMO-LUMO, and band gap values for compounds 6.2b and 6.2e

On cyclic voltammogram of compound **6.2e** the irreversible oxidation (+1.66V) and reduction (-2.0V) peaks were observed (Figure 6.4). The lower electrochemical band

gap for **6.2b** is probably attributed to the more destabilised HOMO due to the presence of three thiophene donor units compared to two ones in **6.2e**. The low optical band gap for both compounds (**6.2b** and **6.2e**) compared to corresponding electrochemical band gap attributed to the formation of excitons upon photoexcitation. The larger Stokes shifts compared to reported thiophene-perfluorobenzene system (5,5'-bis(perfluorophenyl)-2,2'-bithiophene)²⁶⁷ observed for both compounds could be explained by more planar geometry of **6.2b** and **6.2e** in the excited state. Results from cyclic voltammetry indicate that **6.2b** has a lower ionization potential, while **6.2e** shows a little bit higher electron affinity than **6.2b**. Trends from the optical absorption and emission parameters of both fluorinated compounds can be directly correlated to electrical performances in field effect devices. Collection of UV-Vis and CV data are listed in table in 6.2.

6.5 Atomic Force Microscopy and crystal data

To evaluate the potential of these (**6.2b** and **6.2e**) compounds as organic semiconductor materials, attempts were made to fabricate OFETs using evaporation methods on bare Si/SiO₂ substrates. There was no FET transistor behaviour observed for either compounds. The solution process technique was tried for fabrication of OFETs. Thin films of compound **6.2b** and **6.2e**, were spin-coated as an active layer from chlorobenzene on Si/SiO₂ substrates. The films, however, afforded morphologies for both compounds, which did not support OFETs. Several attempts to form thin films by varying solvent and spin coating rate invariably afforded larger crystals. In case of compound **6.2b**, AFM shows the presence of distinct domains in thin film of **6.2b** (fig. 6.5A) and section analysis of the sample revealed that the step heights between domain

levels measured between 2.5 and 3.0 nm. In the case of compound **6.2e**, (fig. 6.5B) bulk crystals were randomly observed and once again not suitable for field effect transistors. Hence, this observation indicates the necessity of optimizing chemical components along with the device fabrication procedure optimization, such as spin coating conditions. Subsequently, a study on combining, or blending, two small compounds (**6.2b** and **6.2e**) has been employed to form nano-structured tuned film. This supramolecular approach to fabrication of thin films explores an intermolecular packing in such a way that improves the mobility.

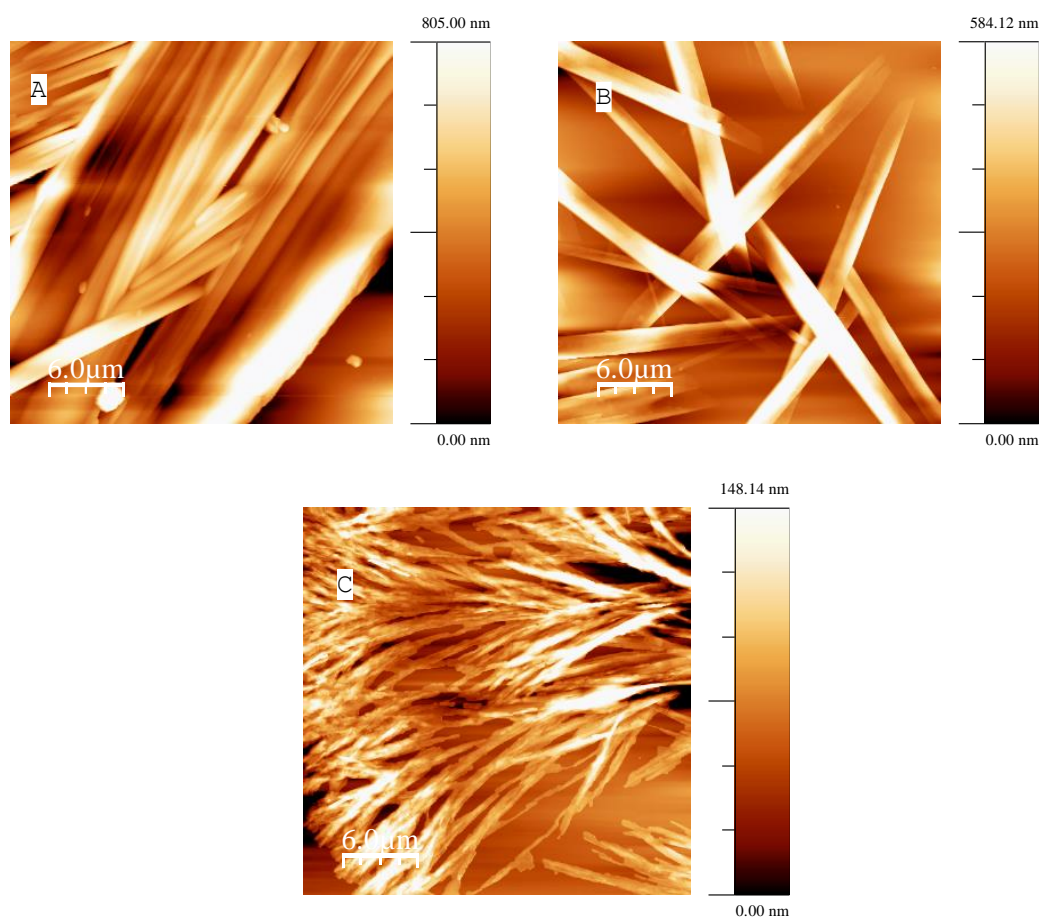


Figure 6.5: Atomic Force Microscopic images of compound 6.2b (A) and 6.2e (B) and blend of two compounds 6.2b and 6.2e (C)

The AFM image (fig. 6.5C) exhibits fibrillar structures confirming that the blend of two compounds has a different morphology. Fabrication of OFETs using compounds **6.2b** and **6.2e** as active layers is currently under progress in the laboratory. To illustrate the intermolecular interactions, we performed the X-ray crystal analysis of compound **6.2b**. As shown in figure 6.6, there are apparent face to face π - π stacking interactions between perfluorobenzene and thiophene with interplanar distance of 3.51 Å, a similar value (3.62 Å) reported for perfluorobenzene system 5,5'-(perfluoro-1,4-phenylene)bis(3-methylselenophene).^{261, 268} In the view of the crystal structure, the compound exhibits almost planar though slightly twisted conformation which might be due to the steric repulsion between the thiophene and perfluorobenzene units.

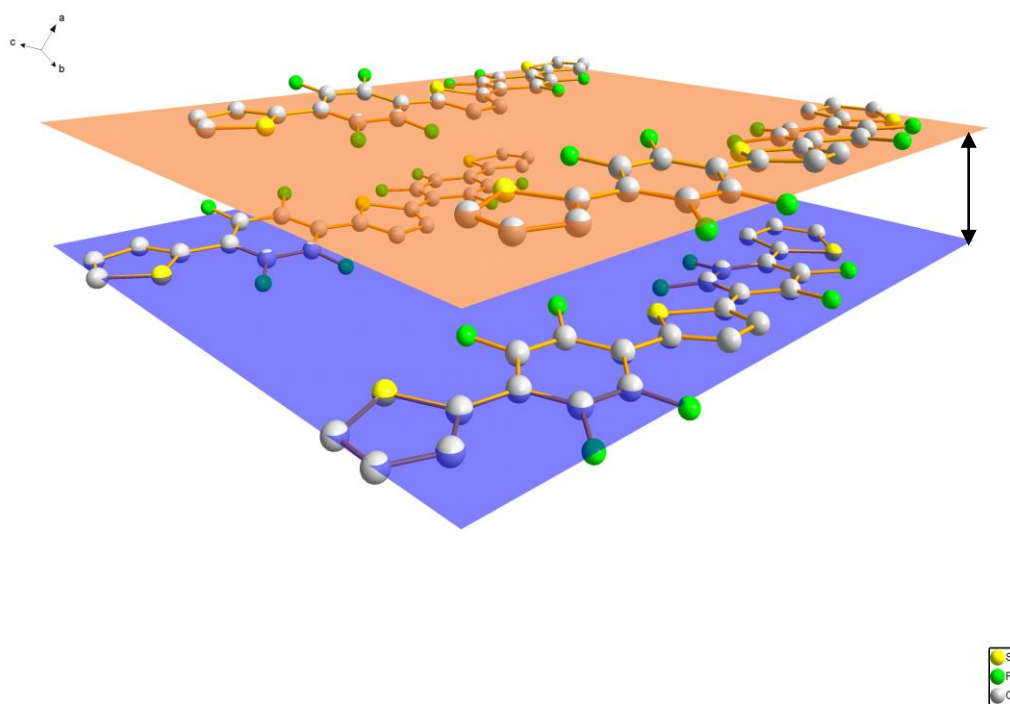


Figure 6.6: Crystal structure and interplanar distance of compound (6.2b) (2,5-bis(2,3,5,6-tetrafluoro-4-(thiophen-2-yl)phenyl) thiophene)

The planarity of the molecule arises from attractive intramolecular S-F interactions (2.74Å)²⁶⁹ and strong F---F interactions (2.57Å). Due to the presence of the aforementioned face to face π - π stacking interactions strong electronic charge transport can be expected. It is clearly seen from the figure 6.7, herringbone packing has been detected in the crystal structure suggests that monomer **6.2b** may work well, as semi-conductor for field effect transistors.^{256, 267, 270}

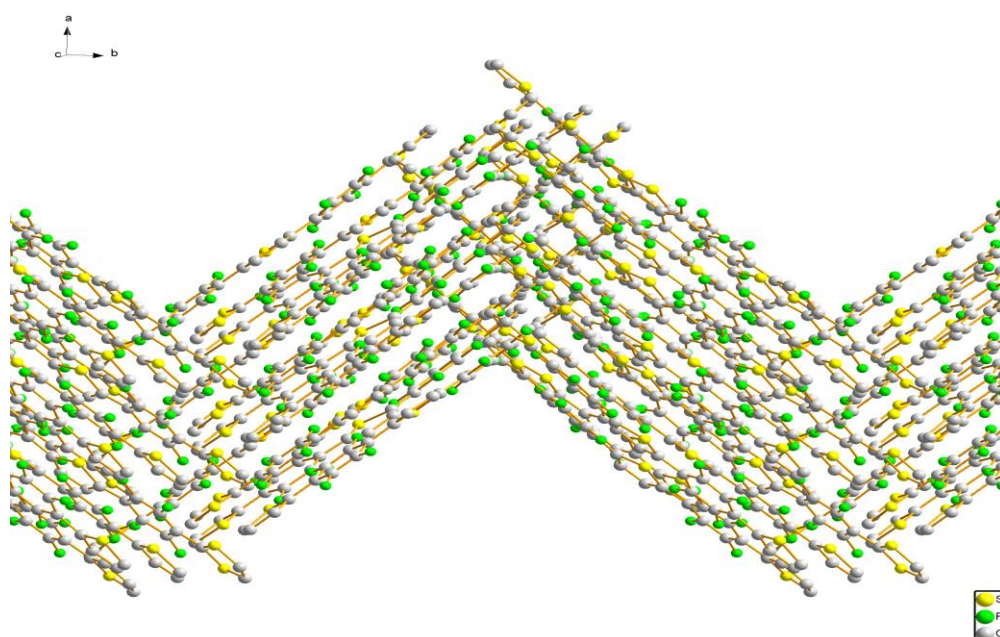


Figure 6.7: π - π Stacking herringbone structure of compound (6.2b) 2,5-bis(2,3,5,6-tetrafluoro-4-(thiophen-2-yl)phenyl)thiophene

6.6 Conclusions

This chapter attempts to give an overview of new semiconductor materials for organic field effect transistors from the viewpoint of synthetic chemistry. In the field of organic

electronics, the instability of the materials and the lack of n-type semiconductor are the two important key issues hindering the commercialization of devices. Through band gap engineering, the LUMO energy level can be decreased with fluorine functionalization that might lead to ambipolar or electron transport. Based on results of this chapter and the studies from other research groups, n-channel materials design include: 1) incorporation of electron withdrawing substituents on π -conjugated frameworks to enhance stability of the materials towards oxidation and decrease their LUMO level to the range of -4.0 to -4.1 eV; 2) introduction of non-covalent interactions leading to structural planarity that increase molecular packing and stabilise doped state. In summary, two donor-acceptor based organic semiconductors have been described. Future work will be focusing on the optimization of these materials for electron-transport applications considering their synthetic accessibility, stability and high device performance.

Chapter 7

Summary and conclusions

The purpose of this thesis was the synthesis and characterisation of a new electron-deficient, potentially n-type, organic semiconductors 6.2b, 6.2e and the study of the behaviour of four p-type organic semiconductors [5T-TTF, 5T-Ge, p(DPP-TTF) and DPP Linear-c]. Even though the two of the latter (p(DPP-TTF) and DPP Linear-c) do contain electron deficient DPP-unit the more spatially extended character of the HOMO make them exclusively p-type materials. The OFETs have been fabricated and their output and transfer characteristics have been analysed. In this work, electrodes and gate dielectric surface were modified by SAM. BG/BC field-effect transistor mobility of $9.56 \times 10^{-3} \text{cm}^2/\text{Vs}$ was exhibited by 5T-TTF film spun onto ODTS (SAM) treated SiO_2 gate dielectric from chloroform solution with the on/off ratio of 10^5 . AFM characterization of the spin coated film reveals crystallinity, with the size of crystalline domain being highly dependent on the solvent used for spin-coating. For p(DPP-TTF) the two geometries of OFETs are investigated. In a bottom-contact, top-gate OFET geometry, combinations of a polymeric organic semiconductor with cyclic fluoropolymer (cytop) dielectric lead to OFET mobility of $5.3 \times 10^{-2} \text{cm}^2/\text{Vs}$ with excellent air stability. The bottom-contact, bottom-gate layout, however, produced the lower performance of mobility than top gate configuration.

Both chapters 2 and 3 discussed the effect of SAMs on the electrode and dielectrics surfaces on device performance due to an improved charge injection and microscopic ordering in the channel of a semiconductor. The choice of the solvents was also important. The results revealed that chloroform was the best solvent for fabricating OFET using 5T-TTF and p(DPP-TTF) as semiconductors due to the solvation energy effect which led a larger domain size of semiconductor film and higher OFET mobility.

The hole mobility of $2.41 \times 10^{-5} \text{cm}^2/\text{Vs}$ for Ge cruciform semiconductor was found for OFET devices fabricated by spin-coating from chloroform. In this work it has been shown that this material has good tendency to crystalize and form crystalline thin films. Two sets of devices have been fabricated changing the annealing temperature regime (straight and stepwise) when chlorobenzene used as a solvent. Spaghetti-like crystalline morphology was produced by single annealing at 120°C , while stepwise thermal treatment led to tight grain packing morphology which proved to be beneficial for OFET performance. By applying different annealing protocols (stepwise or straight) a variety of semiconductor film morphologies has been achieved which provide different device performance. The control over morphology by different annealing procedures is provided by the strong propensity of Ge-cruciform to form aggregates, due to 2D π - π stacking interaction in the crystalline domains. Overall, the best performance for devices fabricated by spin-coating 5T-Ge from CF solution is achieved after stepwise annealing of the thin film up to 120°C using CB solution.

In chapter 5, DPP Linear-c oligomer shows a strong dependence of field-effect mobility on the gate dielectric surface modification, with almost an order of magnitude difference being observed between different dielectrics. From the results obtained from DPP Linear-c, it is found that the field-effect mobility of thin film increases from ODTS treated dielectric surface to oxygen-plasma (OP) treated gate dielectric SiO_2 surface and hexamethyldisilazane (HMDS) treated dielectric surface, from 5.56×10^{-5} to 1.77×10^{-4} and $1.91 \times 10^{-4} \text{cm}^2/\text{Vs}$ respectively. The methyl groups of HMDS treated SiO_2 surface are just enough to provide homogeneous distribution of the crystalline domains all over the substrates, which yields improved mobility of device. Whereas

orientation of domains on ODTs treated SiO₂ surface is not favourable for field effect mobility.

Finally, chapter 6 deals with the synthesis of two novel compounds from the family of perfluorobenzene thiophene small molecules. Introduction of highly electronegative halogen (fluoro) elements onto conjugated backbone molecules enhances electron affinity for n-type semiconductors. Both compounds show optical band gap of 3eV and electrochemical band gap of 3.17eV (6.2b) and 3.32eV (6.2e). Trends from the optical and CV parameters of both fluorinated compounds can be directly correlated to electrical performances in field effect devices. However, morphological studies indicate that both compounds form bulky crystalline domains at every attempt of spin-coating and this is detrimental for field effect transistors. A new approach is on the way to employ mixing these two novel small molecule materials and to produce the semiconductor with improved nano-morphology and field effect mobility. Computational studies and OFET characterisations are also in progress to fully understand this unique class of semiconductors.

In this thesis, BHJ solar cells with two different semiconductors (5T-TTF and DPP-TTF polymer) were fabricated and characterised. Initially, BHJ solar cells using 5T-TTF as a donor material and PC₇₁BM as an acceptor were investigated. Devices using chloroform exhibited a J_{sc} of 7.44mA/cm² and a V_{oc} of 700mV with a fill factor of 0.33 and a PCE value of 1.7%. The further improvement was achieved by using DCB as a solvent, which produced J_{sc} of 9.81mA/cm² and a V_{oc} of 780mV and a fill factor of 0.33 and a PCE value of 2.5%. Secondly, DPP-TTF copolymer donor material was characterised using two different solar cell concepts. D/A blended BHJ solar cell and

a single material organic solar cell (SMOC) were described. The overall efficiency of the BHJ polymer devices exhibited a PCE of 1.8% with V_{oc} of 710mV and J_{sc} of 8mA/cm². SMOC exhibited a power conversion efficiency of 0.3 % with a J_{sc} of 1.8mA/cm² and V_{oc} of 610mV. The results obtained from these materials offer great opportunities to develop systems with interesting energy harvesting properties.

Chapter 8

Experimental section

8.1 OFETs fabrication and characterization

All solvents and SAM reagents were purchased from Sigma Aldrich Ltd., UK. Commercially available (Fraunhofer institute) n-doped silicon chips with 200 ± 10 nm of thermally grown SiO_2 , prefabricated interdigitated Au fingers (50 nm Source/Drain electrodes) having capacitance per unit area of $1.7 \times 10^{-8} \text{ F/cm}^2$ were used as substrates.

8.1.1 5T-TTF oligomer

All OFET devices in the case of 5T-TTF molecule were fabricated using BG/BC configuration. Gold electrodes were treated with 7mM PFBT isopropanol solution for 20 minutes. Insulator surfaces were treated with ODTS or were left untreated. Substrates treated with ODTS were soaked for 30s in a 3 mM ODTS solution in toluene and rinsing with toluene. Both PFBT and ODTS treatment were performed under an ambient atmosphere. SAM modified substrates were then moved into a Nitrogen filled glove box for active layer deposition. Active semiconductor materials were prepared by dissolving 10 mg of 5T-TTF in 1ml of CF and CB separately. The active layers were then deposited on top of SAM treated surface by spincoating method at 800 rpm for 60s and annealed subsequently at 120°C for 20 minutes. In all measurements, we used a channel length (L) of 10 μm and a channel width (W) of 1 cm. The electrical characteristics of the FETs were measured in an inert environment using Keithley 4200 source/measure units. Field effect mobilities and threshold voltages (V_{th}) were calculated in the saturation regime defined by standard FET models by plotting the $\sqrt{I_{\text{ds}}}$ versus V_{gs} data at $V_{\text{ds}} = -50\text{V}$ for all devices using the following equation:

$$\mu_{sat} = \frac{2L}{WC_i} \times \left(\frac{\partial \sqrt{I_{ds}}}{\partial V_g} \right)^2, V_T = \frac{\sqrt{I_0}}{\frac{\partial \sqrt{I_{ds}}}{\partial V_g}} \quad (15)$$

Where I_{ds} is the source drain current, μ is the carrier mobility, $\partial (I_{ds})^{1/2}/\partial V_{gs}$ is the slope and $(I_0)^{1/2}$ is the intercept of the plot. V_g is the gate voltage, L is the channel length, W is the channel width and C_i is the capacitance per unit area of an insulator material. Also extracted from transfer characteristics is the on/off current ratio (I_{on}/I_{off}).

8.1.2 DPP-TTF polymer

Two different types of configurations were used for DPP-TTF OFET fabrication: 1) BG/BC configuration 2) TG/BC configuration

I) BG/BC configuration

Commercially available SiO_2 (insulator) surfaces were soaked for 30s in a 3 mM ODTs solution in toluene and rinsing with toluene while gold electrodes were left untreated. ODTs treatment was performed under an ambient atmosphere. SAM modified substrates were then moved into a Nitrogen filled glove box for active layer deposition. Active semiconductor materials were prepared by dissolving 6 mg of DPP-TTF polymer in 1 ml of CF and CB separately. The active layers were then deposited on top of SAM treated surface by spincoating method at 1000 rpm for 60s and annealed subsequently at 200°C for half an hour. In all measurements, we used a channel length (L) of 10 μm and a channel width (W) of 1 cm. The electrical characteristics of the FETs were measured in an ambient environment using Keithley 4200 source/measure units. Field effect mobilities and threshold voltages (V_{th}) were calculated in the

saturation regime defined by standard FET models by plotting the $\sqrt{I_{ds}}$ versus V_{gs} data at $V_{ds} = -50V$ for all devices using the following equation (15)

II) TG/BC configuration

Gold source and drain electrodes (70 nm) were deposited by high vacuum thermal evaporation on top of the silicon substrate using a shadow mask which provided channel length (L) of 40 μm and a channel width (W) of 1500 μm . Substrates treated with ODTS were soaked for 30s in a 3 mM ODTS solution in toluene and rinsed with toluene. The active layers were then deposited on top of SAM treated surface by spin coating method (1000 rpm) and annealed subsequently at 200°C for half an hour. Cytos was then added and annealed at 100°C for half an hour. These samples were then placed in the evaporator chamber for deposition of aluminium (70nm) gate electrode. The prepared OFETs were then characterised. The electrical characteristics of the FETs were measured using Keithley 4200 source/measure unit. Field effect mobilities and threshold voltages (V_{th}) were calculated in the saturation regime defined by standard FET models by plotting the $\sqrt{I_{ds}}$ versus V_{gs} data at $V_{ds} = -70V$ (CB and CF) for all devices using the following equation (15). The carrier mobility was also calculated in the linear regime from the slope plotting drain current versus gate voltage (V_{gs}) of -15V(CF) and -20V(CB). The calculations in linear regime were done by the following equation (16):

$$\mu_{lin} = \frac{\partial I_{ds,lin}}{\partial V_g} \times \frac{L}{WC_i V_d}, V_T = \frac{I_0}{\frac{\partial I_{ds,lin}}{\partial V_g}} - \frac{V_{gs}}{2} \quad (16)$$

8.1.3 5T-Ge cruciform

To characterize 5T-Ge cruciform, OFET devices were fabricated using BG/BC configuration. Gold electrodes on Si/SiO₂ substrates were treated with 7mM PFBT isopropanol solution for 20 minutes. Insulator surfaces were left untreated. PFBT treatment was performed under an ambient atmosphere. SAM modified substrates were then moved into a Nitrogen filled glove box for active layer deposition. Active semiconductor materials were prepared by dissolving 10mg of 5T-Ge cruciform in 1ml of CF and CB separately. The active layers were then deposited on top of SAM treated surface by spincoating method at 800 rpm for 60s. One set of samples were annealed straight at 120°C for 20 minutes, another set of samples were step-annealed at 50, 75, 100 and 120°C for 20 minutes each. In all measurements, we used a channel length (L) of 10 um and a channel width (W) of 1 cm. The electrical characteristics of the FETs were measured in an inert environment using Keithley 4200 source/measure units. Field effect mobilities and threshold voltages (V_{th}) were calculated in the saturation regime defined by standard FET models by plotting the $\sqrt{I_{ds}}$ versus V_{gs} data at $V_{ds} = -50V$ for all devices using the equation 15.

8.1.4 DPP Linear-c macromolecule

To characterize DPP Linear-c macromolecule, OFET devices were fabricated using BG/BC configuration. Gold electrodes on Si/SiO₂ substrates were treated with 7 mM PFBT isopropanol solution for 20 minutes. Insulator surfaces were treated with *n*-ODTS and hexamethyldisilazane²⁷¹ (HMDS). Substrates treated with ODTs were soaked for 30s in a 3 mM ODTs solution in toluene and rinsed with toluene. Both

PFBT and ODTs treatment were performed under an ambient atmosphere, while substrates treated with HMDS were spun at 3000 rpm/60s to dry before annealing at 100°C for 10 minutes. SAM modified substrates were then moved into a Nitrogen filled glove box for active layer deposition. Active semiconductor materials were prepared by dissolving 30mg of DPP Linear-c in 1ml of CF and CB separately. The active layers were then deposited on top of SAM treated surface by spincoating method at 800 rpm for 60s and subsequently annealed at 140°C for 20 minutes. In all measurements, we used a channel length (L) of 10 μm and a channel width (W) of 1 cm. The electrical characteristics of the FETs were measured in an inert environment using Keithley 4200 source/measure units. Field effect mobilities and threshold voltages (V_{th}) were calculated in the saturation regime defined by standard FET models by plotting the $\sqrt{I_{\text{ds}}}$ versus V_{gs} data at $V_{\text{ds}} = -50\text{V}$ for all devices using the equation 15.

8.2 Solar cell fabrication and characterization

The devices were fabricated with a conventional structure of Glass/ITO/PEDOT–PSS/(D/A)/Ca(40nm)/Al(40nm), using a solution process for depositing hole-collecting layer and donor-acceptor blend. The 100 nm thick layer of ITO coated glass substrates was cleaned by ultrasonic treatment in acetone, and isopropyl alcohol for 5 minutes and dried by a nitrogen flow. A thin hole collecting layer of poly(ethylenedioxythiophene)/poly(styrenesulfonate) (PEDOT/PSS), was spin coated at 4000 rpm on the ITO/glass substrate. After baking at 120°C for 20 minutes, the substrates were transferred into nitrogen-filled glove box and the rest of the OPV device processing and characterisations were carried out in the glove box.

The donor-acceptor (D/A) blend with different ratio were prepared in CF and o-DCB solutions and stirred for 12hrs before spin-coating at 800 rpm. Finally, a 40 nm of calcium and 40 nm of aluminium layer were deposited on the active layer under high vacuum (2×10^{-6} mbar). The effective area of each cell (4 mm x 1.5 mm) was defined by the shadow mask. The current density–voltage (I–V) curves of photovoltaic devices were obtained by a Keithley 4200 source/measure unit. The photocurrent was measured under AM 1.5 (100 mW/cm²) irradiation using a Newport solar simulator, calibrated with a standard Si solar cell. The efficiency of solar cell was calculated by the following equation:

$$\eta_{max} = \frac{V_{OC} \cdot I_{SC} \cdot FF}{P_{in}} \quad (17)$$

Where V_{oc} - Open-circuit voltage, I_{sc} - short circuit current, FF - Fill factor.

8.3 Synthesis

¹H spectra were recorded on a Bruker Avance / DPX400 at 400.13 and 100.61 MHz and Bruker Avance / DRX500 at 500 MHz and 125.75 MHz in CDCl₃; chemical shifts are given in ppm; all J values are in Hz. MS MALDI-TOF spectra were recorded on a Shimadzu Axima-CFR spectrometer (mass range 1-150 000 Da). Elemental analyses were obtained on a PERKIN ELMER 2400 elemental analyser. Melting points were taken using a TA Instruments Q1000 DSC using a heat rate of 10°C/min. UV-Vis absorption spectra were recorded on a UNICAM UV 300 instrument. Baselines of solvents were measured before analysis and solution spectra were recorded in 1 cm path length quartz cells between 190 and 1100 nm. Emission spectra were measured

on a Perkin Elmer LS45 fluorescence spectrometer with excitation at 370 nm. Commercial TLC plates (Silica gel 60 F254) were used for TLC chromatography and column chromatography was carried out on silica gel Zeoprep 60 Hyd (40-63 μm mesh). Solvents were removed using a rotary evaporator (vacuum supplied by low vacuum pump) and, when necessary, a high vacuum pump was used to remove residual solvent. Dry solvents (tetrahydrofuran, hexane, toluene) were obtained from a solvent purification system (SPS 400, innovative technologies) using alumina as the drying agent; any other dry solvent (DMF) were purchased from Aldrich. All reagents and solvents were purchased commercially from Sigma Aldrich. The Crystals were made by the thermal gradient sublimer under the vacuum of 10^{-3} mbar.

8.3.1 Synthesis of 2,2'-(perfluoro-1,4-phenylene)dithiophene (6.2a) and 2,5-bis(2,3,5,6-tetrafluoro-4-(thiophen-2-yl)phenyl)thiophene (6.2b)

Thiophene was dissolved in dry tetrahydrofuran (75ml) and cooled to -78°C under inert nitrogen atmosphere. *N*-Butyl lithium solution was added drop wise, under stirring. After complete addition, the yellow solution was warmed to room temperature over a period of 1 hour followed by the addition of hexafluorobenzene rapidly. The resulting viscous orange solution refluxed for 24 hours. The reaction mixture was allowed to cool to room temperature and diluted with chloroform. The resulting precipitated solution was filtered through sintered crucible leaving a yellow coloured solid of the polymer **6.2c**. The CHCl_3 and THF fractions were concentrated under reduced pressure yielded yellow coloured solid mixture. The thin-layer chromatography technique showed two spots. Using hexane as eluent, the products were separated by column chromatography to give the products of 2,2'-(perfluoro-1,4-

phenylene) dithiophene **6.2a** and 2,5- bis(2,3,5,6-tetrafluoro-4-(thiophen-2-yl)phenyl)thiophene **6.2b**. Table 8.1 summarises different reaction conditions and the ratio of materials used for this reaction. The reaction products are purified by recrystallization from CH₂Cl₂/methanol affording compound **6.2a** as a fine white powder and compound **6.2b** as a yellow solid material. m/z: 544.05, ¹HNMR: 7.23 (2H, dd, ³J=4.8 Hz, ³J=4.0 Hz), 7.59 (2H, d, ³J=4.8 Hz), 7.71 (2H, d, ³J=4.0 Hz), 7.76 (2H, S). The value of elemental analysis calculated for compound **6.2b**: C, 52.94; H, 1.48; S, 17.67 %. Found: C, 53.20; H, 1.32; S, 18.01 %. For the product **6.2a** the obtained data are comparable with the literature.¹⁶

| | THF | Thiophene | n-BuLi | C ₆ F ₆ | Oligomers | M/V | Yield | Polymer (6.2c) |
|---|--------|--|---|---|--------------------------------|--------------------|--------------------|----------------|
| 1 | 50 ml | 2g, 1.9ml, 23.76 mmol (1eq) | At -80°C, 2.10M, 24mmol, 11.42ml (1.01eq) | 1.37ml,(0.5eq) Exothermic was observed | 6.2a | 30mg | 0.8% | 2.28g |
| 2 | 25 ml | 2g, 1.9ml, 23.76 mmol (1eq) | At -80°C, 2.29M, 24mmol, 10.5ml (1.01eq) | 2.21g,(0.5eq) Maintained -30°C Exothermic was observed | 6.2a 6.2b | 600mg 18mg | 16% 0.6% | 2.30g |
| 3 | 50 ml | 4g, 3.8ml, 47.5 mmol (1eq) | At -80°C, 2.21M, 48mmol, 21.7 ml (1.01eq) | 4.42g,(0.5eq) Maintained -30°C Exothermic was observed | 6.2a 6.2b | 1.17g 140mg | 15.6% 2.16% | 2.90g |
| 4 | 100 ml | 10g, 9.17ml (5 eq) <i>[1 eq would be 2g, 1.9ml, 23.76 mmol]</i> | At -80°C, 2.16M, 24mmol, 11.1ml (1.01eq) | 2.21g,(0.5eq) Maintained -30°C Exothermic was not observed. | 6.2a 6.2b | 470mg 350mg | 12.6% 10.8% | 3.33g |
| 5 | 75 ml | 6g, 5.504ml (3 eq) <i>[1 eq would be 2g, 1.9ml, 23.76 mmol]</i> | At -80°C 2.16M, 24 mmol, 9.6ml (1.01eq) | 2.21g,(0.5eq) Maintained at room temperature, Exothermic was observed | 6.2a 6.2b | 640mg 295mg | 17.1% 9.13% | 1.87g |

Table 8.1: Experiments with various ratios of reagents and various reaction conditions

8.3.2 Synthesis of (perfluoro-1,4-phenylene)bis(thiophene-5,2-diyl))bis(trimethylstannane) (6.2d)

A solution of *n*-BuLi (6.01 ml of 2.5 M solution in hexanes, 13.360 mmol) was added drop wise to a stirred at -78°C solution of dry tetrahydrofuran containing the compound **6.2a** (2 g, 6.632 mmol) in 200 ml of THF. The reaction mixture was stirred for 1.5 hours at the same temperature, followed by drop wise addition of 14 ml (13.36 mmol) of Me₃SnCl solution. The resulting reaction mixture was stirred at -78°C for 2 hours. After reaching the room temperature, the reaction mixture was concentrated in vacuum, and the residue was extracted with a CH₂Cl₂ and washed with brine. The organic fractions were dried over Na₂SO₄, and concentrated in vacuum, to yield 3.5g (85%) of compound **6.2d**. ¹HNMR: 0.43 (18H, s), 7.28 (2H, d, J³=3.6 Hz), 7.76 (2H, d, J³=3.2Hz).

8.3.3 Synthesis of 5,5'-(perfluoro-1,4-phenylene)bis(2-(perfluorophenyl)thiophene) (6.2e)

A solution of 0.124 ml (0.938 mmol) of iodopentafluorobenzene, 0.200g (0.313 mmol) of compound **6.2d**, and 5 mg (0.05 mmol) of Pd(PPh₃)₄ in 2.5 ml of anhydrous tetrahydrofuran was stirred at 125°C in a sealed vial (2.5-5ml type) for 12 hours in the microwave, the pressure being maintained at 7 bar. After cooling to room temperature, the precipitate was separated by filtration. After the recrystallization, the yield of the compound **6.2e** was 25mg (15.6%, Melting point: 218°C - 221°C). m/z: 645.90, ¹HNMR: 7.63 (2H, d, ³J=4.0 Hz), 7.77 (2H, d, ³J=4.0Hz).

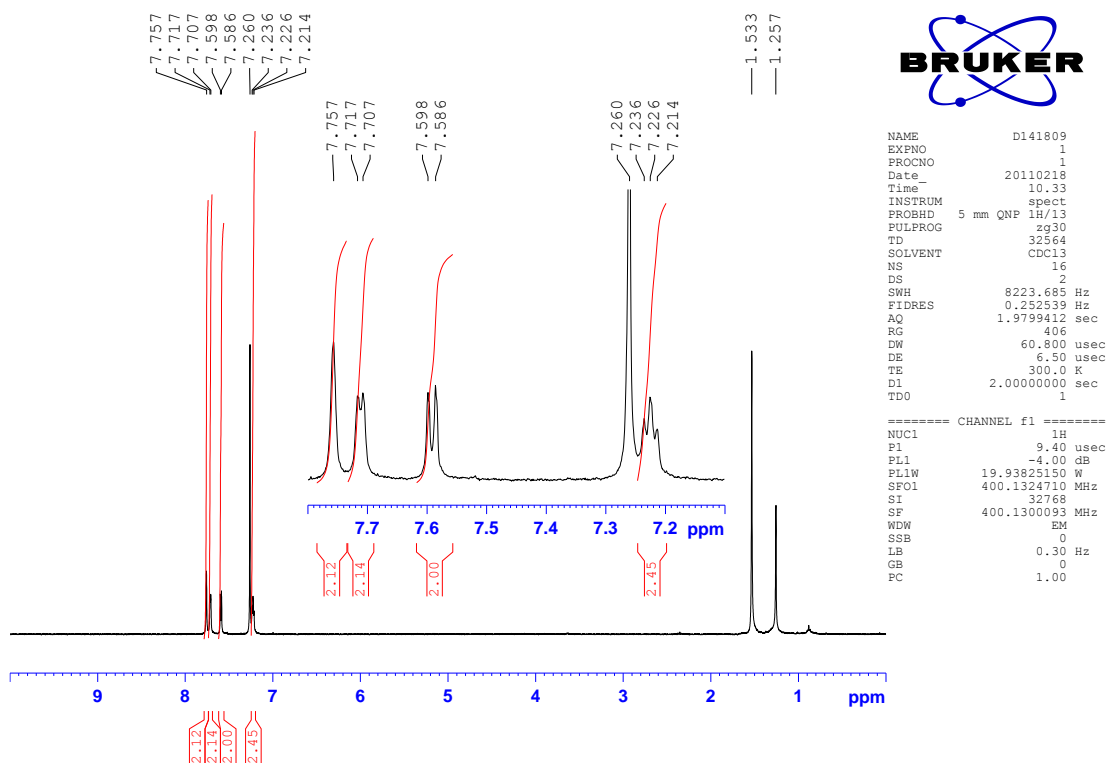


Figure 8.1: ^1H NMR spectrum of 2,5-bis(2,3,5,6-tetrafluoro-4-(thiophen-2-yl)phenyl)thiophene (**6.2b**)

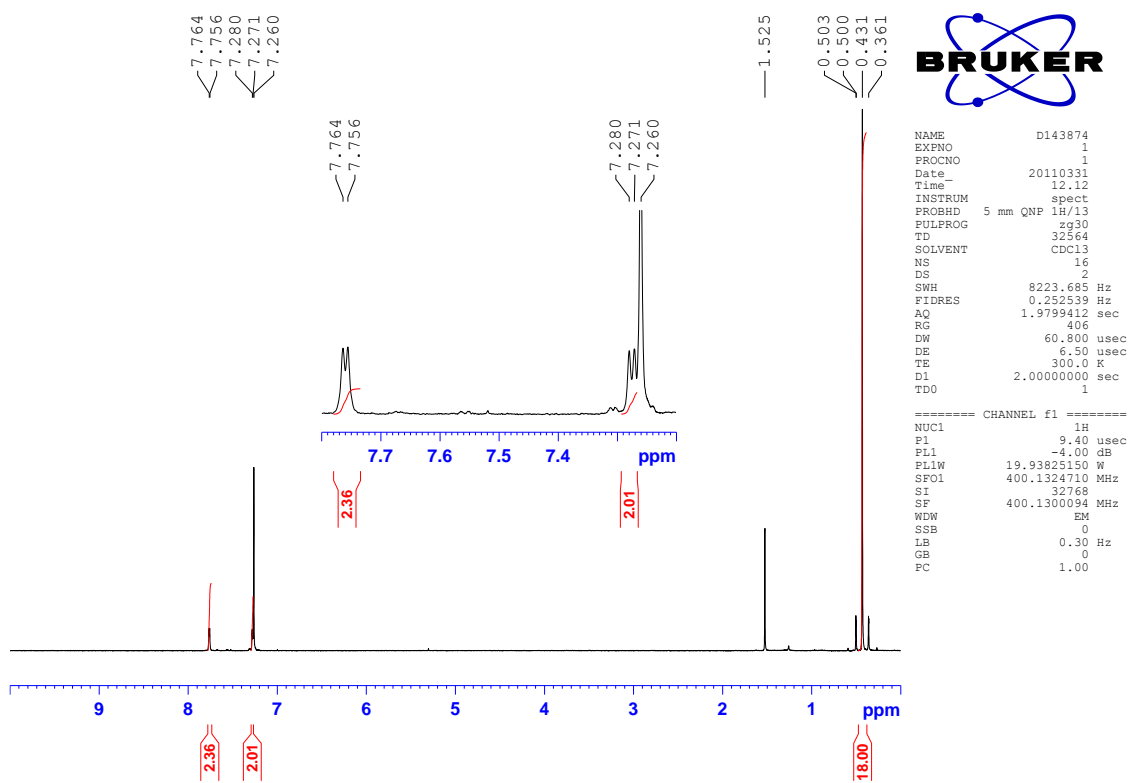


Figure 8.2: ^1H NMR spectrum of ((perfluoro-1,4-phenylene)bis(thiophene-5,2-diyl))bis(trimethylstannane) (**6.2d**)

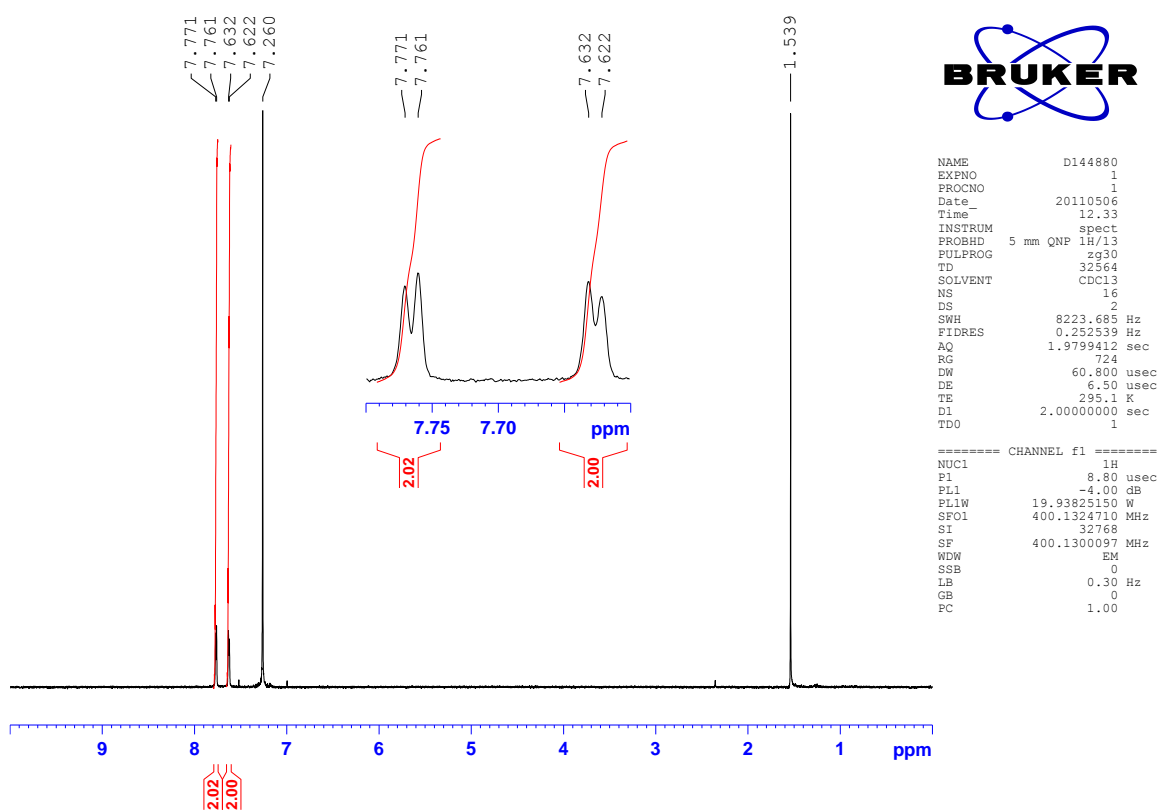


Figure 8.3: ^1H NMR spectrum of 5,5'-(perfluoro-1,4-phenylene)bis(2-(perfluorophenyl)thiophene) (**6.2e**)

8.4 Atomic force microscopy (AFM)

Atomic force microscope (AFM) images were recorded by Digital Instruments, Veeco metrology group, DimensionTM 3100, Version 4.43B. AFM involves moving a very small tip close to the substrate surface, a schematic is shown in figure 8.4. AFM operation can be either in a contact or in a tapping mode. When the tip is in a contact mode it can cause damage to the surface. Thus the tapping mode AFM is more commonly used. This moves the tip up and down, so it unevenly comes into contact with the surface but is not dragged on the thin film surface. So the tapping mode causes less damage than the contact one. The tip is held on a flexible cantilever, and when it

is close to the sample surface repulsive forces occur between the sample and the tip leading to a deflection of the cantilever. A laser beam is reflected off the cantilever to measure this deflection. The reflected beam is detected by a photodiode, allowing information about the surface topology to be recorded. The image processing software, WSxM V.5.0, was downloaded from www.nanotec.es software products. This software was used to produce all the AFM images shown in this thesis and also to obtain the RMS roughness and height distribution data.²⁷²

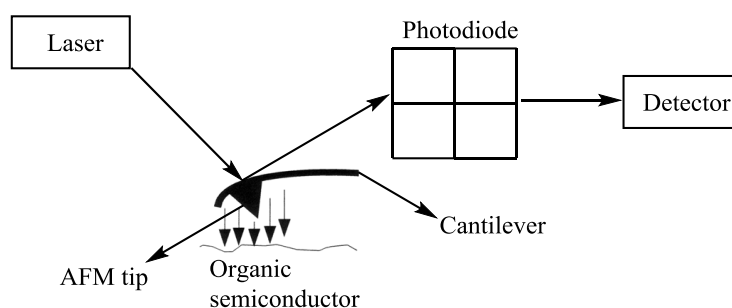


Figure 8.4: Schematic representation of atomic force microscopy

8.5 X-ray diffraction (XRD)

Thin film XRD data was collected on PANalytical Xpert diffractometer. The films were illuminated at a constant incidence angle of 0.2° with a wavelength of 1.54 \AA (Cu Anode) and incident energy of 40 keV. Bragg's equation ($d = \lambda / 2 \sin \theta$) was used to calculate interplanar distance. Ge-5T single crystal data were analysed from both Mercury and Diamond (CCDC) software.

Chapter 9

References

9.1 References

1. P. J. Skabara, *Chemical Communications*, 2013, 49, 9242-9244.
2. A. C. Grimsdale, K. Leok Chan, R. E. Martin, P. G. Jokisz and A. B. Holmes, *Chemical Reviews*, 2009, 109, 897-1091.
3. I. D. W. Samuel and G. A. Turnbull, *Chemical Reviews*, 2007, 107, 1272-1295.
4. Y. Yamashita, in (<http://iopscience.iop.org/1468-6996/10/2/024313>), 2009, vol. 10.
5. N. R. Armstrong, W. Wang, D. M. Alloway, D. Placencia, E. Ratcliff and M. Brumbach, *Macromolecular Rapid Communications*, 2009, 30, 717-731.
6. X. A. Zhu, C. , *Conf Proc IEEE Eng Med Biol Soc*, 2004, 3, 1968-1971.
7. S. R. F. Sven Möller¹, Craig Perlov², Warren Jackson², and Carl Taussig², *J. Appl. Phys.*, 2003, 94, 7811.
8. R. L. S. a. W. A. Phillips, in *Wiley*, 1980.
9. J. W. Rolf, *Wiley*, 1994.
10. A.J. Bard and L.R. Faulkner, ed. *J. W. a. S. inc, John Wiley and Sons inc.*, 2001.
11. J. D. Koryta, J. Principles of electrochemistry, 1987.
12. G. A. Mabbott, *Journal of Chemical Education*, 1983, 60, 697.
13. D. Pletcher, Peter, L., Peat, R., Robinson, J. and Greef, R., *Cambridge, GB, Woodhead Publishing*, 2001.
14. M. Heeney, W. Zhang, D. J. Crouch, M. L. Chabinyk, S. Gordeyev, R. Hamilton, S. J. Higgins, I. McCulloch, P. J. Skabara, D. Sparrowe and S. Tierney, *Chemical Communications*, 2007, DOI: 10.1039/B712398A, 5061-5063.
15. H. Pang, P. J. Skabara, S. Gordeyev, J. J. W. McDouall, S. J. Coles and M. B. Hursthouse, *Chemistry of Materials*, 2006, 19, 301-307.
16. D. J. Crouch, P. J. Skabara, J. E. Lohr, J. J. W. McDouall, M. Heeney, I. McCulloch, D. Sparrowe, M. Shkunov, S. J. Coles, P. N. Horton and M. B. Hursthouse, *Chemistry of Materials*, 2005, 17, 6567-6578.
17. B. Mollay, U. Lemmer, R. Kersting, R. F. Mahrt, H. Kurz, H. F. Kauffmann, auml and H. ssler, *Physical Review B*, 1994, 50, 10769.
18. H. Naarmann, *Wiley*, 2005.
19. H. Shirakawa, E. J. Louis, A. G. MacDiarmid, C. K. Chiang and A. J. Heeger, *Journal of the Chemical Society, Chemical Communications*, 1977, 578-580.
20. C. K. Chiang, C. R. Fincher, Jr., Y. W. Park, A. J. Heeger, H. Shirakawa, E. J. Louis, S. C. Gau and A. G. MacDiarmid, *Physical Review Letters*, 1977, 39, 1098-1101.
21. B. S. B. Arun Bahl, *S. Chand and Company*, 2003.
22. Z. Bao, *Advanced Materials*, 2000, 12, 227-230.
23. J. Roncali, P. Leriche and A. Cravino, *Advanced Materials*, 2007, 19, 2045-2060.
24. J. C. Perkinson, November 19, 2007.
25. N. M. Th. B. Singh, G. J. Matt, N. S. Sariciftci, R. Schwödiauer, and S. Bauer, *Applied physics letters*, 2004, 85.
26. G. Horowitz, *Advanced Materials*, 1998, 10, 365-377.
27. S. Y. P. Joonhyung Park, Sang-Oak Shim, Hyewon Kang, and Hong H. Lee, *Applied physics letters*, 2004, 85, 3283.
28. A. Operamolla and G. M. Farinola, *European Journal of Organic Chemistry*, 2011, 2011, 423-450.
29. R. H. F. H. Sirringhaus, X. C. Li, S. C. Moratti, A. B. Holmes, and N. Feeder, *Applied physics letters*, 1997, 71, 3871.
30. P. C. a. A. Bonfiglio, *Applied physics letters*, 2010, 97.

31. S. Allard, M. Forster, B. Souharce, H. Thiem and U. Scherf, *Angewandte Chemie International Edition*, 2008, 47, 4070-4098.
32. W. Xu and S.-W. Rhee, *Organic Electronics*, 2010, 11, 996-1004.
33. L. C. Augustin Joseph McEvoy, T. Markvart, *Elsevier*, 2013, second edition.
34. R. K. W. Harold J. Hovel, *Solar cells*, 1975, 11.
35. S. B. Darling and F. You, *RSC Advances*, 2013, 3, 17633-17648.
36. B. Kippelen and J.-L. Bredas, *Energy & Environmental Science*, 2009, 2, 251-261.
37. S. Günes, H. Neugebauer and N. S. Sariciftci, *Chemical Reviews*, 2007, 107, 1324-1338.
38. C. W. Tang, *Applied physics letters*, 1986, 48, 183-185.
39. B. C. Thompson and J. M. J. Fréchet, *Angewandte Chemie International Edition*, 2008, 47, 58-77.
40. S. B. Darling, *Energy & Environmental Science*, 2009, 2, 1266-1273.
41. M. Knupfer, *Appl Phys A*, 2003, 77, 623-626.
42. G. Chidichimo and L. Filippelli, *International Journal of Photoenergy*, 2010, 2010.
43. S. M. Lindner, S. Hüttner, A. Chiche, M. Thelakkat and G. Krausch, *Angewandte Chemie International Edition*, 2006, 45, 3364-3368.
44. L. J. A. Koster, *Phd thesis*, 2007.
45. S. E. Shaheen, C. J. Brabec, N. S. Sariciftci, F. Padinger, T. Fromherz and J. C. Hummelen, *Applied physics letters*, 2001, 78, 841-843.
46. S. Sista, Z. Hong, M.-H. Park, Z. Xu and Y. Yang, *Advanced Materials*, 2010, 22, E77-E80.
47. J. Y. Kim, K. Lee, N. E. Coates, D. Moses, T.-Q. Nguyen, M. Dante and A. J. Heeger, *Science*, 2007, 317, 222-225.
48. C. Waldauf, M. Morana, P. Denk, P. Schilinsky, K. Coakley, S. A. Choulis and C. J. Brabec, *Applied physics letters*, 2006, 89, 233517-233513.
49. S. K. Hau, H.-L. Yip, J. Zou and A. K. Y. Jen, *Organic Electronics*, 2009, 10, 1401-1407.
50. M. M. Wienk, J. M. Kroon, W. J. H. Verhees, J. Knol, J. C. Hummelen, P. A. van Hal and R. A. J. Janssen, *Angewandte Chemie International Edition*, 2003, 42, 3371-3375.
51. S. Yoo, W. J. Potscavage, B. Domercq, J. Kim, J. Holt and B. Kippelen, *Applied physics letters*, 2006, 89, 233516-233513.
52. Y. Yao, C. Shi, G. Li, V. Shrotriya, Q. Pei and Y. Yang, *Applied physics letters*, 2006, 89, 153507-153503.
53. V. D. Mihailetschi, L. J. A. Koster, J. C. Hummelen and P. W. M. Blom, *Physical Review Letters*, 2004, 93, 216601.
54. L. J. A. Koster, E. C. P. Smits, V. D. Mihailetschi and P. W. M. Blom, *Physical Review B*, 2005, 72, 085205.
55. D. Veldman, O. z. İpek, S. C. J. Meskers, J. r. Sweelssen, M. M. Koetse, S. C. Veenstra, J. M. Kroon, S. S. v. Bavel, J. Loos and R. A. J. Janssen, *Journal of the American Chemical Society*, 2008, 130, 7721-7735.
56. J.-M. Nunzi, *Comptes Rendus Physique*, 2002, 3, 523-542.
57. J. M. Kroon, M. M. Wienk, W. J. H. Verhees and J. C. Hummelen, *Thin Solid Films*, 2002, 403-404, 223-228.
58. W. H. Lee, J. H. Cho and K. Cho, *Journal of Materials Chemistry*, 2010, 20, 2549-2561.
59. W. Wu, Y. Liu and D. Zhu, *Chemical Society Reviews*, 2010, 39, 1489.
60. F. Gholamrezaie, *Phd thesis*, 2012.

61. Y. Ito, A. A. Virkar, S. Mannsfeld, J. H. Oh, M. Toney, J. Locklin and Z. Bao, *Journal of the American Chemical Society*, 2009, 131, 9396-9404.
62. R. A. B. Sasikumar Arumugam, Clara Orofino-Pena, Neil Findlay, Anto Regis Inigo, Alexander L. Kanibolotsky, and Peter. J. Skabara*, *Journal of Israel Chemistry*, 2014, 52, 1-9.
63. S.-C. L. Yu-Wei Su, and Kung-Hwa Wei*, *Materialstoday*, 2012, 15, 554-562.
64. A. Sharenko, M. Kuik, M. F. Toney and T.-Q. Nguyen, *Advanced Functional Materials*, 2014, DOI: 10.1002/adfm.201304100, n/a-n/a.
65. I. A. Wright, N. J. Findlay, S. Arumugam, A. R. Inigo, A. L. Kanibolotsky, P. Zassowski, W. Domagala and P. J. Skabara, *Journal of Materials Chemistry C*, 2014, 2, 2674-2683.
66. J. Wang and T. Higashihara, *Polymer Chemistry*, 2013, 4, 5518-5526.
67. Z. F. WANG ZiXuan, WANG Jin, XU XiaoWei, WANG Jian, LIU Yang, XU Zheng, *Chinese Science Bulletin*, 2012, 57, 4143-4152.
68. H.-C. Liao, C.-C. Ho, C.-Y. Chang, M.-H. Jao, S. B. Darling and W.-F. Su, *Materials Today*, 2013, 16, 326-336.
69. R. Y. Wasiu Adebayo Hammed, Abdura'uf Lukman Bola and Habibun Nabi Muhammad Ekramul Mahmud, *Energies*, 2013, 6, 5847-5868.
70. T. Benanti and D. Venkataraman, *Photosynth Res*, 2006, 87, 73-81.
71. I. A. Wright, P. J. Skabara, J. C. Forgie, A. L. Kanibolotsky, B. Gonzalez, S. J. Coles, S. Gambino and I. D. W. Samuel, *Journal of Materials Chemistry*, 2011, 21, 1462-1469.
72. D. Cortizo-Lacalle, S. Arumugam, S. E. T. Elmasly, A. L. Kanibolotsky, N. J. Findlay, A. R. Inigo and P. J. Skabara, *Journal of Materials Chemistry*, 2012, 22, 11310-11315.
73. I. A. Wright, A. L. Kanibolotsky, J. Cameron, T. Tuttle, P. J. Skabara, S. J. Coles, C. T. Howells, S. A. J. Thomson, S. Gambino and I. D. W. Samuel, *Angewandte Chemie International Edition*, 2012, 51, 4562-4567.
74. S. Arumugam, I. A. Wright, A. R. Inigo, S. Gambino, C. T. Howells, A. L. Kanibolotsky, P. J. Skabara and I. D. W. Samuel, *Journal of Materials Chemistry C*, 2014, 2, 34-39.
75. A. L. Kanibolotsky, F. Vilela, J. C. Forgie, S. E. T. Elmasly, P. J. Skabara, K. Zhang, B. Tieke, J. McGurk, C. R. Belton, P. N. Stavrinou and D. D. C. Bradley, *Advanced Materials*, 2011, 23, 2093-2097.
76. T. Kanbara, K. Shibata, S. Fujiki, Y. Kubozono, S. Kashino, T. Urisu, M. Sakai, A. Fujiwara, R. Kumashiro and K. Tanigaki, *Chemical Physics Letters*, 2003, 379, 223-229.
77. A. Facchetti, M. Mushrush, H. E. Katz and T. J. Marks, *Advanced Materials*, 2003, 15, 33-38.
78. M.-H. Yoon, S. A. DiBenedetto, A. Facchetti and T. J. Marks, *Journal of the American Chemical Society*, 2005, 127, 1348-1349.
79. A. Facchetti, M.-H. Yoon, C. L. Stern, H. E. Katz and T. J. Marks, *Angewandte Chemie International Edition*, 2003, 42, 3900-3903.
80. H. Usta, A. Facchetti and T. J. Marks, *Accounts of Chemical Research*, 2011, 44, 501-510.
81. X. Gao and Y. Hu, *Journal of Materials Chemistry C*, 2014, 2, 3099-3117.
82. M. Mas-Torrent, M. Durkut, P. Hadley, X. Ribas and C. Rovira, *Journal of the American Chemical Society*, 2004, 126, 984-985.
83. M. Mas-Torrent, P. Hadley, S. T. Bromley, N. Crivillers, J. Veciana and C. Rovira, *Applied Physics Letters*, 2005, 86, 012110-012113.

84. J. Casado, M. Z. Zgierski, M. C. R. Delgado, J. T. L. Navarrete, M. Mas-Torrent and C. Rovira, *The Journal of Physical Chemistry C*, 2007, 111, 10110-10118.
85. S. A. DiBenedetto, A. Facchetti, M. A. Ratner and T. J. Marks, *Advanced Materials*, 2009, 21, 1407-1433.
86. B. de Boer, A. Hadipour, M. M. Mandoc, T. van Woudenberg and P. W. M. Blom, *Advanced Materials*, 2005, 17, 621-625.
87. K. Demirkan, A. Mathew, C. Weiland, Y. Yao, A. M. Rawlett, J. M. Tour and R. L. Opila, *The Journal of Chemical Physics*, 2008, 128, 074705.
88. I. Hargittai, J. Brunvoll, M. Kolonits and V. Khodorkovsky, *Journal of Molecular Structure*, 1994, 317, 273-277.
89. M. Mas-Torrent and C. Rovira, *Journal of Materials Chemistry*, 2006, 16, 433-436.
90. P. Atkins and J. de Paula, *Physical Chemistry*, Oxford University Press, 2006.
91. M. Mas-Torrent and C. Rovira, *Chemical Society Reviews*, 2008, 37, 827-838.
92. W. Q. Xike Gao, Yunqi Liu, Gui Yu and Daoben Zhu, *Pure and applied chemistry*, 2008, 80, 2405-2423.
93. X. Gao, W. Wu, Y. Liu, W. Qiu, X. Sun, G. Yu and D. Zhu, *Chemical Communications*, 2006, 0, 2750-2752.
94. X. Gao, W. Wu, Y. Liu, S. Jiao, W. Qiu, G. Yu, L. Wang and D. Zhu, *Journal of Materials Chemistry*, 2007, 17, 736-743.
95. S. Ukai, S. Igarashi, M. Nakajima, K. Marumoto, H. Ito, S. Kuroda, K. Nishimura, Y. Enomoto and G. Saito, *Colloids and Surfaces A: Physicochemical and Engineering Aspects*, 2006, 284-285, 589-593.
96. I. Doi, E. Miyazaki, K. Takimiya and Y. Kunugi, *Chemistry of Materials*, 2007, 19, 5230-5237.
97. J. W. Sease and L. Zechmeister, *Journal of the American Chemical Society*, 1947, 69, 270-273.
98. G. Horowitz, D. Fichou, X. Peng, Z. Xu and F. Garnier, *Solid State Communications*, 1989, 72, 381-384.
99. G. Horowitz, X. Z. Peng, D. Fichou and F. Garnier, *Journal of Molecular Electronics*, 1991, 7, 85-89.
100. F. Garnier, G. Horowitz, D. Fichou and A. Yassar, *Synthetic Metals*, 1996, 81, 163-171.
101. A. Dodabalapur, L. Torsi and H. E. Katz, *Science*, 1995, 268, 270-271.
102. H. E. Katz, L. Torsi and A. Dodabalapur, *Chemistry of Materials*, 1995, 7, 2235-2237.
103. G. Horowitz, X. Peng, D. Fichou and F. Garnier, *Journal of Applied Physics*, 1990, 67, 528-532.
104. F. Garnier, A. Yassar, R. Hajlaoui, G. Horowitz, F. Deloffre, B. Servet, S. Ries and P. Alnot, *Journal of the American Chemical Society*, 1993, 115, 8716-8721.
105. H. Akimichi, K. Waragai, S. Hotta, H. Kano and H. Sakaki, *Applied Physics Letters*, 1991, 58, 1500-1502.
106. B. Servet, G. Horowitz, S. Ries, O. Lagorsse, P. Alnot, A. Yassar, F. Deloffre, P. Srivastava and R. Hajlaoui, *Chemistry of Materials*, 1994, 6, 1809-1815.
107. R. Hajlaoui, G. Horowitz, F. Garnier, A. Arce-Bouchet, L. Laigre, A. E. Kassmi, F. Demanze and F. Kouki, *Advanced Materials*, 1997, 9, 389-391.
108. G. Horowitz, F. Garnier, A. Yassar, R. Hajlaoui and F. Kouki, *Advanced Materials*, 1996, 8, 52-54.
109. M. Halik, H. Klauk, U. Zschieschang, G. Schmid, S. Ponomarenko, S. Kirchmeyer and W. Weber, *Advanced Materials*, 2003, 15, 917-922.

110. T. Kaikawa, K. Takimiya, Y. Aso and T. Otsubo, *Organic Letters*, 2000, 2, 4197-4199.
111. M. G. Hill, K. R. Mann, L. L. Miller and J. F. Penneau, *Journal of the American Chemical Society*, 1992, 114, 2728-2730.
112. K. M. Knoblock, C. J. Silvestri and D. M. Collard, *Journal of the American Chemical Society*, 2006, 128, 13680-13681.
113. P. J. Skabara, R. Berridge, E. J. L. McInnes, D. P. West, S. J. Coles, M. B. Hursthouse and K. Mullen, *Journal of Materials Chemistry*, 2004, 14, 1964-1969.
114. R. Berridge, P. J. Skabara, C. Pozo-Gonzalo, A. Kanibolotsky, J. Lohr, J. J. W. McDouall, E. J. L. McInnes, J. Wolowska, C. Winder, N. S. Sariciftci, R. W. Harrington and W. Clegg, *The Journal of Physical Chemistry B*, 2006, 110, 3140-3152.
115. P. J. Skabara, D. M. Roberts, I. M. Serebryakov and C. Pozo-Gonzalo, *Chemical Communications*, 2000, DOI: 10.1039/b001943g, 1005-1006.
116. A. L. Kanibolotsky, L. Kanibolotskaya, S. Gordeyev, P. J. Skabara, I. McCulloch, R. Berridge, J. E. Lohr, F. Marchioni and F. Wudl, *Organic Letters*, 2007, 9, 1601-1604.
117. J. Chang, J. Li, K. L. Chang, J. Zhang and J. Wu, *RSC Advances*, 2013, 3, 8721-8727.
118. D. M. Taylor, *Dielectrics and Electrical Insulation, IEEE Transactions on*, 2006, 13, 1063-1073.
119. H. Dong, L. Jiang and W. Hu, *Physical Chemistry Chemical Physics*, 2012, 14, 14165-14180.
120. H. Akimichi, K. Waragai, S. Hotta, H. Kano and H. Sakaki, *Applied Physics Letters*, 1991, 58, 1500-1502.
121. G. Yu, J. Gao, J. C. Hummelen, F. Wudl and A. J. Heeger, *Science*, 1995, 270, 1789-1791.
122. C. J. Brabec, N. S. Sariciftci and J. C. Hummelen, *Advanced Functional Materials*, 2001, 11, 15-26.
123. T. Kietzke, *Advances in OptoElectronics*, 2007, 2007.
124. J. P. Farges, *Organic Conductors: Fundamentals and Applications*, Marcel Dekker, Incorporated, 1994.
125. D. Kreher, M. Cariou, S.-G. Liu, E. Levillain, J. Veciana, C. Rovira, A. Gorgues and P. Hudhomme, *Journal of Materials Chemistry*, 2002, 12, 2137-2159.
126. A. Suzuki, K. Inoue, K. Yano, T. Oku and K. Kikuchi, *Journal of Physics and Chemistry of Solids*, 2010, 71, 1587-1591.
127. K. Y. Atsushi Suzuki, Takeo Oku, *Materials Science Forum* 2011, 688, 80-84.
128. N. Noma, T. Tsuzuki and Y. Shirota, *Advanced Materials*, 1995, 7, 647-648.
129. k. m. Y. kuwabara, k. Nawa, N. Noma, Y. Shirota, *Nippon kagaku kaishi* 1992, 1992, 1168-1173.
130. J. Sakai, T. Taima and K. Saito, *Organic Electronics*, 2008, 9, 582-590.
131. F. Yang, M. Shtein and S. R. Forrest, *Nat Mater*, 2005, 4, 37-41.
132. K. H. Hendriks, G. H. L. Heintges, V. S. Gevaerts, M. M. Wienk and R. A. J. Janssen, *Angewandte Chemie International Edition*, 2013, DOI: 10.1002/anie.201302319, n/a-n/a.
133. H. Bronstein, R. S. Ashraf, Y. Kim, A. J. P. White, T. Anthopoulos, K. Song, D. James, W. Zhang and I. McCulloch, *Macromolecular Rapid Communications*, 2011, 32, 1664-1668.
134. C.-Y. Chen, C.-S. Tsao, Y.-C. Huang, H.-W. Liu, W.-Y. Chiu, C.-M. Chuang, U. S. Jeng, C.-J. Su, W.-R. Wu, W.-F. Su and L. Wang, *Nanoscale*, 2013, 5, 7629-7638.
135. W. Tang, J. Hai, Y. Dai, Z. Huang, B. Lu, F. Yuan, J. Tang and F. Zhang, *Solar Energy Materials and Solar Cells*, 2010, 94, 1963-1979.

136. A. Facchetti, *Chemistry of Materials*, 2010, 23, 733-758.
137. J.-L. Brédas, J. E. Norton, J. Cornil and V. Coropceanu, *Accounts of Chemical Research*, 2009, 42, 1691-1699.
138. P. M. Beaujuge and J. M. J. Fréchet, *Journal of the American Chemical Society*, 2011, 133, 20009-20029.
139. J. D. Yuen and F. Wudl, *Energy & Environmental Science*, 2013, 6, 392-406.
140. A. R. Murphy and J. M. J. Fréchet, *Chemical Reviews*, 2007, 107, 1066-1096.
141. J. Zaumseil and H. Sirringhaus, *Chemical Reviews*, 2007, 107, 1296-1323.
142. K. S. Yook and J. Y. Lee, *Advanced Materials*, 2012, 24, 3169-3190.
143. M. Sessolo and H. J. Bolink, *Advanced Materials*, 2011, 23, 1829-1845.
144. G. Gunbas and L. Toppare, *Chemical Communications*, 2012, 48, 1083-1101.
145. R. L. Elsenbaumer, K. Y. Jen and R. Oboodi, *Synthetic Metals*, 1986, 15, 169-174.
146. R. D. McCullough and R. D. Lowe, *Journal of the Chemical Society, Chemical Communications*, 1992, 0, 70-72.
147. T. A. Chen and R. D. Rieke, *Journal of the American Chemical Society*, 1992, 114, 10087-10088.
148. W. Ma, C. Yang, X. Gong, K. Lee and A. J. Heeger, *Advanced Functional Materials*, 2005, 15, 1617-1622.
149. S. Luňák Jr, J. Vyňuchal and R. Hrdina, *Journal of Molecular Structure*, 2009, 919, 239-245.
150. F. Nourmohammadian, I. Yavari, A. R. Mirhabibi and S. Moradi, *Dyes and Pigments*, 2005, 67, 15-20.
151. S. Schutting, S. M. Borisov and I. Klimant, *Analytical Chemistry*, 2013, 85, 3271-3279.
152. B. Zhao, K. Sun, F. Xue and J. Ouyang, *Organic Electronics*, 2012, 13, 2516-2524.
153. J. C. Bijleveld, A. P. Zoombelt, S. G. J. Mathijssen, M. M. Wienk, M. Turbiez, D. M. de Leeuw and R. A. J. Janssen, *Journal of the American Chemical Society*, 2009, 131, 16616-16617.
154. J. S. Lee, S. K. Son, S. Song, H. Kim, D. R. Lee, K. Kim, M. J. Ko, D. H. Choi, B. Kim and J. H. Cho, *Chemistry of Materials*, 2012, 24, 1316-1323.
155. Y. Li, P. Sonar, S. P. Singh, M. S. Soh, M. van Meurs and J. Tan, *Journal of the American Chemical Society*, 2011, 133, 2198-2204.
156. Y. Li, S. P. Singh and P. Sonar, *Advanced Materials*, 2010, 22, 4862-4866.
157. Z. Chen, M. J. Lee, R. Shahid Ashraf, Y. Gu, S. Albert-Seifried, M. Meedom Nielsen, B. Schroeder, T. D. Anthopoulos, M. Heeney, I. McCulloch and H. Sirringhaus, *Advanced Materials*, 2012, 24, 647-652.
158. J. Li, Y. Zhao, H. S. Tan, Y. Guo, C.-A. Di, G. Yu, Y. Liu, M. Lin, S. H. Lim, Y. Zhou, H. Su and B. S. Ong, *Sci. Rep.*, 2012, 2.
159. X. Zhang, L. J. Richter, D. M. DeLongchamp, R. J. Kline, M. R. Hammond, I. McCulloch, M. Heeney, R. S. Ashraf, J. N. Smith, T. D. Anthopoulos, B. Schroeder, Y. H. Geerts, D. A. Fischer and M. F. Toney, *Journal of the American Chemical Society*, 2011, 133, 15073-15084.
160. H. Bronstein, Z. Chen, R. S. Ashraf, W. Zhang, J. Du, J. R. Durrant, P. Shakya Tuladhar, K. Song, S. E. Watkins, Y. Geerts, M. M. Wienk, R. A. J. Janssen, T. Anthopoulos, H. Sirringhaus, M. Heeney and I. McCulloch, *Journal of the American Chemical Society*, 2011, 133, 3272-3275.
161. J. C. Bijleveld, V. S. Gevaerts, D. Di Nuzzo, M. Turbiez, S. G. J. Mathijssen, D. M. de Leeuw, M. M. Wienk and R. A. J. Janssen, *Advanced Materials*, 2010, 22, E242-E246.

162. J. W. Lee, Y. S. Choi and W. H. Jo, *Organic Electronics*, 2012, 13, 3060-3066.
163. J. Peet, M. L. Senatore, A. J. Heeger and G. C. Bazan, *Advanced Materials*, 2009, 21, 1521-1527.
164. F. Liu, Y. Gu, C. Wang, W. Zhao, D. Chen, A. L. Briseno and T. P. Russell, *Advanced Materials*, 2012, 24, 3947-3951.
165. M. M. Wienk, M. Turbiez, J. Gilot and R. A. J. Janssen, *Advanced Materials*, 2008, 20, 2556-2560.
166. Y. Yao, J. Hou, Z. Xu, G. Li and Y. Yang, *Advanced Functional Materials*, 2008, 18, 1783-1789.
167. J. K. Lee, W. L. Ma, C. J. Brabec, J. Yuen, J. S. Moon, J. Y. Kim, K. Lee, G. C. Bazan and A. J. Heeger, *Journal of the American Chemical Society*, 2008, 130, 3619-3623.
168. G. Zhang, Y. Fu, Z. Xie and Q. Zhang, *Solar Energy Materials and Solar Cells*, 2011, 95, 1168-1173.
169. J. C. Bijleveld, R. A. M. Verstrijden, M. M. Wienk and R. A. J. Janssen, *Journal of Materials Chemistry*, 2011, 21, 9224-9231.
170. J. J. M. Halls, J. Cornil, D. A. dos Santos, R. Silbey, D. H. Hwang, A. B. Holmes, J. L. Brédas and R. H. Friend, *Physical Review B*, 1999, 60, 5721-5727.
171. H. Ohkita, S. Cook, Y. Astuti, W. Duffy, S. Tierney, W. Zhang, M. Heaney, I. McCulloch, J. Nelson, D. D. C. Bradley and J. R. Durrant, *Journal of the American Chemical Society*, 2008, 130, 3030-3042.
172. J.-i. Yamada, H. Akutsu, H. Nishikawa and K. Kikuchi, *Chemical Reviews*, 2004, 104, 5057-5084.
173. J. Roncali, *Advanced Energy Materials*, 2011, 1, 147-160.
174. S. Miyanishi, Y. Zhang, K. Tajima and K. Hashimoto, *Chemical Communications*, 2010, 46, 6723-6725.
175. Y. Olivier, *Phd thesis*, 2008.
176. M. L. Chabinyk, R. Lujan, F. Endicott, M. F. Toney, I. McCulloch and M. Heaney, *Applied Physics Letters*, 2007, 90, 233503-233508.
177. K. Ryu, I. Kymissis, V. Bulovic and C. G. Sodi, *Electron Device Letters, IEEE*, 2005, 26, 716-718.
178. G. Gu, M. G. Kane and S.-C. Mau, *Journal of Applied Physics*, 2007, 101, 014504.
179. G. Gu and M. G. Kane, *Applied Physics Letters*, 2008, 92, -.
180. W. M. Y. Se Hyun Kim, Oh-Kwan Kwon, Kipyong Hong, Chanwoo Yang, Woon-Seop Choi and Chan Eon Park, *Journal of Physics D: Applied Physics*, 2010, 43, 456102.
181. S. H. Kim, S. Nam, J. Jang, K. Hong, C. Yang, D. S. Chung, C. E. Park and W.-S. Choi, *Journal of Applied Physics*, 2009, 105, -.
182. F.-C. Chen, C.-W. Chu, J. He, Y. Yang and J.-L. Lin, *Applied Physics Letters*, 2004, 85, 3295-3297.
183. J. Veres, S. D. Ogier, S. W. Leeming, D. C. Cupertino and S. Mohialdin Khaffaf, *Advanced Functional Materials*, 2003, 13, 199-204.
184. J. Yuan, X. Huang, F. Zhang, J. Lu, Z. Zhai, C. Di, Z. Jiang and W. Ma, *Journal of Materials Chemistry*, 2012, 22, 22734-22742.
185. Q. Zhang, A. Cirpan, T. P. Russell and T. Emrick, *Macromolecules*, 2009, 42, 1079-1082.
186. M. Sommer, S. Huttner, U. Steiner and M. Thelakkat, *Applied Physics Letters*, 2009, 95, 183308-183303.
187. B. Walker, C. Kim and T.-Q. Nguyen, *Chemistry of Materials*, 2010, 23, 470-482.
188. P. J. Skabara, J.-B. Arlin and Y. H. Geerts, *Advanced Materials*, 2013, 25, 1948-1954.

189. S. Roquet, R. de Bettignies, P. Leriche, A. Cravino and J. Roncali, *Journal of Materials Chemistry*, 2006, 16, 3040-3045.
190. A. L. Kanibolotsky, I. F. Perepichka and P. J. Skabara, *Chemical Society Reviews*, 2010, 39, 2695-2728.
191. T. P. I. Saragi, T. Fuhrmann-Lieker and J. Salbeck, *Advanced Functional Materials*, 2006, 16, 966-974.
192. A. Zen, P. Pingel, F. Jaiser, D. Neher, J. Grenzer, W. Zhuang, J. P. Rabe, A. Bilge, F. Galbrecht, B. S. Nehls, T. Farrell, U. Scherf, R. D. Abellon, F. C. Grozema and L. D. A. Siebbeles, *Chemistry of Materials*, 2007, 19, 1267-1276.
193. J. Pina, J. Seixas de Melo, H. D. Burrows, A. Bilge, T. Farrell, M. Forster and U. Scherf, *The Journal of Physical Chemistry B*, 2006, 110, 15100-15106.
194. T. P. I. Saragi, T. Spehr, A. Siebert, T. Fuhrmann-Lieker and J. Salbeck, *Chemical Reviews*, 2007, 107, 1011-1065.
195. R. Pudzich, T. Fuhrmann-Lieker and J. Salbeck, *Advances in Polymer Science*, 2006, 199, 83-142.
196. J. Salbeck, N. Yu, J. Bauer, F. Weissörtel and H. Bestgen, *Synthetic Metals*, 1997, 91, 209-215.
197. U. Bach, D. Lupo, P. Comte, J. E. Moser, F. Weissörtel, J. Salbeck, H. Spreitzer and M. Gratzel, *Nature*, 1998, 395, 583-585.
198. H. J. Snaith, A. J. Moule, C. Klein, K. Meerholz, R. H. Friend and M. Gratzel, *Nano Lett.*, 2007, 7, 3372-3376.
199. E. Cadoni, E. Perra, C. Fattuoni, G. Bruno, M. G. Cabiddu, S. De Montis and S. Cabiddu, *Tetrahedron*, 2009, 65, 2279-2284.
200. K. Ueda, M. Yamanoha, T. Sugimoto, H. Fujita, A. Ugawa, K. Yakushi and K. Kano, *Chem. Lett.*, 1997, 461-462.
201. K. Ueda, M. Iwamatsu, T. Sugimoto, T. Tada and K. Nishimura, *Acta Crystallogr. Sect. C-Cryst. Struct. Commun.*, 2000, 56, E160-E161.
202. U. Herzog, U. Bohme and G. Rheinwald, *J. Organomet. Chem.*, 2000, 612, 133-140.
203. J. Pfeiffer, M. Noltemeyer and A. Meller, *Z. Anorg. Allg. Chem.*, 1989, 572, 145-150.
204. F. H. Fink, J. A. Turner and D. A. Payne, *Journal of the American Chemical Society*, 1966, 88, 1571-1572.
205. D. A. Payne and F. H. Fink, *Journal of Chemical Education*, 1966, 43, 654-656.
206. G. N. Schrauzer, *Accounts of Chemical Research*, 1969, 2, 72-80.
207. R. Kato, *Chemical Reviews*, 2004, 104, 5319-5346.
208. P. Cassoux, L. Valade, H. Kobayashi, A. Kobayashi, R. A. Clark and A. E. Underhill, *Coordination Chemistry Reviews*, 1991, 110, 115-160.
209. N. Robertson and L. Cronin, *Coordination Chemistry Reviews*, 2002, 227, 93-127.
210. C. L. Beswick, in *Progress in Inorganic Chemistry*, John Wiley & Sons Inc, New York, 2004, vol. 52, pp. 55-110.
211. J. Guay, A. Diaz, R. L. Wu and J. M. Tour, *Journal of the American Chemical Society*, 1993, 115, 1869-1874.
212. T. P. I. Saragi, T. Fuhrmann-Lieker and J. Salbeck, *Synthetic Metals*, 2005, 148, 267-270.
213. F. Steuber, J. Staudigel, M. Stössel, J. Simmerer, A. Winnacker, H. Spreitzer, F. Weissörtel and J. Salbeck, *Advanced Materials*, 2000, 12, 130-133.
214. T. P. I. Saragi, J. Londenberg and J. Salbeck, *Journal of Applied Physics*, 2007, 102, 046104-046103.
215. L. M. Wilson and A. C. Griffin, *Journal of Materials Chemistry*, 1993, 3, 991-994.

216. S. Wang, W. J. Oldham, R. A. Hudack and G. C. Bazan, *Journal of the American Chemical Society*, 2000, 122, 5695-5709.
217. P. Ganesan, X. Yang, J. Loos, T. J. Savenije, R. D. Abellon, H. Zuilhof and E. J. R. Sudhölter, *Journal of the American Chemical Society*, 2005, 127, 14530-14531.
218. J. Roncali, C. Thobie-Gautier, H. Brisset, J.-F. Favart and A. Guy, *Journal of Electroanalytical Chemistry*, 1995, 381, 257-260.
219. C. H. Tan, A. R. Inigo, W. Fann, P.-K. Wei, G.-Y. Perng and S.-A. Chen, *Organic Electronics*, 2002, 3, 81-88.
220. S. C. Youngkyoo Kim, Sachetan M. Tuladhar, Stelios A. Choulis, Jenny Nelson, James R. Durrant, Donal D. C. Bradley, Mark Giles, Iain McCulloch, Chang-Sik Ha & Moonhor Ree, *Nature materials* 5, 2006, 2006.
221. R. J. Baldwin, T. Kreouzis, M. Shkunov, M. Heeney, W. Zhang and I. McCulloch, *Journal of Applied Physics*, 2007, 101, 023713-023710.
222. J. B. Birks, *Photophysics of aromatic molecules*, Wiley-Interscience, London; New York, 1970.
223. K.-T. Wong, Y.-Y. Chien, R.-T. Chen, C.-F. Wang, Y.-T. Lin, H.-H. Chiang, P.-Y. Hsieh, C.-C. Wu, C. H. Chou, Y. O. Su, G.-H. Lee and S.-M. Peng, *Journal of the American Chemical Society*, 2002, 124, 11576-11577.
224. S. Setayesh, A. C. Grimsdale, T. Weil, V. Enkelmann, K. Müllen, F. Meghdadi, E. J. W. List and G. Leising, *Journal of the American Chemical Society*, 2001, 123, 946-953.
225. M. T. Bernius, M. Inbasekaran, J. O'Brien and W. Wu, *Advanced Materials*, 2000, 12, 1737-1750.
226. D. Neher, *Macromolecular Rapid Communications*, 2001, 22, 1365-1385.
227. M. Knaapila, R. Stepanyan, B. P. Lyons, M. Torkkeli and A. P. Monkman, *Advanced Functional Materials*, 2006, 16, 599-609.
228. D. C. Müller, T. Braig, H.-G. Nothofer, M. Arnoldi, M. Gross, U. Scherf, O. Nuyken and K. Meerholz, *ChemPhysChem*, 2000, 1, 207-211.
229. G. Heliotis, R. Xia, D. D. C. Bradley, G. A. Turnbull, I. D. W. Samuel, P. Andrew and W. L. Barnes, *Journal of Applied Physics*, 2004, 96, 6959-6965.
230. G. Heliotis, R. Xia, G. A. Turnbull, P. Andrew, W. L. Barnes, I. D. W. Samuel and D. D. C. Bradley, *Advanced Functional Materials*, 2004, 14, 91-97.
231. G. Heliotis, R. Xia, D. D. C. Bradley, G. A. Turnbull, I. D. W. Samuel, P. Andrew and W. L. Barnes, *Applied Physics Letters*, 2003, 83, 2118-2120.
232. A. C. Arias, N. Corcoran, M. Banach, R. H. Friend, J. D. MacKenzie and W. T. S. Huck, *Applied Physics Letters*, 2002, 80, 1695-1697.
233. A. C. Arias, J. D. MacKenzie, R. Stevenson, J. J. M. Halls, M. Inbasekaran, E. P. Woo, D. Richards and R. H. Friend, *Macromolecules*, 2001, 34, 6005-6013.
234. R. Stevenson, A. C. Arias, C. Ramsdale, J. D. MacKenzie and D. Richards, *Applied Physics Letters*, 2001, 79, 2178-2180.
235. K. Müllen and G. Wegner, *Advanced Materials*, 1998, 10, 433-436.
236. W. G. Mullen K, *Wiley-VCH, New York*, 1998.
237. A. L. Kanibolotsky, R. Berridge, P. J. Skabara, I. F. Perepichka, D. D. C. Bradley and M. Koeberg, *Journal of the American Chemical Society*, 2004, 126, 13695-13702.
238. M. Moreno Oliva, J. Casado, J. T. López Navarrete, R. Berridge, P. J. Skabara, A. L. Kanibolotsky and I. F. Perepichka, *The Journal of Physical Chemistry B*, 2007, 111, 4026-4035.
239. K. M. Omer, A. L. Kanibolotsky, P. J. Skabara, I. F. Perepichka and A. J. Bard, *The Journal of Physical Chemistry B*, 2007, 111, 6612-6619.

240. C.-C. Wu, T.-L. Liu, Y.-T. Lin, W.-Y. Hung, T.-H. Ke, K.-T. Wong and T.-C. Chao, *Applied Physics Letters*, 2004, 85, 1172-1174.
241. B. S. Gaylord, S. Wang, A. J. Heeger and G. C. Bazan, *Journal of the American Chemical Society*, 2001, 123, 6417-6418.
242. Y. Wang, G. Tsiminis, Y. Yang, A. Ruseckas, A. L. Kanibolotsky, I. F. Perepichka, P. J. Skabara, G. A. Turnbull and I. D. W. Samuel, *Synthetic Metals*, 2010, 160, 1397-1400.
243. G. Tsiminis, Y. Wang, P. E. Shaw, A. L. Kanibolotsky, I. F. Perepichka, M. D. Dawson, P. J. Skabara, G. A. Turnbull and I. D. W. Samuel, *Applied Physics Letters*, 2009, 94, -.
244. G. Tsiminis, N. A. Montgomery, A. L. Kanibolotsky, A. Ruseckas, I. F. Perepichka, P. J. Skabara, G. A. Turnbull and I. D. W. Samuel, *Semiconductor Science and Technology*, 2012, 27, 094005.
245. S. C. J. Meskers, R. A. J. Janssen, J. E. M. Haverkort and J. H. Wolter, *Chemical Physics*, 2000, 260, 415-439.
246. M. Fakis, I. Polyzos, G. Tsigaridas, V. Giannetas, P. Persephonis, I. Spiliopoulos and J. Mikroyannidis, *Optical Materials*, 2004, 27, 503-507.
247. H. E. Katz, Z. Bao and S. L. Gilat, *Accounts of Chemical Research*, 2001, 34, 359-369.
248. J. U. Wallace and S. H. Chen, in *Polyfluorenes*, eds. U. Scherf and D. Neher, Springer Berlin Heidelberg, 2008, vol. 212, ch. 152, pp. 145-186.
249. C. Chi, C. Im and G. Wegner, *The Journal of Chemical Physics*, 2006, 124, 024907-024908.
250. Y. Qu, J. Hua and H. Tian, *Organic Letters*, 2010, 12, 3320-3323.
251. V. Amendola, D. Esteban-Gómez, L. Fabbrizzi and M. Licchelli, *Accounts of Chemical Research*, 2006, 39, 343-353.
252. P. Sonar, L. Oldridge, A. C. Grimsdale, K. Müllen, M. Surin, R. Lazzaroni, P. Leclère, J. Pinto, L.-L. Chua, H. Siringhaus and R. H. Friend, *Synthetic Metals*, 2010, 160, 468-474.
253. A. R. Rabindranath, Y. Zhu, K. Zhang and B. Tieke, *Polymer*, 2009, 50, 1637-1644.
254. K. Zhang, B. Tieke, J. C. Forgie, F. Vilela, J. A. Parkinson and P. J. Skabara, *Polymer*, 2010, 51, 6107-6114.
255. M. L. Tang and Z. Bao, *Chemistry of Materials*, 2010, 23, 446-455.
256. H. Dong, C. Wang and W. Hu, *Chemical Communications*, 2010, 46, 5211-5222.
257. H. Zhou, L. Yang, A. C. Stuart, S. C. Price, S. Liu and W. You, *Angewandte Chemie International Edition*, 2011, 50, 2995-2998.
258. F. Babudri, G. M. Farinola, F. Naso and R. Ragni, *Chemical Communications*, 2007, 1003-1022.
259. J. L. Brédas and A. J. Heeger, *Chemical Physics Letters*, 1994, 217, 507-512.
260. A. Facchetti, M. Mushrush, M.-H. Yoon, G. R. Hutchison, M. A. Ratner and T. J. Marks, *Journal of the American Chemical Society*, 2004, 126, 13859-13874.
261. D. J. Crouch, P. J. Skabara, M. Heeney, I. McCulloch, S. J. Coles and M. B. Hursthouse, *Chemical Communications*, 2005, 1465-1467.
262. J. A. Letizia, A. Facchetti, C. L. Stern, M. A. Ratner and T. J. Marks, *Journal of the American Chemical Society*, 2005, 127, 13476-13477.
263. J. A. Letizia, S. Cronin, R. P. Ortiz, A. Facchetti, M. A. Ratner and T. J. Marks, *Chemistry – A European Journal*, 2010, 16, 1911-1928.
264. D. J. Crouch, P. J. Skabara, M. Heeney, I. McCulloch, D. Sparrowe, S. J. Coles and M. B. Hursthouse, *Macromolecular Rapid Communications*, 2008, 29, 1839-1843.

265. E. Hwang, K. M. N. de Silva, C. B. Seevers, J.-R. Li, J. C. Garno and E. E. Nesterov, *Langmuir*, 2008, 24, 9700-9706.
266. M. C. McCairn, T. Kreouzis and M. L. Turner, *Journal of Materials Chemistry*, 2010, 20, 1999-2006.
267. K. Geramita, J. McBee, Y. Shen, N. Radu and T. D. Tilley, *Chemistry of Materials*, 2006, 18, 3261-3269.
268. T. Okamoto, K. Nakahara, A. Saeki, S. Seki, J. H. Oh, H. B. Akkerman, Z. Bao and Y. Matsuo, *Chemistry of Materials*, 2011, 23, 1646-1649.
269. Y. Wang and M. D. Watson, *Macromolecules*, 2008, 41, 8643-8647.
270. M. Mas-Torrent and C. Rovira, *Chemical Reviews*, 2011, 111, 4833-4856.
271. E. J. Wren, K. Mutkins, M. Aljada, P. L. Burn, P. Meredith and G. Vamvounis, *Polymer Chemistry*, 2010, 1, 1117-1126.
272. I. Horcas, R. Fernández, J. M. Gómez-Rodríguez, J. Colchero, J. Gómez-Herrero and A. M. Baro, *Review of Scientific Instruments*, 2007, 78, -.